Development of a Novel Parallel Synthesis by Injection Moulding and its Application to Study Dielectric Materials

Dissertation

zur Erlangung des Grades
des Doktors der Ingenieurwissenschaften
der Naturwissenschaftlich-Technischen Fakultät III
Chemie, Pharmazie, Bio- und Werkstoffwissenschaften
der Universität des Saarlandes

Vorgelegt von
Shuhua Ren

Saarbrücken
2009

Tag des Kolloquiums:	23.10.2009
Dekan:	Prof. Dr. Stefan Diebels
Vorsitzender:	Prof. Dr. Uli Kazmaier
Berichterstatter:	Prof. Dr. Dr. h.c. Michael Veith
	Prof. Dr. Wilhelm F. Maier
Akad. Mitarbeiter:	Dr. Holger Kohlmann

ACKNOWLEDGEMENTS

I would first like to express my special gratitude to Prof. Dr. Dr. h.c. Michael Veith for the opportunity and support to work under his supervision in a very active and open mind atmosphere at the Leibniz Institute for New Materials (INM). I am very thankful to his guidance and advices for the completion of this Ph.D. work, as well as the pleasant memories from the diverse together-activities of the mountain-biking and skiing.

I am grateful to Dr. Wolfgang Kochanek for his encouragements and contributions at the beginning of my work. I would like to thank Dr. Matthias Wittmar for his further encouragement and support during my dissertation work.

I would also like to thank Dr. Henning Bolz for a lot of discussions and help in operating injection moulding and translating the abstract into German. Special thanks also to Dr. Martin Heuberger and Mr. Robert Drumm concerning the operation and security of injection moulding machine. Thank Dr. Mesut Aslan for his selfless sharing of his knowledge about the ceramic processing. I wish to thank Dr. Ingrid Grobelsek, Dr. Mario Quilitz, Mr. Rudolf Karos, Dr. Claudia Fink-Straube for the kind characterizations in microstructure, dielectric properties, element analysis and the valuable comments. Thank Tobias Lehnert for his kind and friendly help for programming concerning the dielectric measurements. Also thanks to Sylvia de Graaf, our secretary for her kindness and help during this period. I am grateful to the members of mechanical workshop and electric workshop, especially to Mr. Dietmar Serwas, Mr. Herbert Beermann, Mr. Michael Schneider, Mr. Martin Britscher, Mr. Klaus Schmitt, for their contributions.

Last but by no means least, I like to thank my family. I am particularly indebted to my parents, Yingui and Linying, my brother Weihua, sister-in-law Jianrong and my cute nephew Haoxiang for their unconditional loving, never-ending encouragement and ongoing support. Very special thanks go to my dear husband, Ruiyong, for sticking by my side, both when I have the joy to achieve good results and when I am irritable and depressed by the frustrating results, being patient, supportive and helping. Great thanks also to his wonderful family who all have been supportive and caring.

ABSTRACT

A new parallel synthesis method by injection moulding technique has been developed for producing multi-component solid-state inorganic materials. The utility of the method has been illustrated by phase relationship investigation of the ternary system Fe_2O_3-TiO_2-Al_2O_3. The consistency of phase relationship to the previous investigations by conventional means proved the reliability of the new combinatorial strategy. A further application of this parallel synthesis strategy was performed on another ternary system CuO-TiO_2-CaO. The phase relations have been tentatively determined. From room-temperature dielectric property mapping at 10 kHz, giant dielectric constants ($\varepsilon_r > 10^4$) were observed for most of ceramic composites in the CuO-rich region and in the region along CuO-CaO binary line. The composites in the $CaCu_3Ti_4O_{12}$-rich region were found to give a comparable giant dielectric constant when sintered at 1050°C. Composites with high ε_r showed a particular microstructure of larger grains of a predominant phase surrounded by smaller grains of a secondary phase. In the representative composite with molar fraction of Cu/Ti/Ca of ~85/10/5, the frequency and temperature dependencies of permittivity and impedance were investigated. Strong hints suggested grain boundary effect as the most probable dielectric mechanism. Finally, the dielectric properties of the high-ε_r composites prepared by sol-gel process revealed the qualitative reproducibility of the high-ε_r composites.

ZUSAMMENFASSUNG

Ausgehend vom klassischen Spritzguss wurde eine neue Methode zur Parallelsynthese von anorganischen Multikomponentensystemen entwickelt. Die Leistungsfähigkeit der Methode wurde am Beispiel des ternären Systems Fe_2O_3-TiO_2-Al_2O_3 gezeigt. Die Phasenanalyse mit XRD entspricht der Literatur und zeigt die Zuverlässigkeit der neuen Methode. In einem weiteren Beispiel wurden die subsolidus-Phasenbeziehungen des ternären Systems CuO-TiO_2-CaO bei 950°C bestimmt. Bei 25°C und 10 kHz zeigen sich sehr große Dielektrizitätskonstanten $>10^4$ für die meisten Zusammensetzungen im CuO-reichen Bereich und entlang der binären CuO-CaO-Linie. Im Bereich von $CaCu_3Ti_4O_{12}$ findet man vergleichbar hohe dielektrische Konstanten nach Sinterung bei 1050°C. Proben mit derart hohen dielektrischen Konstanten zeigen eine typische Struktur mit großen Körnern aus einer vorherrschenden Phase und kleineren Körnern einer zweiten Phase. Für das Material Cu/Ti/Ca ~ 85/10/5 wurde die Impedanz temperatur- und frequenzabhängig bestimmt. Die Ergebnisse sprechen für einen internen Sperrschicht-Effekt im Bereich der Korngrenzen als den wahrscheinlichsten Mechanismus zur Erklärung des dielektrischen Verhaltens. Abschließend wurden durch Sol-Gel-Prozesse Materialien mit vergleichbar hohen dielektrischen Konstanten hergestellt. Dies belegt die Übertragbarkeit des neuen Syntheseverfahrens auf andere Methoden.

CONTENTS

ACKNOWLEDGEMENTS I
ABSTRACT III
ZUSAMMENFASSUNG V

1. Introduction and Objective 1

2. State of the Art 3

2.1. Parallel synthesis methods 3
2.1.1. Thin film deposition techniques 3
2.1.2. Diffusion multiple approach 4
2.1.3. Solution based methods 5
2.1.4. Other parallel synthesis methods 5
2.2. Injection moulding technique 6
2.3. Subsolidus phase relations in the ternary systems examined in this work 8
2.3.1. Fe_2O_3-TiO_2-Al_2O_3 8
2.3.2. CuO-TiO_2-CaO 9
2.4. Dielectric properties 9
2.4.1. Theoretical background 9
2.4.2. high-ε_r materials 13
2.4.2.1. $CaCu_3Ti_4O_{12}$ 13
2.4.2.2. Other materials 15
2.4.3. Possible mechanism for the giant dielectric response 15
2.4.3.1. Intrinsic mechanism 16
2.4.3.2. Extrinsic mechanism 17
2.4.3.3. Other mechanisms 22

3. Experimental 23

3.1. Parallel synthesis of the ternary systems 23
3.1.1. Synthesis and combination of three layers 24

3.1.2. Separation of library cells by honeycomb cutting 27
3.1.3. Mixing and post treatment 29
3.2. Sol-gel process for representative candidates in CuO-TiO_2-CaO ternary system .. 30
3.3. Physical Characterizations 31
3.3.1. Phase relations determination 31
3.3.2. Microstructure and composition analysis 32
3.3.3. Electric property testing 32
3.3.4. Other properties 33

4. Results and Discussion 35

4.1. Parallel synthesis for the Fe_2O_3-TiO_2-Al_2O_3 ternary system 35
4.1.1. Microstructure difference 35
4.1.2. Mixing of three components 41
4.1.3. Composition analysis 44
4.1.4. Phase relations in the Fe_2O_3-TiO_2-Al_2O_3 system 45
4.2. Phase relationship in CuO-TiO_2-CaO system 54
4.3. Dielectric property in ternary system CuO-TiO_2-CaO 57
4.3.1. Dielectric property mapping 57
4.3.2. Dielectric property in CuO-rich region 59
4.3.3. Dielectric property in $CaCu_3Ti_4O_{12}$-rich region 65
4.4. Possible mechanism for the giant dielectric constant 77
4.4.1. Internal barrier layer capacitance (IBLC) mechanism 77
4.4.2. Temperature dependence of dielectric response 79
4.4.3. Temperature dependence of impedance spectra 82
4.5. Dielectric properties of representative composites synthesized by sol-gel method 87
4.5.1. $CaCu_3Ti_4O_{12}$ 87
4.5.2. CuO-rich composite 90

5. Summary and Conclusions 91

6. Outlook 95

7. Appendix 99

7.1. List of abbreviations 99

7.2. List of used chemicals 100
7.3. List of instruments and equipments 101
7.4. Composition calculation 102
7.5. Parallel synthesis for ternary system CuO-TiO_2-CaO 105
7.5.1. Photographs of injected and cutted three layers 105
7.5.2. Mixing of three components in ternary system CuO-TiO_2-CaO 106

References 107
List of publications 121

LIST OF FIGURES

Fig. 2.1 The basic sequence of the powder injection moulding process. 7

Fig. 2.2 Schematic curves of the real and imaginary parts of the permittivity of a fictive material. 12

Fig. 2.3 The molecular model of $CaCu_3Ti_4O_{12}$. 14

Fig. 2.4 (a) Equivalent circuit used to represent the electrical properties of grain and grain-boundary effects and (b) The corresponding schematic impedance spectra according to equivalent circuit (a). 18

Fig. 2.5 (a) Microstructure model of polycrystaline $CaCu_3Ti_4O_{12}$ showing the internal domains inside the grains. (b) Equivalent circuit of (a) 21

Fig. 3.1 Schematic arrangement of three component systems. (a) Fe_2O_3, TiO_2 and Al_2O_3 layers, in which each layer was individually produced by injection moulding from the mixtures of the corresponding solid powders, paraffin wax, surfactants; (b) the combination of three layers on aluminium honeycomb; (c) the combinatorial library made by honeycomb cutting. 23

Fig. 3.2 The images of the moulds used to produce three layers in injection moulding. (a) the right half mould and (b) the pair of moulds for producing up/down layers; (c) the pair moulds with TiO_2 middle layer on one mould for producing middle layers. 26

Fig. 3.3 Schematic experimental set-up used to separate library cells. (a) injected three layers; (b) silicone rubber layer sputtered by graphite; (c) stainless-steel cover; (d) Frame made of aluminium alloy; (e) honeycomb. 27

Fig. 3.4 Photographs of the failed honeycomb cutting. 28

Fig. 3.5 Photographs of the set-up used to separate library cells in ternary system Fe_2O_3-TiO_2-Al_2O_3. (a) frame without cover, (b) full set-up with three layers inside the frame, (c) the product after honeycomb cutting with sputtered graphite paper on top, (d) the product after honeycomb cutting. Note that in (d), the black color on top of three layers is carbon graphite from (c). 28

Fig. 3.6 Flowing chart for the synthesis of representative candidates in the CuO-TiO_2-CaO system by soft chemistry method. 31

Fig. 4.1 SEM images of original powder (left) and the corresponding feedstock (right) of Fe_2O_3 with magnification of (a) ×5000, (b) ×50000, respectively, and (c) TiO_2, (d) Al_2O_3. 37

Fig. 4.2 The operation curves during injection moulding for Fe_2O_3 feedstock 38

Fig. 4.3 Principle structure for polyvinylether (left image). The polyvinylether Luwax V has C18-side chains (right image). 39

Fig. 4.4 Photographs of the injected three layers (a) Fe_2O_3 layer, (b) two layers of Fe_2O_3 (bottom layer) and TiO_2 (top layer), (c) three layers of Fe_2O_3 (bottom layer), TiO_2 (middle layer), and Al_2O_3 (top layer). 40

Fig. 4.5 Ex-situ mixed products of the layered pieces in self-made aluminium rack 42

Fig. 4.6 EDX analysis of different positions in magnifications of ×5000, ×50000, ×400000 for the mixture with composition of Fe : Ti : Al = 30.1: 33.8 : 36.1 43

Fig. 4.7 Compositions (mol %) and phase relationship for combinatorial library prepared by injection moulding technique in the system Fe_2O_3-TiO_2-Al_2O_3 in air at 1300°C. The dashed lines are phase boundaries reported by Pownceby et al. 46

Fig. 4.8 XRD patterns of samples in Region 1 of Fig. 4.7 with composition (molar fraction) of Fe_2O_3 : TiO_2 : Al_2O_3 in starting mixtures of (a) 97.0 : 2.0 : 1.0, (b) 94.0 : 2.0 : 4.1, (c) 90.7 : 2.0 : 7.3, (d) 87.2 : 2.1 : 10.7, (e) 83.5 : 2.1 : 14.3, (f) 79.6 : 2.2 : 18.2 47

Fig. 4.9 The lattice constants *a* (top), *c* (bottom) as a function of Al atomic content in hematite in the samples in Fig. 4.8. 48

Fig. 4.10 XRD patterns of samples along the Fe_2O_3-TiO_2 edge from hematite solid solution to the bi-phasic region of (hematite + pseudobrookite), which are marked in Region 2 of Fig. 4.7 49

Fig. 4.11 SEM micrographs for sintered samples in air at 1300°C. The composition (molar fraction) of Fe_2O_3 : TiO_2 : Al_2O_3 in starting mixtures is (a) 88.0 : 4.6 : 7.4, (b) 3.5 : 95.3 : 1.2, (c) 5.3 : 2.7 : 92.0. 51

Fig. 4.12 Phase relationship in ternary system CuO-TiO_2-CaO at 950°C in air. The phase relationship analysis is based on compositions shown in Fig. 4.14. 55

Fig. 4.13 The XRD patterns for the representative samples (A) to (D) in phase region V, which are marked in Fig. 4.12, with starting compositions of CuO : TiO_2 : CaO = 44.5 : 2.0 : 53.5, 62.0 : 1.8 : 36.2, 67.1 : 1.7 : 31.2, 84.3 : 1.5 : 14.2. 56

Fig. 4.14 Room-temperature of (a) ε_r and (b) tan δ of the samples sintered at 950°C in ternary system CuO-TiO_2-CaO at 10 kHz. Colored dots represent the

investigated compositions (molar fraction) used to determine dielectric properties and the phase relations in Fig. 4.12. Dashed lines show the phase boundaries. 58

Fig. 4.15 The frequency dependence of ε_r (up) and tan δ (down) of (a): samples (1-a) to (1-d) (down to up) of Region 1 and (b): samples (2-a) to (2-g) (down to up) of Region 2 in Fig. 4.14 (a). Sample (1-b*) has the same starting composition as sample (1-b), but sintered at 1000°C, whereas others were sintered at 950°C. 60

Fig. 4.16 SEM images of (a): sample (1-b) and (b): sample (1-b*) in Fig. 4.15 with sintering temperature of 950°C and 1000°C, respectively. 62

Fig. 4.17 SEM images of samples (1-a), (1-c), (1-d) (left-side images) and samples (2-a), (2-c), (2-f) (right-side images) in region 1 and region 2 of Fig. 4.14, respectively. 64

Fig. 4.18 The frequency dependence of ε_r (up) and tan δ (down) of samples (3-a) and (3-a*) in Region 3 of Fig. 4.14 (a) with the same starting composition but sintered at 1050°C, 950°C, respectively. 66

Fig. 4.19 SEM micrographs of (a): sample (3-a*) and (b): sample (3-a) in Fig. 4.18 sintered at 950°C and 1050°C, respectively. 67

Fig. 4.20 The EDX composition analysis for sample (3-a) in Fig. 4.19. (a) big grain, (b) small grains, and (c) liquid phase, respectively. 68

Fig. 4.21 The frequency dependence of ε_r (up) and tan δ (down) of samples (3-a) and (3-b) in Region 3 of Fig. 4.14 (a) sintered at 1050°C. 69

Fig. 4.22 XRD patterns of sample (3-a) and (3-b) in Region 3 of Fig. 4.14 (a) sintered at 1050°C. 70

Fig. 4.23 SEM micrographs of (a): sample (3-b*) and (b): sample (3-b) sintered at 950 °C and 1050°C, respectively. 71

Fig. 4.24 The frequency dependence of ε_r (up) and tan δ (down) of samples (3-c), (3-d) and (3-e) in Region 3 of Fig. 4.14 (a) sintered at 1050°C. 72

Fig. 4.25 X-ray diffraction patterns of sample (3-c), (3-d) and (3-e) in Fig. 4.24. 72

Fig. 4.26 SEM micrographs of (a): (3-c), (b): (3-d) and (c): (3-e) in Fig. 4.24. 73

Fig. 4.27 The frequency dependence of ε_r (up) and tan δ (down) of samples (3-c) and (3-f) sintered at 1050°C, which are marked in Fig. 4.14 (a). 74

Fig. 4.28 SEM micrographs of sample (3-f) sintered at 1050°C 74

Fig. 4.29 The frequency dependence of ε_r (top) and tan δ (bottom) of composites (3-e), (3-g), sintered at 1050°C 75

Fig. 4.30 SEM image of sample (3-g) sintered at 1050°C. 76
Fig. 4.31 Microstructure models of multiphased composites showing the grain boundary effect..... 78
Fig. 4.32 XRD pattern of the sample (1-c) sintered at 950°C in air. 79
Fig. 4.33 The frequency dependence of the (a) ε_r and (b) $\varepsilon''/\varepsilon_0$ at temperatures between 25 and 130°C for sample (1-c) sinted at 950°C in air. 80
Fig. 4.34 Arrhenius plot of dielectric relaxation time τ for the sintered sample (1-c). 81
Fig. 4.35 Impedance complex plane plot, Z^* at different temperatures for the sintered sample (1-c). The fitting results were obtained and consist of segments of three (*RC*) elements connected in series.. 83
Fig. 4.36 Equivalent circuit used to represent the electrical properties in sample (1-c). 84
Fig. 4.37 Arrhenius plot of resistance R_1, R_2, R_3 obtained from impedance spectra in sample (1-c). 85
Fig. 4.38 The TG-DSC curves of the thermal decomposition of $CaCu_3Ti_4O_{12}$ precursor at a heating rate of 10°Cmin^{-1} in syn. air. 87
Fig. 4.39 XRD patterns of sample $CaCu_3Ti_4O_{12}$ with thermal treatments of (a) 500°C for 0.5h, (b) 750°C for 2h, (c) 1050°C for 70h and (d) 1090°C for 70h. 88
Fig. 4.40 SEM images of sample $CaCu_3Ti_4O_{12}$ sintered at (a) 1050°C and (b) 1090°C. 89
Fig. 4.41 The frequency dependence of ε_r and tan δ of $CaCu_3Ti_4O_{12}$ sintered at 1050°C and 1090°C, respectively. 89
Fig. 4.42 The frequency dependence of ε_r and tan δ of CuO-a sintered at 1050°C and 1090°C, respectively. 90
Fig. 6.1 Schematic set-up for parallel synthesis of quaternary system. 95
Fig. 7.1 (a) Vertical view of combinatorial three layers in x-y coordinate; (b) A vertical plane cutting parallel to BC is designated as "MN"; (c) the cross section of the vertical plane cutting of (b). The individual thickness of a random point "P" inside the triangular prism ABC from layer A, layer B and layer C are h_A, h_B, h_C, respectively..... 103
Fig. 7.2 Photographs of (a) injected three layers, left: $CaCO_3$ layer; middel: TiO_2 layer; right: CuO layer, (b) the product after honeycomb cutting..... 105
Fig. 7.3 Ex-situ mixed products of the layered pieces in self-made aluminium rack. 106
Fig. 7.4 EDX analysis of different positions in magnifications of × 5000, × 50000, × 40000 for the mixture with composition of Cu : Ti : Ca = 10.4: 80.2 : 9.4. Dashed colored lines indicate the calculated composition..... 106

LIST OF TABLES

Table 2.1 Electrical microstructure of electroceramics. 19

Table 3.1 The blends compositions successfully used as feedstock in injection moulding..... 25

Table 3.2 Moulding variables to produce metal oxide layers used in this study. 25

Table 4.1 ICP-AES composition analysis of some samples in the library compared to the calculated values..... 44

Table 4.2 Specific resistivity, capacitance and permittivity values for (R_1C_1), (R_2C_2) and (R_3C_3) at various temperatures determined by impedance spectrscopy in sample (1-c). 84

Table 7.1 List of abbreviations 99

Table 7.2 Chemicals used in the preparation of combinatorial libraries in injection moulding and sol-gel process. 100

1. Introduction and Objective

Functional materials are an essential part of our daily life. The development and application of new functional materials has therefore a significant effect on our living [1-2]. Due to the unlimited worldwide demand for new or improved materials, the materials development has always been a demanding, time-consuming, and costly process [3]. Combinatorial methods allow parallel synthesis and screening of large arrays of different materials. The improved efficiency of a combinatorial approach makes it possible to treat complex systems and interactions in a "faster, cheaper, and more convenient" way and has stimulated much progress in the past few years in studies of phase diagrams and composition-structure-property relationships [4-5].

Various parallel synthesis strategies have been developed for accelerated materials research and discovery [1, 4, 6]. For instance, the combinatorial thin film deposition technique [7, 8], diffusion-multiple approach [9], ink-jet printing technique [10] and automatic microdispenser systems [11-12] have been successfully developed and applied in materials research. The systematic nature of the combinatorial approaches can reveal complex phenomena and interactions that otherwise would be difficult to be aware of or find using conventional one-composition-at-a-time practice [4]. This is particularly convenient for the studies of phase diagrams considering the conventional methods by mechanical mixing of coarse starting materials and grinding operations at each discrete composition point are time-consuming, energy intensive, and discouraging because of the difficult technique of homogeneous milling and product contamination [13-14].

Powder injection moulding technique is a method of shaping engineering artifacts from ceramics powders and it offers near net shape production by automated processes [15]. Taking advantage of injection moulding fabrication route, a new parallel synthesis method has been developed for the synthesis of material libraries in this work. Comparing to the existing parallel synthesis technologies, this new parallel synthesis method could provide a number of potential advantages. Powders with a particle size range from nano- to submicrometer can be applied in this approach. The settling which is probably happening in nanoparticle suspension

can be avoided. The amount of materials which is obtained for each composition is sufficient to test the bulk properties [16].

Combinatorial method provided us an efficient and systematic way to discover possible new functional solid-state materials and to study composition-structure-property relationships. Therefore, the objective of this work includes two parts: (1) to develop this new parallel synthesis method based on injection moulding technique and to verify the reliability of this technology by investigation of the phase relationships in the ternary system Fe_2O_3-TiO_2-Al_2O_3; (2) the application of the new parallel synthesis method on the development of new dielectric material in order to discover the possible new promising dielectric candidates and investigate the phase relationship in the ternary system CuO-TiO_2-CaO and accordingly, to study the possible composition-structure-property relationship, and finally, to reveal the possible mechanism for the observed promising dielectric behaviour.

In this thesis, the development of this new parallel synthesis method is introduced in Section 3.1 and discussed in Section 4.1. The phase diagram investigation in the ternary system Fe_2O_3-TiO_2-Al_2O_3 is used to determine the applicability and reliability of the new technique in comparison to the previous work by conventional methods (Section 4.1). In this part of work, the consistence of the phase relations with the previous report, especially the linear lattice parameter variation in solid solution region confirms the reliability of the method.

The new parallel synthesis technique is further applied to produce the variation of the compositions in the CuO-TiO_2-CaO ternary system. The subsolidus phase relationship (Section 4.2) and dielectric properties (Section 4.3) in the ternary system have been investigated. The possible composition-structure-dielectric property relations are discussed in Section 4.3. The probable mechanism for the observed giant dielectric response has been revealed in Section 4.4. Guided by the dielectric responses results from parallel synthesis, some representative high dielectric constant candidates are also synthesized by sol-gel process and their dielectric properties are accordingly investigated in Section 4.5.

Finally, the results of this thesis are summarized in Chapter 5. Outlook of the present work is introduced in Chapter 6. The thesis contains also an Appendix (Chapter 7), where extra information including mathematic calculations of the compositions and some other technical information are provided.

2. State of the Art

Four sections are included in this chapter: (1) the existing parallel synthesis strategies for the preparation of solid state materials (Section 2.1); (2) the basic background concerning the injection moulding technique (Section 2.2); (3) the subsolidus phase relationships in the ternary systems Fe_2O_3-TiO_2-Al_2O_3 and CuO-TiO_2-CaO (Section 2.3); (4) the dielectric properties investigations in the materials located in the ternary system CuO-TiO_2-CaO (Section 2.4). In the last section (Section 2.4), some necessary basic background and the possible mechanism to understand the giant dielectric response have been also included.

2.1 Parallel synthesis methods

2.1.1 Thin film deposition techniques

The idea of a combinatorial approach was first introduced to accelerate phase diagram studies, and it can be traced back to at least half a century ago. Boettcher et al. [17] tested the methodology by depositing thin films with composition gradients and mapped the phase diagram of the Ag-Pb-Sn ternary system. Similarly, Kennedy et al. [18] created a thin film with varying ternary compositions of the Cr-Fe-Ni system on a substrate using electron beam physical vapor deposition of pure Cr, Fe and Ni in elemental form. In 1970, Hanak [19] created the “Multiple-Sample Concept” and successfully prepared composition spread or gradient libraries. In this method, they were able to obtain, in one experiment, almost the entire composition continuum of a given binary or ternary system deposited on one substrate. Xiang et al. [20-21] combined thin film deposition and physical masking techniques for parallel synthesis of spatially addressable libraries of solid-state materials. This combinatorial thin film deposition technique by physical deposition processes, which utilizes natural gradient profiles followed by interdiffusion, has been successfully applied and developed for phase diagrams of alloys [22-24].

In such a parallel synthesis technique, thin films, however, might interact with the substrate and complicate the study of equilibrium phases by formation of metastable structures [25-26]. On the other hand, when bulk properties of the materials are required, the existing approaches for solid-state functional materials using thin film deposition are difficult to apply to bulk structural property screening. The structural properties of bulk materials are microstructure dependent, and the desired microstructures can be difficult to achieve in thin films, especially when the scale of the microstructure is larger than the film thickness [27]. Moreover, phase precipitation kinetics and diffusivities are usually very different in bulk samples from in thin films due to surface effects, thus data evaluated from thin films cannot be directly used to design bulk structural materials [4, 28].

2.1.2 Diffusion multiple approach

A different methodology called “diffusion multiple approach” was developed by Zhao et al. [9, 29] Large, multi-component array (libraries) was assembled from three or more different metal (or ceramic) blocks, which were arranged as a triple, quadruple, etc. and placed in intimate interfacial contact. The composition variations were thus generated through thermal interdiffusion at high temperature. This method has long been used to determine phase diagrams and evaluate diffusion coefficients [30]. By varying the cooling rate and/or subsequent heat treatment of the diffusion couples, valuable information on precipitation kinetics can be obtained simultaneously for a library of compositions. This new combinatorial way of evaluating precipitation kinetics is significant since such information would be very time-consuming and expensive to obtain when handling one sample at a time using the conventional approach [31].

However, this method was not widely adopted, partly due to the difficulty in making good contacts at the tri-junctions and quadri-junctions [32]. Local equilibrium at the phase interfaces is the basis for applying diffusion couples and also diffusion multiples to phase diagram determination. The local equilibrium is only reached at the phase interface, not in the entire diffusion zone, which serves as the base of applying diffusion couple/multiple techniques for determining equilibrium phase diagrams. Furthermore, the unevenly distributed phase points in the cross-section of the interface region need to be determined accurately with high spatial resolution [4]. To avoid melting, the highest temperature for

diffusion heat treatment is limited by the lowest liquidus temperature of the multicomponent system. To determine phase diagrams at relatively low temperatures, the thin film deposition techniques are advantageous since much less time is required to form a homogeneous composition across the thin film thickness [1].

2.1.3 Solution based methods

In solution-based parallel synthesis, the precursor solutions are dispensed automatically by microdispenser or inkjet delivery apparatus, followed by mixing and post treatments [33-34]. In this method, complex parameters and sensitive handling procedures have to be considered, such as pH values, high temperatures or pressures, nature of solvents, and so on [1].

In addition to soluble compounds in the liquid starting state, stable suspensions composed of high reactive nanoparticle powders have also been proven to be applicable in automatic microdispenser or ink-jet delivery systems to produce combinatorial libraries [35-40]. Due to the nanometric particle size of the suspension, the mixing of different precursors and the interdiffusion between the particles can be more effective than that in homogeneous solutions, in which one precursor could be precipitated prior to other [35]. However, this method is limited to the treatment of nanoparticles and stability of the nanoparticle suspensions has to be well-controlled to avoid sedimentation or agglomeration during operation [41]. In ink-jet printing techniques [37-39], the suspension of different ceramic powders has been successfully delivered to create combinatorial libraries of ceramic compositions. Interestingly, continuous gradients can be generated in this technique; the particle size determines the minimum gradient step size [42]. However, demixing might occur during the drying stage of the droplets of multiple powders [43].

2.1.4 Other parallel synthesis methods

Some other parallel synthesis methods have also been developed. So-called split and pool methods [44-45] have been developed to achieve highly diverse materials libraries in the range of 10^3-10^8 samples by combinatorial permutation of element combinations or synthesis parameters. In the area of glass systems, an automated batch melting apparatus has been

developed for high-throughput synthesis, and new multicoloured glasses with a low transition temperature have been found in the P_2O_5-TeO_2-ZnO ternary system [46].

The application of combinatorial chemistry in materials research provides acceleration of basic research, fast discovery of knowledge, reduced development times, reduced time for products to the market, etc.[1] However, diverse parallel synthesis strategies can not solve all the problems. For example, although it is convenient to use thin-film techniques to lay out large compositional gradients, the deposition techniques do not necessarily produce equilibrium phases, and mechanical constraints imposed by the substrate could greatly alter the physical properties of interest. When properties of interest are directly associated with microstructural properties such as grain boundary effects, optimizing the properties by thin-film deposition becomes increasingly challenging [6]. To this point, a novel parallel synthesis method for solid-state materials has been developed in this work by using injection moulding technique. Comparing to the other existing parallel synthesis technologies, the new method provides a wide choice of the ceramic materials, a sufficient amount of each composition to test the bulk properties, etc. [16]

2.2 Injection moulding technique

Powder injection moulding is used in industrial production of small ceramic or metal components of complex shape and provides high dimensional precision [47]. The capacity for complex geometries to be realized in one production step in an automated process is an important advantage of injection moulding. This makes injection moulding suitable for mass producing articles [48]. The basic sequence of the powder injection moulding process is presented in Fig. 2.1 [49]. Fabrication starts by mixing a thermoplastic binder, additives and a powder mixture, referred as feedstock. The feedstock is then injected into a mould cavity to form the required shape. Parts injected at this stage are known as “green parts”. The green parts undergo debinding process where binders are removed by using either thermal evaporation or solvent washing. Finally the as-obtained parts are then consolidated in a sintering process through high temperature furnaces to close the voids created during debinding. Mixing of powder and binder is an important phase in this process, as the uniformity of the mixture influences the flow behaviour of the feedstock and the sintered process [50-51]. The hard particles of ceramics or metals are mixed with a binder system that

covers the particles. This binder system is made usually of thermoplastic, wax and additives that allow the mixture to be molten and injected inside a mould in a way similar to that performed for thermoplastics alone [52].

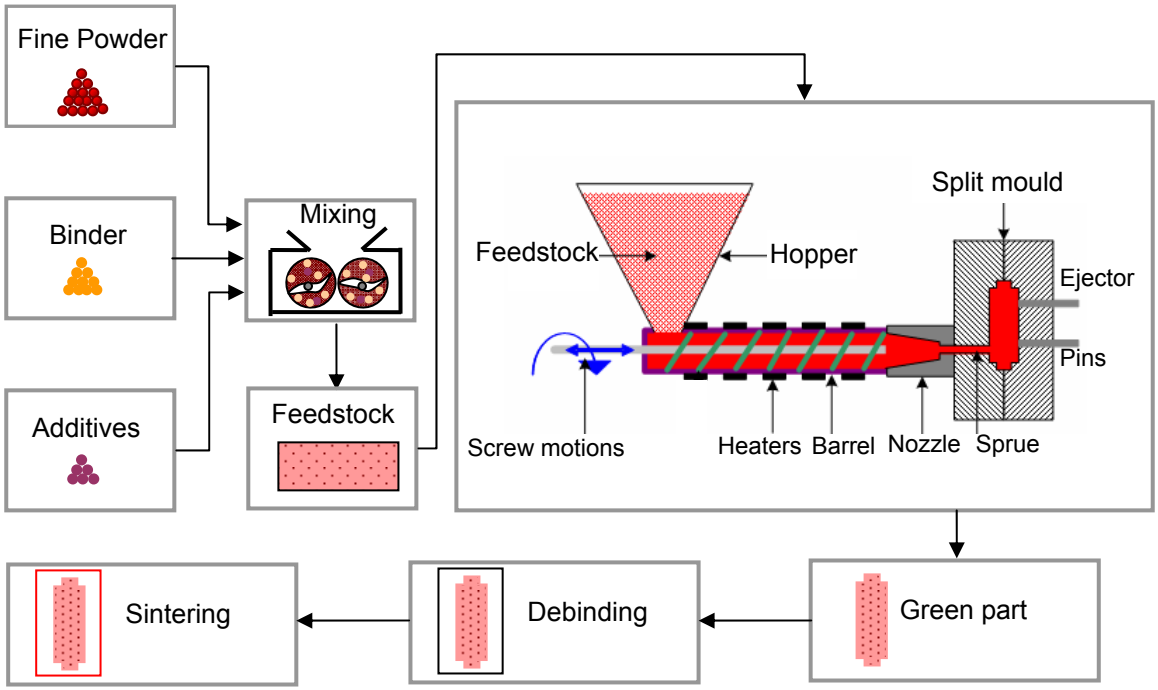

Fig. 2.1 The basic sequence of the powder injection moulding process. The process involves the mixing of selected ceramic powder with binders to form the feedstock, which is then moulded in a mould cavity to form the required component shape. This shape undergoes a debinding process and is then consolidated by sintering.

Typical particle sizes encountered in powder injection moulding are in the range of 0.1-15 µm [50]. Nanoscaled powder ceramics exhibited significant advantages over coarser-grained ceramics since lower sintering temperatures may be possible when using nanosize rather than microsize particles [53-55]. Injection moulding of nanoscaled ceramic powders offers the possibility of near net shape forming thin and complex structures. However, little information concerning the processing of powders with particle sizes <100 nm has been reported due to their big specific surface area and the tendency to form agglomerates, which alter the flow

behaviour of the feedstock, especially when high solid loading contents are required [56]. Nano powders of Al_2O_3 and TiO_2 were proven to be successfully applied in injection moulding technique, respectively [56]. Referred to this research [56], the first ternary system, which was applied to test the novel parallel synthesis strategy based on injection moulding technique, was accordingly chosen in this dissertation work to be the ternary Fe_2O_3-TiO_2-Al_2O_3 system. Nano- or submicron scaled powders are used in this method. The phase relationship analysis in this ternary system in comparison to the state of the art report by conventional means was performed in the first part of this thesis to testify the reliability of this new parallel synthesis technique by injection moulding. The methodology of the novel parallel synthesis by injection moulding technique is introduced in detail in experimental part (Chapter 3).

2.3 Subsolidus phase relations in the ternary systems examined in this work

2.3.1 Fe_2O_3-TiO_2-Al_2O_3

The first study of the system Fe_2O_3-TiO_2-Al_2O_3 was by Fotiev et al. [57], who used a quenching technique followed by XRD analysis to determine the phase relations at temperatures below 1000°C. The phase relations in subregion Fe_2TiO_5-Al_2TiO_5-Al_2O_3-Fe_2O_3 inside the ternary system Fe_2O_3-TiO_2-Al_2O_3 remains uncertain in this tentative study.

A further study by Pownceby et al. established the detailed phase relations within the ternary Fe_2O_3-TiO_2-Al_2O_3 system between 1000° and 1300°C [58]. Some of the important binary and ternary subsystems within this ternary system have been well described at temperatures below 1300°C. The main features of the phase relations are (a) the presence of an $Fe_{2-2x}Al_{2x}TiO_5$ (M_3O_5) solid-solution series between the end members Fe_2TiO_5 and Al_2TiO_5, (b) a miscibility gap along the Fe_2O_3-Al_2O_3 binary, (c) an M_2O_3 (ss) ternary solid solution in Fe_2O_3-rich region, and (d) an extensive three-phase region characterized by the assemblage M_3O_5 + M_2O_3 (ss) + corundum (ss). The M_3O_5 solid solution is continuous across the entire compositional range at 1300°C; however, as the temperature is lowered, the solid solution becomes unstable relative to the assemblage (M_3O_5 + Al_2O_3 + TiO_2). This shows considerable discrepancy compared to the first tentative phase relations study in this system at T≤1000°C by Fotiev et al. [57], who reported the formation between Fe_2TiO_5 and Al_2TiO_5 of a continuous series of substituational

solid solutions $Fe_{2-2x}Al_{2x}TiO_5$. Herein, 1300°C was chosen to be the sintering temperature for the phase relationship analysis in the ternary system Fe_2O_3-TiO_2-Al_2O_3 in the present work. The results will be compared to those by Pownceby et al. [58]

2.3.2 CuO-TiO_2-CaO

The phase diagrams of the binary systems of CaO-CuO [59-61], CaO-TiO_2 [62-63], CuO-TiO_2 [64] have been extensively studied. Very recently, Jacob et al. [65] computed the phase diagram for the system CaO-TiO_2-CuO/Cu_2O at 1000°C as a function of oxygen partial pressure (P_{O2}/P^0) using the Gibbs energy minimization technique. P^0 represents the standard atmospheric pressure. At (P_{O2}/P^0)=1, three ternary oxides, $CaTiO_3$, $Ca_4Ti_3O_{10}$, $Ca_3Ti_2O_7$ are evaluated to be present along the CaO-TiO_2 binary, and Ca_2CuO_3 is present along the CaO-CuO binary. With the reduction in oxygen partial pressure a new phase Cu_3TiO_4, containing both Cu^+ and Cu^{2+} ions, appears along the CuO-TiO_2 binary at (P_{O2}/P^0) $\leq$ 0.165. It was concluded that the ternary phase relations are very sensitive to the oxygen partial pressure [65]. Up to now, no experimental phase relationship investigation in the ternary system CuO-TiO_2-CaO has been done.

2.4 Dielectric properties

2.4.1 Theoretical background

The dielectric properties of the various materials used in microelectronic components fabrication play an important role in achieving the desired performance of integrated circuits. A basic understanding of dielectric properties is therefore necessary.

One important property of a dielectric material is its permittivity. Permittivity (ε) is a physical quantity that describes how an electric field affects, and is affected by, a dielectric medium, and is determined by the ability of a material to polarize in response to the field, and thereby reduce the total electric field inside the material [66-67].

Different from the response of a vacuum, the response of dielectric materials to external fields generally depends on the frequency of the field. This frequency dependence reflects the fact that a material's polarization does not respond instantaneously to an applied field. The response must always be causal (arising after the applied field) which can be represented by a phase difference. For this reason permittivity is often treated as a complex function (since complex numbers allow specification of magnitude and phase) of the frequency of the applied field [68-69].

Since the response of materials to alternating fields is characterized by a complex permittivity, it is natural to separate its real and imaginary parts, which is done by convention in the following way [69]:

$$\varepsilon^* = \varepsilon' + i\varepsilon'' = \frac{D_0}{E_0}(\cos\delta + i\sin\delta) \qquad \textbf{(2.1)}$$

where ε' is the real part of the permittivity, which is related to the stored energy within the medium; ε'' is the imaginary part of the permittivity, which is related to the dissipation (or loss) of energy within the medium; δ is the phase difference between electric displacement field (D) and electric field (E); D_0 and E_0 are the amplitudes of the displacement and electrical fields, respectively; i is the imaginary unit, $i^2 = -1$.

The advantage of high ε' substances is the fact that they enable a reduction in physical volume of capacitors and therefore a decrease in the size of device products. The dispersion of the dielectric response leads to dielectric losses of the matter which can be mathematically expressed by the imaginary part (ε'') of the complex dielectric permittivity. The lower the dielectric loss, the more effective is a dielectric material.

Dielectric losses are usually described by the loss tangent:

$$\tan\delta = \frac{\varepsilon'}{\varepsilon''} \qquad \textbf{(2.2)}$$

This definition of the dissipation factor (loss tangent) is the ratio of the energy dissipated to the energy stored in the dielectric material. The dissipated energy typically turns into heat or is radiated as radio frequencies into the air. All dielectrics (except vacuum) have two types of losses. One is a conduction loss, representing the flow of actual charge through the dielectric. The other is a dielectric loss due to movement or rotation of the atoms or molecules in an alternating electric field.

The dielectric constant (ε_r) of a material is the ratio of its real part of permittivity (ε') to the permittivity of vacuum ε_0 ($\varepsilon_0 = 8.854 \times 10^{-12}$ Fm^{-1}). Therefore,

$$\varepsilon_r = \frac{\varepsilon'}{\varepsilon_0} \tag{2.3}$$

The dielectric constant is also known as the relative permittivity of the material. Since the dielectric constant is just a ratio of two similar quantities, it is dimensionless. The dielectric constant of vacuum is 1 by definition.

The dielectric constant is directly related to the dielectric material capacitance (C), which is used for the calculation of the dielectric constant of the material.

$$C = \varepsilon' \frac{A}{d} = \varepsilon_r \varepsilon_0 \frac{A}{d} \tag{2.4}$$

where ε_0 is the permittivity in vacuum, A is the sample area and d is the sample thickness.

A dielectric material may have several dielectric mechanisms or polarization effects that contribute to its overall permittivity. Fig. 2.2 illustrates the frequency dependence of the real and imaginary parts of the dielectric permittivity [68]. Various processes are labeled on the image: boundary planes, orientation, distortion and electronic polarizations. Electronic polarization exists in all dielectrics and follows the electric field almost instantaneously as it is based on the displacement of the negatively charged electron shell against the positively charged core. The distortion polarization cannot respond as rapidly as fast changing fields since it involves the displacement of entire ions. Orientation polarization describes the alignment of permanent dipoles. At ambient temperatures, usually all dipole moments show a statistical distribution of their directions. An electric field generates a preferred direction for the dipoles, while the thermal movement of the atoms perturbs the alignment.

Space charge polarization could exist in dielectric materials which show spatial inhomogenieties of charge carrier densities. Space charge polarization effects can occur in ceramics with electrically conducting grains and insulating grain boundaries (so-called Maxwell-Wagner polarization). Domain wall polarization plays a decisive role in ferroelectric materials and contributes to the overall dielectric response. The motion of a domain wall that separates regions of different oriented polarization takes place by the fact that favored oriented domains tends to grow with respect to the applied field.

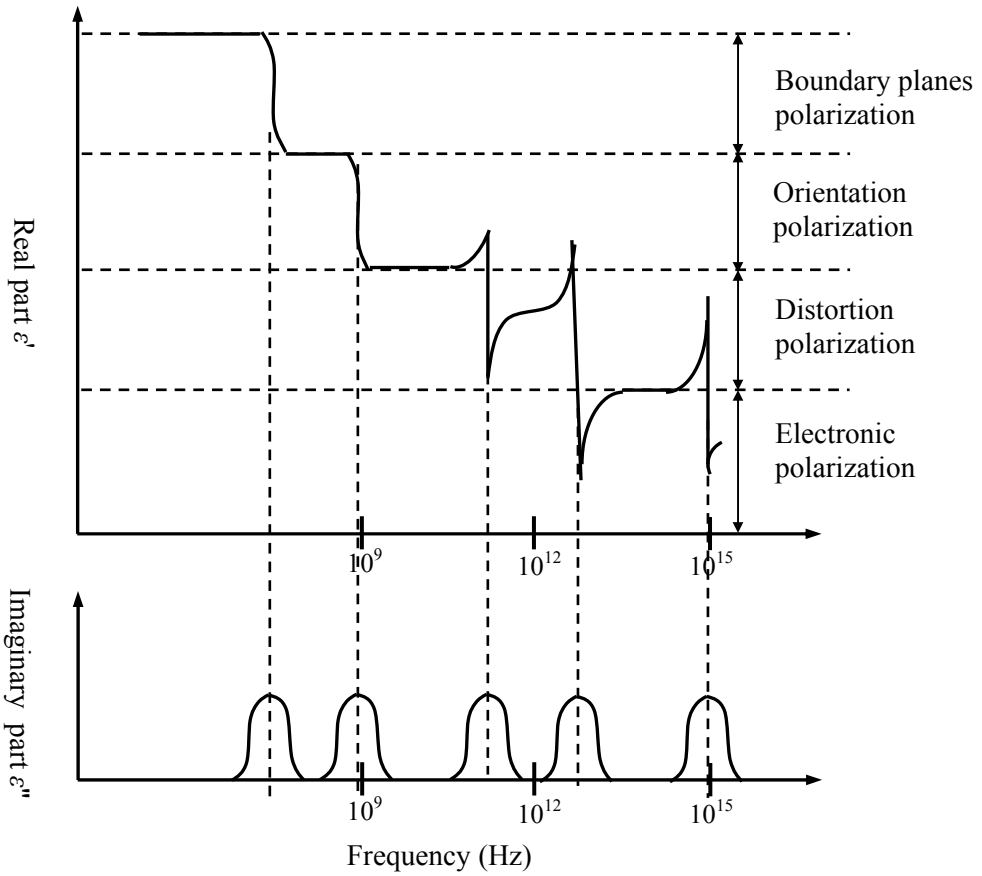

Fig. 2.2 Schematic curves of the real and imaginary parts of the permittivity of a fictive material. The polarization modes exhibited in the material includes electronic, distortion, orientation and boundary planes polarizations [68-69].

The total polarization of dielectric material results from all the contributions discussed above. Each contribution stems from a short-range movement of charges that responds to an electric field on different time scales and, hence, through a Fourier transform, in different frequency regimes. If the oscillating mass experiences a restoring force, relaxation behaviour is found (for orientation, domain walls, and space charge polarization). Resonance effects are observed for the ionic and electronic polarization. The dispersion of the dielectric function is also shown in Fig. 2.2, and holds the potential to separate the different dielectric contributions. This frequency dependence reflects the fact that a material's polarization does not respond instantaneously to an applied field. As frequency increases, the slow mechanisms drop out in

turn, leaving the faster ones to contribute to ε'. The loss factor (ε'') will correspondingly peak at each critical frequency.

A perfect dielectric is a material that has no conductivity, thus exhibiting only a displacement current. Therefore it stores and returns electrical energy like an ideal capacitor [70]. Due to the requirements of the miniaturization in microelectronic devices [71], the higher the dielectric constant, the more charge can be stored, and the smaller the electronic circuits can be made [72-73].

2.4.2 High-ε_r materials

High-dielectric constant materials have been playing a significant role in microelectronics, since they have been used as important devices such as capacitors and memory devices [74]. Ferroelectric oxides like $Pb(Zr,Ti)O_3$ (PZT) [75-76] or $BaTiO_3$ [77-78] exhibit a dipole moment in the absence of an external electric field. Another example is a relaxor oxide, e.g. $PbMg_{1/3}Nb_{2/3}O_3$ (PMN) [79-80], characterized by a ferroelectric response under high electric fields at lower temperature, but showing no macroscopic spontaneous polarization [81-82]. Both kinds of materials show a huge variation of their dielectric constants with temperature, which is undesirable for many applications. On the other hand, Ba and Pb-free materials with high dielectric constant values are increasingly attractive [83]. Most recently, several materials were reported to possess an extraordinarily high static dielectric constant above 10^4 which is weakly temperature and frequency dependent [84-86]. Such interesting investigations prompted the present work to perform a systematic investigation on the ternary system CuO-TiO_2-CaO. Since there are large technical demands for large dielectric constant materials, it is interesting to investigate systematically the dielectric properties of the composites in this ternary system, which certainly will shed light on the origin of the giant dielectric response.

2.4.2.1 $CaCu_3Ti_4O_{12}$

Subramanian et al. discovered that $CaCu_3Ti_4O_{12}$ possesses giant ε_r of 10^4, which is nearly constant below 1 MHz over a wide temperature range from -173 to 327°C [84]. This dielectric response makes such material ideal for a wide range of applications [87, 88].

The unit cell of $CaCu_3Ti_4O_{12}$ was identified in 1979 as a body-centred cubic perovskite-like structure (Fig. 2.3) with space group *Im3* and a lattice parameter of 7.391 Å [89-90]. Following the notation used for perovskite-related structure (general formula ABO_3), Ca^{2+} and Cu^{2+} ions share the A-site and Ti^{4+} occupies the B-site. The size difference between Ca^{2+} and Cu^{2+}, and their ordered occupation of the A-site, causes the TiO_6 octahedra to undergo substantial tilting, leading to a body-centred cubic supercell of space group *Im3* in which Ti^{4+} ions occupy centrosymmetric position in the octahedral sites. The angle of tilt is sufficiently large that the Cu^{2+} ions occupy an essentially square-planer environment [91].

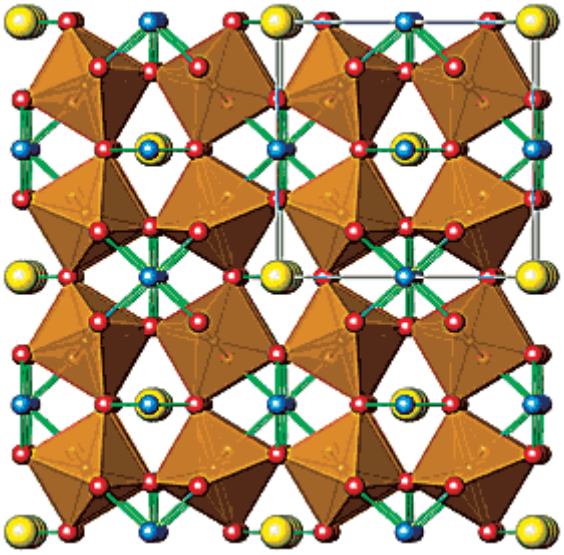

Fig. 2.3 The molecular model of $CaCu_3Ti_4O_{12}$, which shows the arrangement of atoms of calcium (yellow), oxygen (red), copper (blue), and titanium (black, at center of double-sided brown pyramids, or octahedra).

In the cubic perovskite structure encountered in $BaTiO_3$ above 120°C, the Ti^{4+} cation is located in the body centre of the structure. The structure is centro-symmetric and possesses no spontaneous dipole. Below 120°C, the cubic structure changes to the tetragonal structure [92-93]. The movement of Ti atoms inside the O_6 octahedra may be considered to be significantly responsible for the dipole moment. The site symmetry for Ti^{4+} in $CaCu_3Ti_4O_{12}$ is much lower

than that in cubic $BaTiO_3$; this greatly reduces the possibility of a ferroelectric phase transition based on the displacement of Ti^{4+} from the centre of its octahedron [84, 94, 95].

The origin of the peculiar dielectric phenomena in $CaCu_3Ti_4O_{12}$ is not fully understood. It could arise from both intrinsic and extrinsic factors. A local dipole moment associated with small off-center displacement of Ti^{4+} ions within the TiO_6 octahedra is an intrinsic factor. The transition to the ferroelectric state is frustrated by the octahedral tilt required to accommodate the square-planar coordination of the Cu^{2+} ions. Extrinsic effects arising from domain boundaries [96] and internal barrier layer mechanism (IBLC) are supposed to be the main contributions to the enhanced the dielectric response. This part will be further summarized in Section 2.4.3.

2.4.2.2 Other materials

A similar dielectric behaviour as for $CaCu_3Ti_4O_{12}$ was also found in CuO [97], Li, Ti doped NiO [81, 98], etc. Also, (Ca, Ta)-doped TiO_2 ceramics show ultrahigh $\varepsilon_r > 10^4$, and a grain-boundary atomic defect model was proposed to explain such a behaviour [99-102].

The interesting feature is that all these giant dielectric constant materials have similar dielectric behaviour to $CaCu_3Ti_4O_{12}$, i.e., they all exhibit a Debye-like relaxation and their dielectric constants are nearly independent of frequency and temperature well below the relaxation frequency [103]. Such weak frequency and temperature dependence of the dielectric response makes these materials quite attractive for applications in microelectronics [104].

2.4.3 Possible mechanism for the giant dielectric response

Since $CaCu_3Ti_4O_{12}$ and other materials with similar promising dielectric responses were discovered to possess giant dielectric constants [90, 105], which are independent of frequency and temperature in a large range, such properties are highly desirable for all applications of high-ε_r materials. The understanding of the mechanism underlying the behaviour of such

materials might lead to engineering of new high-ε_r materials with broad temperature and frequency independent dielectric response [106]. However, the origin of the giant dielectric constant is so far not understood. The following discussions have been focused on the reported possible mechanisms for the giant dielectric response for $CaCu_3Ti_4O_{12}$.

2.4.3.1 Intrinsic mechanism

There has been substantial debate about the intrinsic and extrinsic electrical properties of $CaCu_3Ti_4O_{12}$ since the original report by Subramanian et al [84]. The central question is whether the large dielectric response is intrinsic to a perfect crystal of $CaCu_3Ti_4O_{12}$ or extrinsic in that it originates with defects, inhomogeneities, etc.

"Intrinsic" means the large dielectric response would be present in a perfectly stoichiometric, defect-free, single-domain crystal of $CaCu_3Ti_4O_{12}$. Extrinsic effects mean the effects associated with the "real" microstructure, such as domain boundaries, defects, or other crystal imperfections [90, 107].

The dielectric constant of a material is related to the polarizability α, in particular the dipole polarizability, which arises from structures with a permanent electric dipole that can change orientation in an applied electric field. In general, a value of above 1000 is related to either a ferroelectric material that exhibits a dipole moment in the absence of an external electric field or to a relaxor characterized by a ferroelectric response under high electric fields at lower temperature, but no macroscopic spontaneous polarization [105, 108]. Both classes of materials show a peak of permittivity as a function of temperature. Usually large dielectric constants in perovskite materials are related to the atomic displacements within a noncentrosymmetrical structure, e.g. $BaTiO_3$ [84].

Capacitance measurements on single crystal and ceramics of $CaCu_3Ti_4O_{12}$ have shown a high and relatively temperature independent permittivity value of above 10^4 over a wide temperature range of ~100-600 K. Below 100 K, the permittivity drops rapidly to a value of ~100, but is not accompanied by any structural phase transition [109]. Both powder neutron diffraction and Raman spectroscopy data [110-112] show the structure to remain cubic and centrosymmetric between 25 and 1000°C [111]. The site symmetry for Ti^{4+} in $CaCu_3Ti_4O_{12}$ is

much lower than in cubic $BaTiO_3$ and the high permittivity may arise from local dipole moments associated with off-center displacement of Ti^{4+} ions but the transition to a ferroelectric state is frustrated by the TiO_6 octahedral tilt required to accommodate the square planar coordination of Cu^{2+} [91]. The intrinsic nature of the crystal has been questioned and essentially is contrary to the results based on the first principle calculations [113]. In addition, extrinsic explanation was further supported by an experimental measurement that the intrinsic dielectric constant of a perfect $CaCu_3Ti_4O_{12}$ single-crystal film is only about 100, which is much smaller that the giant value observed in polycrystalline samples ($\varepsilon_r > 10^4$) [114].

2.4.3.2 Extrinsic mechanism

In view of the experimental and theoretical difficulties associated with an intrinsic explanation, many puzzling aspects of the behaviour of $CaCu_3Ti_4O_{12}$ become easier to understand if one assumes that the large observed static dielectric response arises from extrinsic mechanisms, such as point, line, or planar defects, or more generally, with sample microstructure, morphology, and boundary layers [115].

A barrier layer structure with semiconducting areas encircled by insulating layers was established to explain the very large capacitance behaviour of both polycrystalline and single-crystal $CaCu_3Ti_4O_{12}$ [116-117]. Internal barrier layer capacitance (IBLC) has been considered as the most probable mechanism to explain the observed giant dielectric response [118]. The dielectric responses of such a structure essentially are characterized by the so-called interfacial polarization [119].

The insulating layers were not well justified. Regarding the insulating barrier layer of single crystals, locally planar twin boundaries, antiphase and compositional-ordering domain boundaries were proposed to be the possibilities for the barrier layers [119-120].

For polycrystalline materials, the barrier layers are presumably located at the interface between the sample and contact, or at grain boundaries [121-122]. Sinclair et al. [91] used impedance spectroscopy to demonstrate that $CaCu_3Ti_4O_{12}$ ceramics were electrically heterogeneous, consisting of semiconducting grains (with dielectric constant <100) and insulating grain boundaries. A simplified equivalent circuit can be thus obtained, which

consists of two parallel *RC* elements connected in series, one *RC* element, R_bC_b, representing the semiconducting grains and the other, $R_{gb}C_{gb}$, representing the insulating grain boundary regions [123]. The equivalent circuit is shown in Fig. 2.4 (a). The schematic diagram of a typical impedance complex plane plot obtained at room temperature for $CaCu_3Ti_4O_{12}$ ceramics is shown in Fig. 2.4 (b). In this case, the complex impedance plot should in principle reveal two semicircles, corresponding to the contributions of grain and grain boundary, respectively (Fig. 2.4(b)).

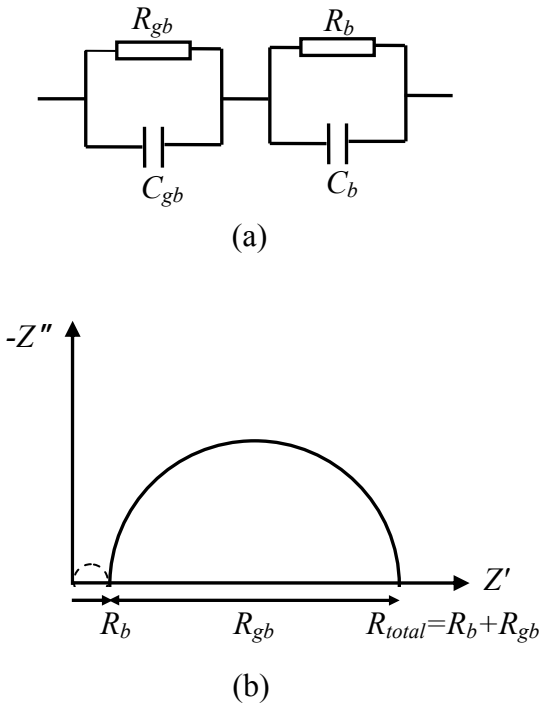

Fig. 2.4 (a) Equivalent circuit used to represent the electrical properties of grain and grain-boundary effects. Herein, R_g (R_{gb}) and C_b (C_{gb}) are resistivity and capacitance of grain (grain boundary), respectively. (b) The corresponding schematic impedance spectra according to equivalent circuit (a) [124].

In some cases, the electric response (the semicircle corresponding to the grain (bulk)) at higher frequencies is missing or only partially appears due to the limitation of the frequency range of the instrument. This study by impedance spectroscopy reveals the electrically inhomogeneous structure of the sample, which is a typical combination of the semiconducting grains with the insulating grain boundaries. Hence, this investigation supports the “extrinsic”

IBLC model as the origin of the high permittivity of $CaCu_3Ti_4O_{12}$ and also reconciled the "intrinsic" properties of $CaCu_3Ti_4O_{12}$. The barrier layers are supposed to be the grain boundaries. The influence of average grain size on the electrical properties of $CaCu_3Ti_4O_{12}$ ceramics has been reported [124-125]. Extremely high grain boundary permittivity value of ~280000 was obtained in the large grained (~100-300 μm) ceramics, which provided further support for the extrinsic IBLC mechanism of the dielectric response in $CaCu_3Ti_4O_{12}$ ceramics [124-125].

Electroceramics can be grouped into two categories (Table 2.1), depending on whether they are electrically homogeneous or heterogeneous [126-127]. For electrically homogeneous materials such as most ionically conducting ceramics, or microwave dielectrics, it is usually desirable to have high-density ceramics in which the grain boundaries have no influence on the electrical properties [128-129]. By contrast, materials such as varistors and barrier layer capacitors have properties that are controlled exclusively by the detailed chemistry and structure of "interfacial regions" at grain boundaries and grain surfaces [130]. It may be less important to achieve high density ceramics in such cases. For the characterisation of electroceramics, it is useful to distinguish between the ceramic microstructure that is seen by direct observation using electron microscopy and the electrical microstructure that is determined indirectly by techniques such as impedance spectroscopy [131]. Grains, especially at grain surfaces, may show small variations in composition that are responsible for the characteristic properties of varistors and barrier layer capacitors. Whereas it may be extremely difficult to detect such compositional variations by electron microscopy, these features are clearly present in the electrical microstructure and indeed, may dominate the overall electrical properties [126, 132].

Table 2.1 Electrical microstructure of electroceramics [126].

Electrically homogeneous	Electrically heterogeneous (grain boundary controlled)
Ionic conductors	Varistors
Mixed conductors	Barrier layer capacitors
High T_c superconductors	PTC thermistors
Microwave dielectrics	Gas sensors

As stated earlier, for the extrinsic mechanism, the barrier-layer model has been considered as the most favourable mechanism to explain the giant dielectric response in $CaCu_3Ti_4O_{12}$ material. According to the internal barrier layer capacitance model, the apparent ε_r of such an electrically heterogeneous ceramics can be approximated from

$$\varepsilon_r \approx \varepsilon_{gb}\left(\frac{d_g + d_{gb}}{d_{gb}}\right) \qquad \textbf{(2.5)}$$

where ε_{gb} is the dielectric constant of the grain boundary layer, d_g and d_{gb} are the thickness of the grains and grain boundary layers, respectively. Therefore, even a small ε_{gb} could lead to a giant ε_r if the ratio $(d_g+d_{gb})/d_{gb}$ is large [103, 133]. Accordingly, it can be easily understood that the bigger grains (larger d_g) with thinner grain boundaries (smaller d_{gb}) in the samples give higher dielectric constants (higher ε_r).

The development of insulating barrier layers at grain boundaries is widely accepted. However, the giant dielectric constants were also reported in single crystal $CaCu_3Ti_4O_{12}$. It would be contradictory for the giant dielectric response of $CaCu_3Ti_4O_{12}$ to have the dielectric response mechanism with different kinds of the origins, namely, the internal boundaries for the single crystal but the grain boundaries for the polycrystal $CaCu_3Ti_4O_{12}$. The recent discovery of internal domains inside the grains has indeed solved this contradiction, which also strongly suggested that the origin of the giant dielectric response of $CaCu_3Ti_4O_{12}$ is related to the barrier layer mechanism. Fang et al. observed internal domains inside grains [119, 134]. They proposed the possible existence of both domain boundaries and grain boundaries as the barrier layers to contribute the extraordinary dielectric response in $CaCu_3Ti_4O_{12}$ [119, 135]. The microstructural model [136] for the enhancement of the dielectric response of $CaCu_3Ti_4O_{12}$ has been schematically illustrated in Fig. 2.5 (a). The series-connected conduction path can be simulated by the equivalent circuit of Fig. 2.5 (b). In this case, the stained and composition-disordered domain boundaries could make up large energy barriers for hopping and be assumed to be insulating [136]. The discovery of the internal domains inside the grains of the polycrystalline $CaCu_3Ti_4O_{12}$ not only solves the contradictory explanation of the dielectric response between polycrystalline and sinlge-crystal, but also justified the extrinsic effect of the enhancement of the dielectric response of $CaCu_3Ti_4O_{12}$.

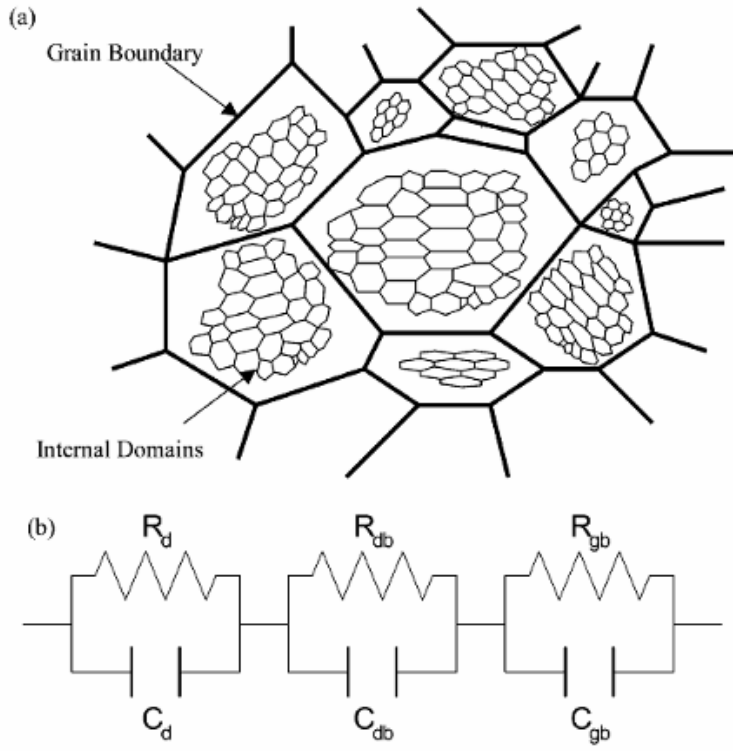

Fig. 2.5 (a) Microstructure model of polycrystaline $CaCu_3Ti_4O_{12}$ showing the internal domains inside the grains. (b) Equivalent circuit of (a). R_d, R_{db} and R_{gb} are the resistance of domain, domain boundary and grain boundary, respectively. C_d, C_{db} and C_{gb} are the capacitance of domain, domain boundary and grain boundary, respectively [136].

Though the origin of such dielectric behaviour is still open to debate, an internal barrier layer capacitor is generally considered as the most probable mechanism [97, 137]. Guillemet-Fritsch et al investigated dielectric properties of $CaCu_3Ti_4O_{12}$ based multiphased ceramics [138]. They proposed the presence of a copper oxide phase besides $CaCu_3Ti_4O_{12}$ was important for enhancing the dielectric property. Kobayashi et al. investigated the dielectric properties of two phase composites of $CaCu_3Ti_4O_{12}$ and $CaTiO_3$ [139]. A high ε_r (≈1800) with a low tanδ (≤0.02) below 100 kHz was obtained at $CaCu_3Ti_4O_{12}$: $CaTiO_3$ ratio of 2:1. A barrier layer of $CaTiO_3$ on the surface of the $CaCu_3Ti_4O_{12}$ grains was proposed to be the possible contribution of the high dielectric performance [139].

Chung et al. [140] used a combination of scanning Kelvin probe microscopy with a lateral bias and I-V measurements on pellets and across individual grain boundaries (using microcontact electrodes on individual grains) to demonstrate the presence of electrostatic barriers at the grain boundaries in $CaCu_3Ti_4O_{12}$ ceramics. The grain size-dependent breakdown voltage supports the IBLC mechanism.

Interfacial polarization occurs in electrically inhomogeneous systems. When an electric current passes through interfaces between two different dielectric media, because of their different conductivities, surface charges pile up at the interfaces, and give rise to a Debye-like relaxation process [141-142] under an external alternating voltage. A detected Debye-like relaxation response is therefore not necessarily the result of dipole relaxation in the system; sometimes it originates from the heterogeneity of the system [143]. For example, grain boundaries and/or the electrodes applied to the sample can produce the effect [121]. This effect could be conveniently described by an equivalent circuit and has been widely used to account for dielectric relaxations in many heterogeneous materials [103].

The IBLC model was also considered as the most favourable mechanism for the other materials with similar dielectric response, e.g. Li or Ti doped NiO [98], CuO [97], etc, although the location of the barrier layers is still open to scientific debate and needs to be further confirmed.

2.4.3.3 Other mechanisms

Insulating barrier layers arising from the Maxwell-Wagner relaxation of the depletion layers at the interface between sample and electrode contacts were also considered as possible contribution factors to the anomalously high dielectric constant of $CaCu_3Ti_4O_{12}$ [144]. However, the electrode contact effect was also not conclusive. Other reasons for the electrode contact effect to be discounted are that the dielectric responses of $CaCu_3Ti_4O_{12}$ are strongly affected by dopants and the microstructures observed [119].

3. Experimental

This chapter describes the detailed experimental work carried out in this thesis. It can be divided into three sections: (1) parallel synthesis of the ternary systems; (2) sol-gel process for representative candidates in the CuO-TiO_2-CaO system; (3) physical characterizations.

3.1 Parallel synthesis of the ternary systems

The basic idea to achieve a combinatorial library in a ternary system is shown schematically in Fig. 3.1. The ternary system Fe_2O_3-TiO_2-Al_2O_3 is chosen as an example to show the schematic arrangement for a ternary system. Three combined triangular pyramid-shaped layers (Fig. 3.1 (a)), produced by injection moulding, were stacked on top of one another (Fig. 3.1 (b)) and further separated by honeycomb cutting (Fig. 3.1 (c)), followed by subsequent mixing and heating treatment. The detailed procedures and parameters are introduced in the following sections.

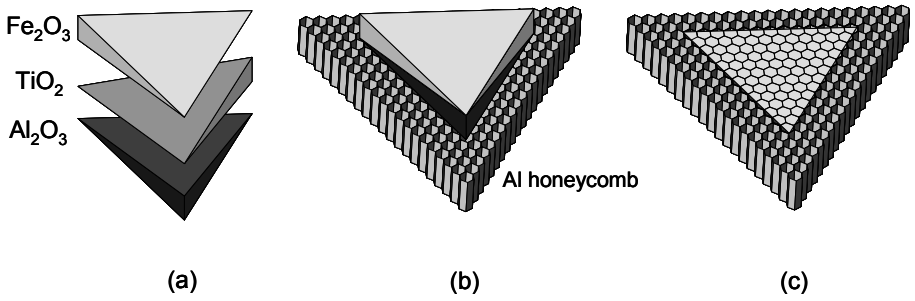

Fig. 3.1 Schematic arrangement of three component systems. (a) Fe_2O_3, TiO_2 and Al_2O_3 layers; each layer was individually produced by injection moulding from the mixtures of the corresponding solid powders, paraffin wax, surfactants; (b) the combination of three layers on aluminium honeycomb; (c) the combinatorial library made by honeycomb cutting.

3.1.1 Synthesis and combination of three layers

Starting materials used were alumina (Aluminiumoxid C, Degussa), titania (P25, Degussa) and iron oxide (1300M, Nordic pigments), $CaCO_3$ (SOCAL® 312, Solvay Chemicals), CuO (Nanostructured & Amorphous Materials Inc) powders with average particle size about 30, 50, 200, 60, 40 nm, respectively. The commercial powders were dried at 120°C overnight prior to mixing with the binder. The low-viscosity feedstock comprised of paraffin wax-based binder, ceramic powder (Fe_2O_3, TiO_2, Al_2O_3, $CaCO_3$ or CuO) and surfactant was prepared by using a kneader (Stephan, Hameln, Germany) with a 650 cm^3 bowl, and two sigmoidal, counter-rotating blades operating at 35 rpm (rotations per minute). The kneading time was 5 h.

It is important that the mixture is homogeneous, free of agglomeration and contains no porosity. Some processing parameters that can affect the homogeneity of the feedstock include: the type of the mixer and mixer blades, the mixing speed and the temperature, the mixing time and the sequence [145-146]. The binder and powder characteristics will affect homogeneity [147]. The detailed investigations in optimization of these factors were not included in this thesis.

The composition of each feedstock is listed in Table 3.1. Granulation of the feedstock was performed during cooling by continuously rotating the blades as the temperature dropped from 100°C to 40°C. The as-prepared feedstock was then fed into an injection moulding machine (Allrounder 220M, Arburg) to form triangular pyramid-shaped layer (see Fig. 3.1(a)). Note that the geometry of the middle layer with two isosceles triangle bases is different from the top and bottom layers with two equilateral triangle bases. The moulds were specially designed and produced by a mould producer (Formenbau Wollscheid, Nonnweiler) and are shown in Fig. 3.2. The moulding parameters for injection moulding process are listed in Table 3.2. Three layers composed of Fe_2O_3 (CuO), TiO_2, or Al_2O_3 ($CaCO_3$), respectively, were stacked on top of one another with a rotation of 120° to form a triangular prism with dimensions of base side 120 mm and height of 20 mm, as shown in Fig. 3.1(b).

Table 3.1 The blends compositions successfully used as feedstock in injection moulding:

MO_x	MO_x (wt%)	Paraffin wax (wt%)	Luwax V (wt%)	Surfactant (wt%)	Layer weight (g)
Fe_2O_3	88.34	8.43	3.24		130.2
Al_2O_3	59.55	18.66	16.16	5.63 (stearicamid)	63.8
TiO_2	73.52	16.17	6.84	3.47 (stearic acid)	80.9
CuO	77.60	15.74	6.66		105.7
$CaCO_3$	75.26	22.49		2.25 (fatty acid)*	72.1

* the commercial product of surface treated precipitated $CaCO_3$.

Table 3.2 Moulding variables to produce metal oxide layers used in this study.

Moulding variables	Value				
Metal oxide feedstock	Fe_2O_3	TiO_2	Al_2O_3	$CaCO_3$	CuO
Mould temperature	30°C				
Barrel temperature (feed to nozzle)	30-30-50-100-130°C				30-30-50-52-55°C
Injection pressure	~45 bar	~120 bar	~120 bar	~250 bar	~120 bar
Hold pressure	~35 bar	~120 bar	~120 bar	~250 bar	~120 bar
Hold pressure time	~5 s				
Cooling time	~15 s				

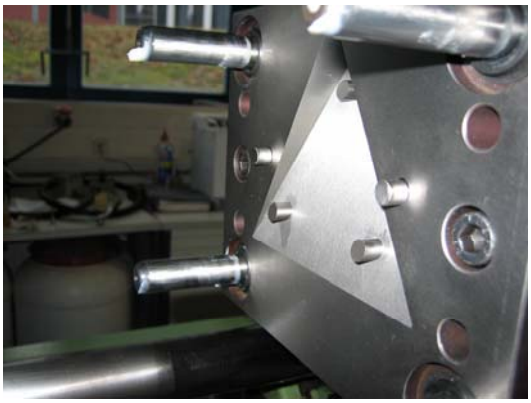

(a)

(b)

(c)

Fig. 3.2 The images of the moulds used to produce three layers in injection moulding. (a) the right half mould and (b) the pair of moulds for producing up/down layers; (c) the pair moulds with TiO_2 middle layer on one mould for producing middle layers.

3.1.2 Separation of library cells by honeycomb cutting

The stacked three layers were vertically put on top of an aluminium honeycomb (Euro-composites Co.) with a cell size of 6.4 mm (see Fig. 3.1(b)). To avoid the slipping of layers and honeycomb during cutting, an additional frame was used to stabilize the system. The frame made of aluminium alloy consists of two parts, one is to fix the honeycomb, and the other is to stabilize the three layers and their covers during cutting. The experimental set-up used to separate the library cells is shown schematically in Fig. 3.3. First of all, the honeycomb was fixed into the lower part of the frame. The injected three layers were directly put on top of the honeycomb, which was stabilized by the upper part of the frame. Silicone rubber (Strauch GmbH) with weighing paper sputtered by graphite, as an isolation to avoid the sticking of the layers to the cover, was then put on top of the three layers. Flexible silicone rubber was used to protect the edges of the honeycomb after the three layers were totally pressed into the honeycomb. Finally, a hard cover made of stainless steel was added on top of the silicone rubber. Subsequent heating of the as-obtained system at ~100°C for 20 min softened the three layers. Then the cover was slowly pressed to push the three layers into the honeycomb. Thus the separated library members were obtained in the honeycomb cells (see Fig. 3.1(c)). A total of 171 compositions were achieved in this library.

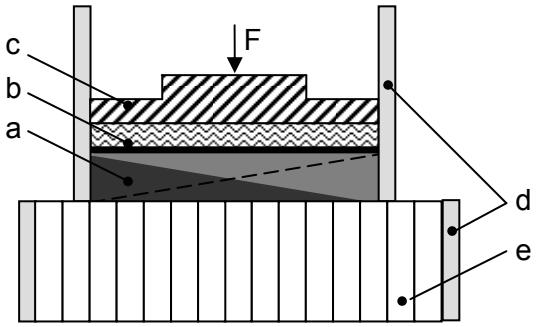

Fig. 3.3 Schematic experimental set-up used to separate the library cells. (a) injected three layers; (b) silicone rubber layer sputtered by graphite; (c) stainless-steel cover; (d) Frame made of aluminium alloy; (e) honeycomb.

(a) (b)

Fig. 3.4 Photographs of the failed honeycomb cutting.

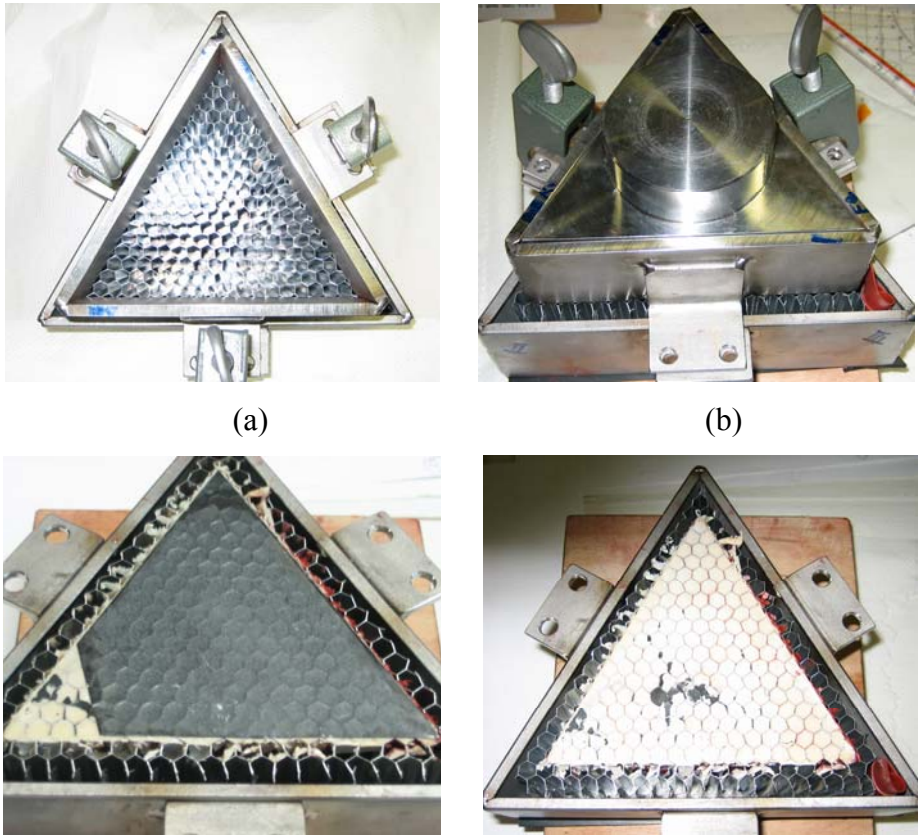

(a) (b)

(c) (d)

Fig. 3.5 Photographs of the set-up used to separate library cells in ternary system Fe_2O_3-TiO_2-Al_2O_3. (a) frame without cover, (b) full set-up with three layers inside the frame, (c) the product after honeycomb cutting with sputtered graphite paper on top, (d) the product after honeycomb cutting. Note that in (d), the black color on top of three layers is carbon graphite.

The key to avoid sticking of three layers on the cover is to use graphite sputtering layer. Additional requirements to get well cutted pieces after honeycomb cutting are to control the cutting speed and the force on the cover. Fig. 3.4 shows a failed cutting due to the sticking of the up layer to the silicon cover (seen in Fig. 3.4 (a)) and the distorted honeycomb due to the overloaded force above the cover (seen in Fig. 3.4 (b)). The successful honeycomb cutting was obtained during the slowly honeycomb cutting below 3 kN. The photographs of the experimental set-up to separate the library cells and the final product after honeycomb cutting are shown in Fig. 3.5. The Photographs of the successful honeycomb cutting products in the ternary system CuO-TiO_2-CaO are shown in Appendix 7.5.1.

3.1.3 Mixing and post treatment

In order to get a homogeneous mixture of each layered piece in the honeycomb cells, each individual layered piece was manually transferred to a self-made aluminium rack with 70 parallel wells of 10 mm in diameter and 30 mm in depth (The photograph of this aluminium rack is shown in the next chapter in Fig. 4.5 in Section 4.1.2). Certain amounts of decane and paraffin wax as a dilution agent were added in each well of the aluminium rack to aid the mixing. The final filling height of each well after adding dilution agents is ca. 2/3 of the total height of the well. The rack was covered by a silicone rubber and then clamped between two electric heating plates. The assembled system was fixed in a red-devil painter mixer (Chameleon M & T Machines Ltd.). The system was heated up to ~120°C by electric heating plates and shaken for 0.5 h at ~120°C. In this step, the binder inside each well of the rack was melted and the contained individual layered piece was mixed in the diluted wax-based solution. After half an hour mixing at ~120°C, the whole system was cooled down to room temperature during shaking, whereas the wax-based solution became solid again. Therefore the mixing status of the mixture in each well of the rack was easily kept in the wax-based system.

For the ternary system Fe_2O_3-TiO_2-Al_2O_3, the cooled mixtures were calcined in air at 500°C for 6 h with a ramping rate of 420°C/h to remove the contained organic components, followed by grinding in an agate mortar. This process was repeated one more time to improve the mixing. The powdered materials were manually pressed in a cylindrical steel die (8 mm in

diam.) at 80 MPa to thin pellets. The pellets were sintered in an air atmosphere at 1300°C with a ramp rate of 300°C/h for 70 h in alumina crucibles, and finally quenched in water.

For the ternary system CuO-TiO_2-CaO, the dielectric properties are very sensitive to microstructure. In order to get a more homogeneous mixture, a stainless steel ball (diameter: 6 mm) was put into each well of the aluminium rack to aid the mixing. The rack with cover was shaken in a red-devil painter mixer at 120°C for 0.5 h, and then cooled during shaking. After removal of the stainless steel balls, the mixtures were then individually transferred to alumina crucibles and calcined in air at 900°C for 6 h in order to remove the organic component and to decompose the contained calcium carbonate, followed by grinding in an agate mortar. This process was repeated 4 more times to improve homogeneity of the mixing. The as-obtained powder was pressed to thin pellets (diameter: 5 mm; thickness: 1.2~1.5 mm) under 5 kN, followed by cold isostatical pressing under 2000 kN for the densification. The pellets were sintered in static air at 950°C for 70 h, followed by cooling in the furnace. Some of the samples near the $CaCu_3Ti_4O_{12}$-rich region were also sintered in air at 1050°C.

Pellets, in stead of powder, were considered particularly effective for both the phase equilibrium studies and the dielectric properties studies ensuring rapid reaction resulting from intimate contact between the oxide particles.

3.2 Sol-gel process for representative candidates in CuO-TiO_2-CaO ternary system

$Ti(OiPr)_4$ (Sigma-Aldrich), $(CH_3COO)_2Cu{\cdot}H_2O$ (Sigma-Aldrich), and $(CH_3COO)_2Ca{\cdot}xH_2O$ (Merck) were individually dissolved in a mixture of 2-propanol and propionic acid (volume ratio of 1:1~1.5). Each resulting solution was refluxed at 150°C for 1h and then cooled down to room temperature. Stoichiometric quantities of the three solutions were mixed. The achieved solution was dried in an oven at 120°C over 48 h, then calcined at 500°C for 0.5 h, followed by calcination at 750°C for 2 h. After grinding in an agate mortar, the achieved powder was pressed to thin pellets (diameter: 5 mm; thickness: 1.2~1.5 mm) under 5 kN, followed by cold isostatical pressing under 2000 kN. The pellets were sintered at 950°C (or

1050°C) for 70 h, followed by cooling in the furnace. The flowing chart of this synthesis is shown in Fig. 3.6.

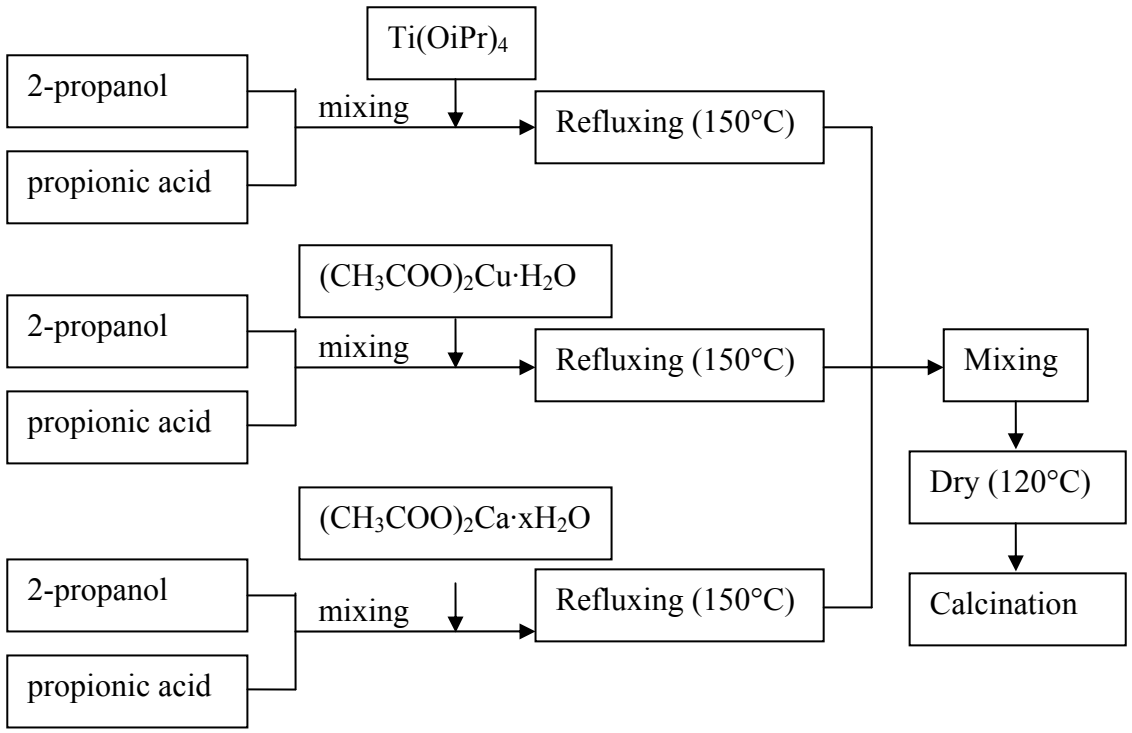

Fig. 3.6 Flowing chart for the synthesis of representative candidates in the CuO-TiO_2-CaO system by soft chemistry method.

3.3 Physical Characterizations

3.3.1 Phase relations determination

X-ray powder diffraction (XRD) measurements were carried out using Cu *Kα* radiation (λ = 1.54178 Å) in a Siemens D-500 diffractometer equipped with a graphite monochromator in the range from 15 to 65° in 2θ and a counting time of 4 sec/step. The relatively longer scan times were considered necessary, especially when close to phase boundaries, where the proportions of some phases may be at a minimum.

3.3.2 Microstructure and composition analysis

An SEM instrument (SEM, JEOL JSM 6400F) equipped with energy-dispersive X-ray spectroscopy (EDX) and optical microscopes (Olympus Optical Co. Ltd.) were used to observe the microstructure and determine the grain-grain boundary compositions of the sintered pellets.

Atomic ratios of the contained elements in the prepared samples were analysed by using atomic emission spectroscopy (ICP-AES, Horiba Jobin Yvon GmbH).

3.3.3 Electric property testing

Room-temperature capacitance (C) and loss tangent ($\tan\delta$) of the samples were measured with a parallel-plate capacitor arrangement using Agilent 4284A precision LCR meter from 10^2 to 10^6 Hz. The sample's surfaces were coated with silver conducting paint to ensure good electrical contacts with the electrodes. The capacitance and loss tangent were carried out as a function of frequency (10^2-5×10^6 Hz) and temperature (25°C to 130°C), using an Agilent 4294A precision impedance analyzer at an oscillation voltage of 100 mV. The complex permittivity, ε^*, was calculated according to equations (2.1) to (2.4).

The complex impedance Z^* was calculated as follows

$$Z^* = Z' - iZ'' = \frac{1}{i\omega C_0 \varepsilon^*} \qquad \textbf{(3.1)}$$

where ω is the angular frequency $\omega = 2\pi f$ and $i = \sqrt{-1}$. $C_0 = \varepsilon_0 A / d$ is the capacitance of free space.

Direct current (DC) resistivity was measured by Model 2425 100W SoureMeter (KEITHLEY).

3.3.4 Other properties

Pellet densities were measured by the Archimedes method. The decomposition of organic components was analysed by TG-DSC (Netzsch STA 449 C).

4. Results and Discussion

The results obtained in this work are presented and discussed in the following chapter. Five sections are included: the development and reliability of the new parallel synthesis strategy (Fe_2O_3-TiO_2-Al_2O_3) in Section 4.1; the subsolidus phase relations (CuO-TiO_2-CaO) in Section 4.2; dielectric properties investigations (CuO-TiO_2-CaO) in Section 4.3; possible mechanism for the giant dielectric constant response in Section 4.4; the dielectric property investigation of the promising composites synthesized by sol-gel process in Section 4.5.

4.1 Parallel synthesis for the Fe_2O_3-TiO_2-Al_2O_3 ternary system

4.1.1 Microstructure difference

Fe_2O_3, TiO_2, Al_2O_3 with average particle size of 200, 50, 30 nm were used to produce the corresponding feedstock for injection moulding. Paraffin wax, Luwax V and the surface modification agents were added as binder in the feedstock. The corresponding compositions for each feedstock are listed in Table 3.1. The microstructure difference between original powder and the corresponding feedstock is shown in Fig. 4.1. The powders are closely packed together after kneading with the binder. The Fe_2O_3 powder with submicron particle size seems to be easier to get organized structure after mixing with its binder. No apparent agglomerates are formed in the Fe_2O_3 feedstock after kneading (right images of Fig. 4.1 (a) and (b)) compared to the microstructure of the original commercial powder product (left images of Fig. 4.1 (a) and (b)). The Fe_2O_3 particles are well arranged and packed with the modification of the binder. In comparison, though apparently dense structure are obtained, the microstructure of the TiO_2 and Al_2O_3 feedstock (seen in right images of Fig. 4.1 (c) and (d)) shows clear agglomeration of the primary nanoscaled particles (seen in left images of Fig. 4.1 (c) and (d)) after kneading with the corresponding binder.

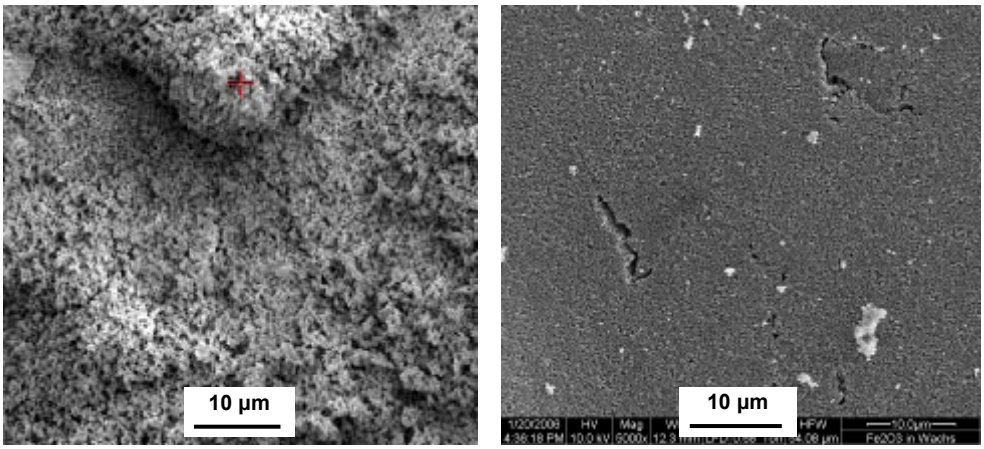

(a)

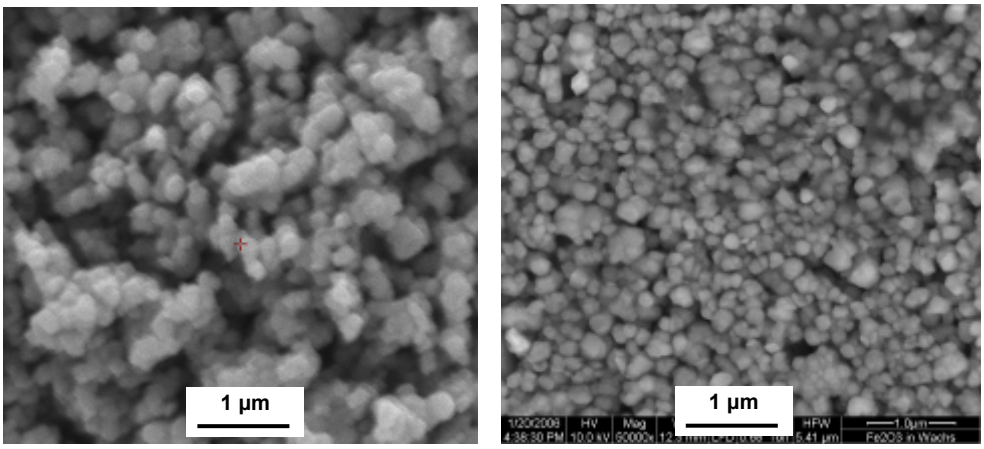

(b)

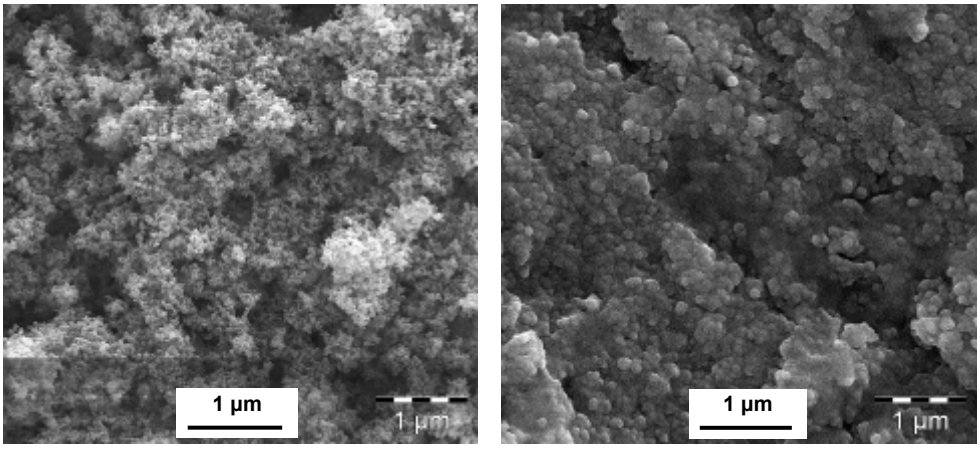

(c)

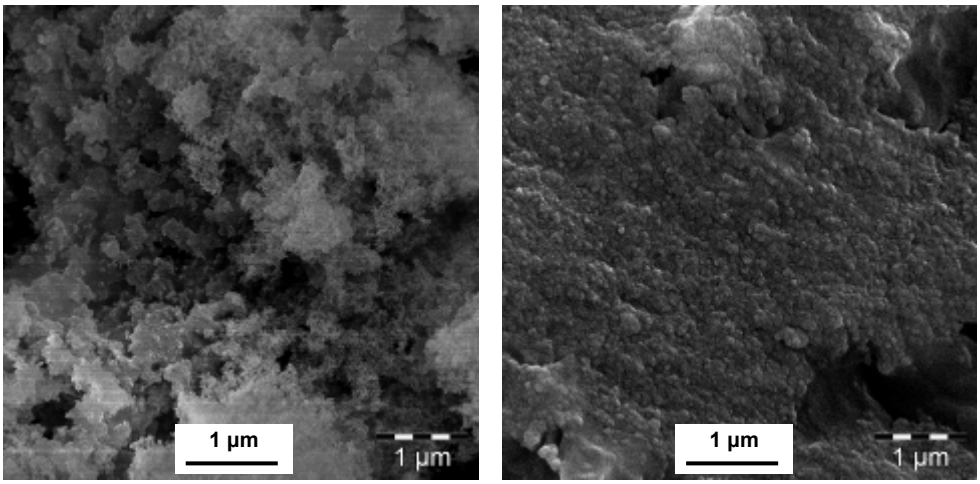

(d)

Fig. 4.1 SEM images of original powder (left) and the corresponding feedstock (right) of Fe_2O_3 with magnification of (a) ×5000, (b) ×50000, respectively, and (c) TiO_2, (d) Al_2O_3.

The chemistry of binder systems has a major influence on the success of powder injection moulding [148]. The binder system used for powder injection moulding usually comprises the components of polymers, waxes, plasticizers, and surfactants [149]. A proper surfactant can enhance the dispersion of powder in the binder during mixing, which in turn results in enhanced powder loading [150]. For Fe_2O_3, no extra surfactant was needed in preparation of the corresponding blend. The operation curves during injection moulding for Fe_2O_3 feedstock are shown in Fig. 4.2. The Fe_2O_3 feedstock was fed into injection moulding machine to form test bars of dimensions of 80 × 20 × 2.5 mm. The smooth curves of injection pressure and feeding amount during time exhibit the good rheological properties of the feedstock during injection.

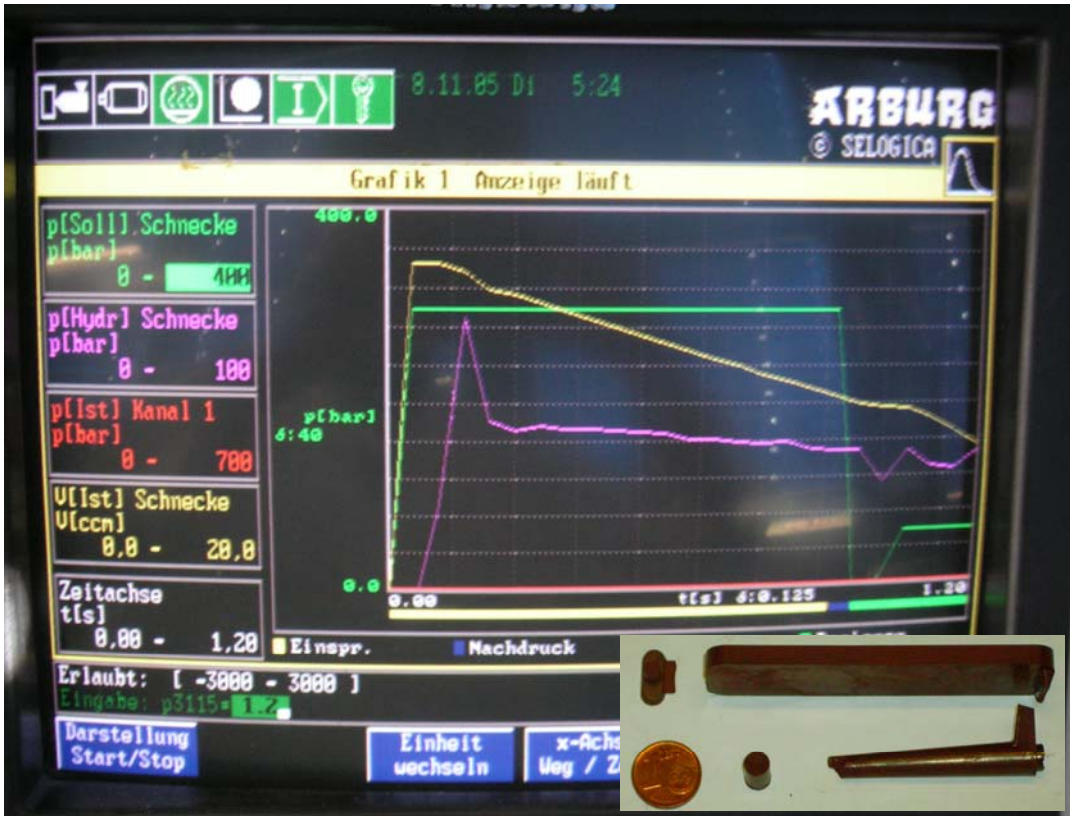

Fig. 4.2 The operation curves during injection moulding for Fe_2O_3 feedstock. — (pink) injection pressure, — (yellow) volume of ceramic feedstock in barrel. The right-bottom insert is the test bar from injection moulding. The smooth curves of injection pressure and feeding amount during time exhibit the good rheological properties of the feedstock during injection.

It is deduced that Luwax V, polyvinyl ether with a waxy consistency, can be possibly acting as a surface modification agent, to improve the binding between Fe_2O_3 powder and wax. The principle structure for polyvinylether is shown in Fig. 4.3. There is no information in the literature concerning the use of Luwax V, as a binder additive for the powder injection moulding. It was firstly used in powder injection moulding by Kraus [56]. In her thesis, the possible liquefying effect of Luwax V was concluded. In the present work, the interesting function of Luwax V with metal oxide powder is also suggested. Since the structure of Luwax V contains both polar group and unpolar group, the interactions both with unpolar substance as paraffin wax and with polar substance as metal oxide make this material serve as surface modification agent between wax and metal oxide. Such effect provides Fe_2O_3 feedstock with

good rheological properties during injection process, which was testified by injection moulding (Fig. 4.2).

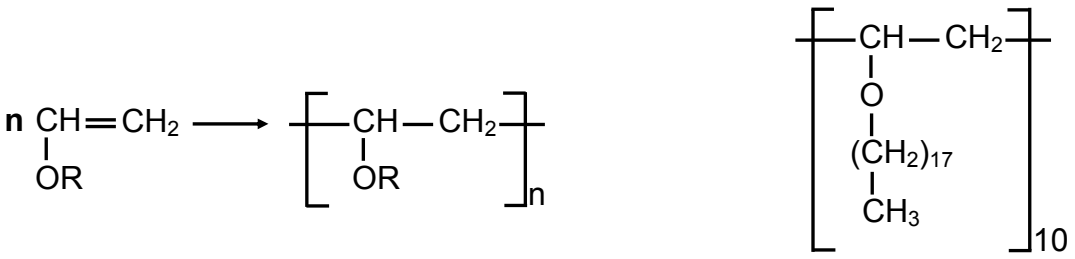

Vinylether polyvinylether octadecylpolyvinylether (Luwax V)

Fig. 4.3 Principle structure for polyvinylether (left image). The polyvinylether Luwax V has C18-side chains (right image) [56].

Typical particle sizes encountered in powder injection moulding are in the range of 0.1-15 μm [50]. Nanoscaled powder ceramics exhibited significant advantages over coarser-grained ceramics since lower sintering temperature may be possible when using nanosize rather than microsize particles [53-54]. However, little information concerning the processing of powders with particle sizes <100 nm has been reported due to their big specific surface area and the tendency to form agglomerates, which alter the flow behaviour of the feedstock, especially when high solid loading contents are required [56]. The application of the nanoscale powders in injection moulding technique has been investigated by Kraus [56]. Here, referred to Kraus' work, stearic amide is chosen as surfactant to produce a homogeneous blend for Al_2O_3 powder and stearic acid for TiO_2 powder, which have been well studied by Kraus. The initial particle size of these two powders are 30, 50 nm, respectively. As seen from Fig. 4.1 (c) and (d), both TiO_2 and Al_2O_3 feedstock show certain extent of agglomeration of the primary nanoscaled particles after kneading with the corresponding binder.

Deagglomeration can occur by two possible mechanisms. One is rupture, characterized by an abrupt splitting of agglomerates into a number of fragments, and the other is erosion, characterized by a continuous detachment of small fragments from the agglomerate occurring

at a lower stress compared with rupture [151]. Since the observed agglomerates in the alumina and titania feedstock are not formed during the powder production stage, in which constitute grains (particles) sintered into hard agglomerates, the agglomerates in alumina and titania systems are attributed as soft agglomerates, held together primarily by van der Waals forces [152]. Deagglomeration of ceramic can be realized by a combination of rupture and erosion during mixing. Reduction in the agglomerate size is due to the force imposed by the flow field, also referred as hydrodynamic stress, which the cohesive forces tend to maintain the integrity of the agglomerates. The nature of deagglomeration, by erosion or rupture or a combination of both, depends on the magnitude of stress generated in the mixing state [153]. Such hydrodynamic stress experienced by the feedstock should exceed the cohesive strength of the cluster for deagglomeration to occur. In the present study, in the case of alumina and titania feedstock preparation, the primary particles have not been well dispersed in the wax-based binder system and certain amounts of agglomerates formed during kneading. In addition, the hydrodynamic force is possibly insufficient to induce the agglomerate rupture due to the absence of high shear force in the mixture. The particle agglomerates still exist in some extent, but below 250 nm. The primary particle size of Fe_2O_3 powder is 200 nm. Therefore, even the agglomerates exist in TiO_2 and Al_2O_3 feedstock, they are good enough for the subsequent investigations, which also will be proven later in the final phase relationship determination in the ternary system. Finally, based on the existing results, each well-mixed feedstock of the corresponding metal oxide powder was fed into injection moulding machine to be shaped into the triangular pyramid-shaped layer for further investigations. The products from injection moulding are shown in Fig. 4.4.

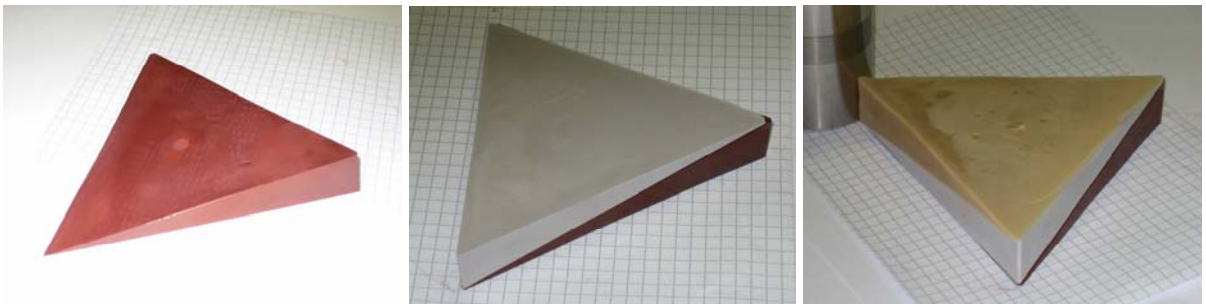

(a) (b) (c)

Fig. 4.4 Photographs of the injected three layers (a) Fe_2O_3 layer, (b) two layers of Fe_2O_3 (bottom layer) and TiO_2 (top layer), (c) three layers of Fe_2O_3 (bottom layer), TiO_2 (middle layer), and Al_2O_3 (top layer).

Once the three layers from Fe_2O_3, TiO_2 and Al_2O_3, respectively, have been produced by injection moulding process, they were stacked on top of one another on a honeycomb board for the subsequent honeycomb dividing process in order to get individual compositions inside the ternary system. The process is introduced in detail in the experimental part in Section 3.1.2.

4.1.2 Mixing of three components

After honeycomb cutting of the three combined layers, the individual composition in the ternary system locates inside the honeycomb net. The mixing of each individual composition in the corresponding cell of the honeycomb is the next challenge to get the final combinatorial library for the ternary system.

In-situ mixing of each layered piece inside the honeycomb board has been tested, but failed. The difficulties in such process lie in mainly two aspects. The mixing of three components in each cell of the honeycomb has to be realized by adding dilution agents in order to decrease the viscosity or the binding force between different components and inside each component. After adding dilution agents, the honeycomb board was sealed in both sides by silicon rubber and fixed between two heating plates. The whole system was then clamped into “Red-devil” paint mixer. The mixing was carried out above the melting point of the organic components. In practice, though it seems that in-situ mixing can save energy and time during the mixing step, it is rather difficult to handle in-situ and control the added dilution agents in each cell of the honeycomb without flowing away from the honeycomb board. Furthermore, the mixing has to be performed above the melting point of the organic components in the mixture. Above 120°C, honeycomb cannot mechanically keep the sealing condition due to the partial burning of the binder, which is one of the components of the commercial honeycomb board product. Therefore, the layered piece, which needs to be mixed well above the melting point of the organic components in the feedstock, will flow away due to the bad sealing condition provided by the honeycomb at higher temperatures. Based on the above limitations and handling-difficulties for in-situ mixing, ex-situ mixing is chosen to achieve the final combinatorial library.

The ex-situ mixing procedures by using additional self-made aluminium rack with 70 parallel wells are introduced in the experimental part (Section 3.1.3). Each layered piece has to be mixed above the melting point of the organic components after adding certain amounts of decane and paraffin wax as dilution agents. The binder inside each well of the rack was then melted at high temperatures (ca. 120°C) and the contained individual layered piece was mixed in the diluted wax-based suspension. After mixing, the whole system was cooled down to room temperature during shaking, and then the wax-based binder system became solid again. Hence, the mixing status of the mixture in each well of the rack was easily kept in wax-based system. Fig. 4.5 shows the pictures of the mixed products in the aluminium rack. After mixing, the cooled mixtures became solid again. Two of the mixtures were taken out of the rack and shown in the glass bottles in the right-top image of Fig. 4.5.

Fig. 4.5 Ex-situ mixed products of the layered pieces in the self-made aluminium rack. Left image is the silicone rubber cover for the rack. Inside the well of the rack is the cooled mixture for different compositions (right-down image). Two of them were taken out and transferred into a glass bottles in order to show the status of the mixture (right-up image).

It is worthwhile to mention the advantages to use paraffin wax as a medium to produce the library. The mixing of library members is realized by a paint mixer above the melting point of the organic vehicle based on paraffin wax. The final mixing status is kept in the cooled solid

organic vehicle. The sedimentation, which probably happens in nano-powder suspensions during aspirating-dispensing by the robot, seems not to be a problem because the particles are totally "fixed" in the solid organic vehicle. One problem existing in the present method is that, demixing might occur during the thermal treatment of the mixtures. Therefore, the fast thermal treatment for the purpose of quick removing the organic components after mixing was chosen in the present work in order to reduce the possibility of demixing. Furthermore, the splashing during the quick burning of organic components might also prevent the possible demixing.

The final mixture with composition of Fe : Ti : Al = 30.1 : 33.8 : 36.1 as an example before thermal treatment is analyzed by EDX analysis, as shown in Fig. 4.6. The position in the mixture for the EDX analysis was randomly picked from the mixture. At lower magnification, the mixing follows the estimated the composition. At higher magnifications, the homogeneity of mixing becomes worse. Though nanoscaled powder was used to prepare the corresponding feedstock, nano particles were not totally dispersed in wax-based binder system since submicron agglomerates were observed in alumina and titania feedstocks (Fig. 4.1), which has been discussed in Section 4.1.1. It is supposed that the final mixture contains three different metal oxide powders with submicron particle sizes. Therefore, the mixing below one micron range (×400000, Fig. 4.6) is not reachable. The final homogeneity of mixing has been further improved by repeating the process of grinding in an agate mortar and calcinations at 500°C.

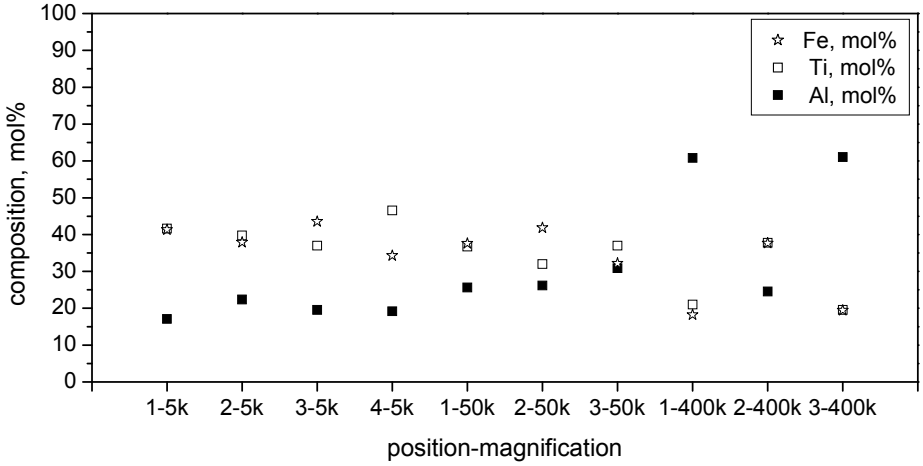

Fig. 4.6 EDX analysis of different positions in magnifications of ×5000, ×50000, ×400000 for the mixture with composition of Fe : Ti : Al = 30.1: 33.8 : 36.1. Number of x-axis was defined by "position - magnification".

4.1.3 Composition analysis

In a three-layer unit of the Fe_2O_3-TiO_2-Al_2O_3 ternary system, each composition in this library depends on its geometric position in the honeycomb and the content of contained metal oxide in each layer. The total thickness at any cell along the honeycomb net is equal to the sum of the individual thicknesses, which vary proportionally from cell to cell. The composition in molar fraction in each cell of the honeycomb is calculated with the solid loading in the corresponding feedstock, the molecular weight of the components, and the individual thickness ratio of central point in the respective cell within the honeycomb net and is visualised in Fig. 4.7. The mathematical calculations and geometric analysis to get each composition inside the honeycomb are introduced in Appendix 7.4. As the amount of contained metal oxide in each layer depends on the solid loading in the corresponding feedstock and the respective molecular weight, the distribution of compositions in the library is not in equal increments. Experimental compositional verification for the sintered samples using ICP-AES measurements was done to demonstrate the consistency between the calculated and the measured composition values. Table 4.1 shows the ICP-AES results of the several tested samples. The relative errors are below 12 %. This error can be explained by the slight shifting of three layers during the honeycomb cutting, which might be further minimized by careful adjustment of cutting speed. On the whole, the tendency of the compositional spreading in the whole library analyzed by ICP-AES is consistent with the expected calculated composition values.

Table 4.1 ICP-AES composition analysis of some samples in the library compared to the calculated values.

Samples	Calculated, mol%			Measured, mol%			Error, % *		
	Fe_2O_3	TiO_2	Al_2O_3	Fe_2O_3	TiO_2	Al_2O_3	Fe_2O_3	TiO_2	Al_2O_3
a	78.45	14.30	7.25	76.11	15.67	8.22	-3.0	8.7	11.8
b	53.21	28.82	17.97	54.80	28.21	16.99	2.9	-2.1	-5.8
c	51.52	34.34	14.14	53.61	33.52	12.87	-2.1	-2.4	2.9
d	26.07	27.15	46.78	28.03	28.93	43.04	-2.4	6.1	3.9
e	25.06	33.94	41.00	28.54	37.09	34.37	6.1	8.5	7.0

* Error = (measured-calculated) / measured

4.1.4 Phase relations in the Fe_2O_3-TiO_2-Al_2O_3 system

To compare the novel parallel synthesis method with conventional solid state reaction method, the similar sintering conditions as that of Pownceby et al. [58] are chosen. The phase relations of the samples in the Fe_2O_3-TiO_2-Al_2O_3 ternary system sintered at 1300°C are presented in Fig. 4.7. Seven phase regions, marked by different symbols, can be identified. These regions can be attributed to hematite solid solution (empty triangle) at Fe_2O_3-rich composition, a continuous pseudobrookite-structure solid solution (empty circle) between Fe_2TiO_5 and Al_2TiO_5, a tri-phasic region (the assemblage of hematite, pseudobrookite and conrundum), and four bi-phasic regions.

In the XRD patterns of the two samples near Al_2TiO_5 in pseudobrookite-structure solid solution between Fe_2TiO_5 and Al_2TiO_5, both rutile and conrundum in very small amounts are also observed besides pseudobrookite-structure. It is possible that due to the sluggish reaction the equilibria were still not achieved. Above the decomposition temperature at 1281±1°C, which was determined by Kato et al., [154] the further reaction to Al_2TiO_5 is possible in an oxidizing atmosphere [155]. Furthermore, Fe_2O_3 can serve as stabilizer in this reaction [156]. Therefore, longer treatment might be needed for the complete conversion. The phase relationships reported by Pownceby et al. [58] are also shown in Fig. 4.7. The phase boundaries with the same phase distribution regions are demonstrated by dashed lines in Fig. 4.7. Our results closely follow the previously reported phase relations constructed by a series of discrete data points obtained by conventional methods. The consistency with the previous report proves the reliability of the phase relationship analysis developed by the new combinatorial technique.

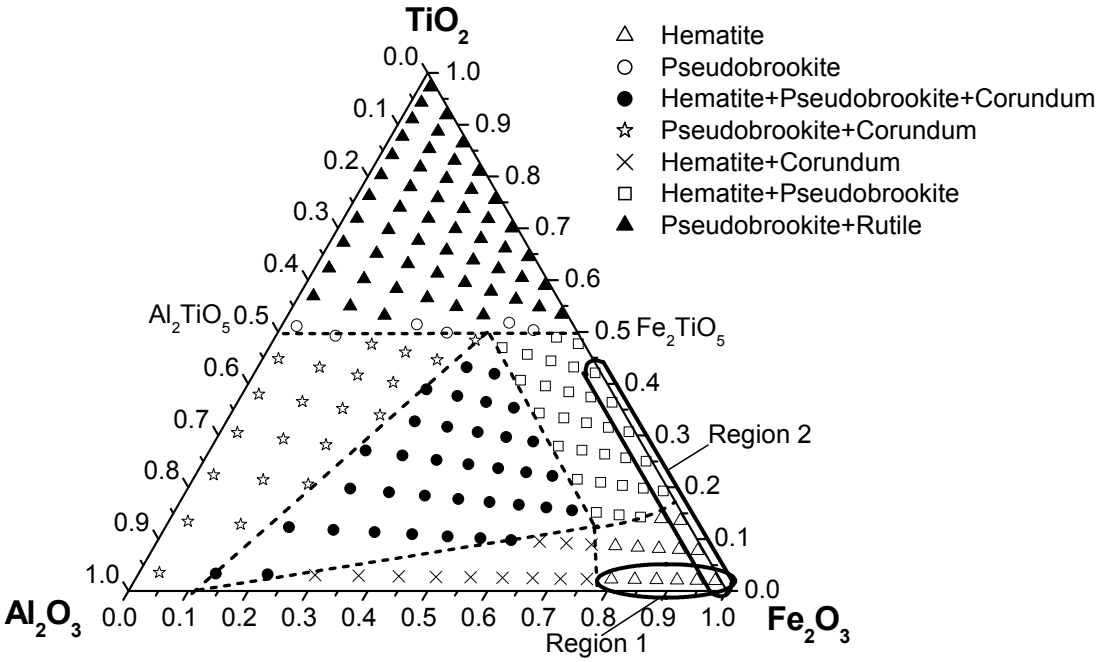

Fig. 4.7 Compositions (mol %) and phase relationship for combinatorial library prepared by injection moulding technique in the system Fe_2O_3-TiO_2-Al_2O_3 in air at 1300°C. The dashed lines are phase boundaries reported by Pownceby et al. [58]

The representative XRD patterns for details of structural changes and progression are demonstrated in Fig. 4.8 and Fig. 4.10. Fig. 4.8 shows the six selected XRD patterns of samples which are indicated along the Fe_2O_3-Al_2O_3 edge in hematite solid solution in Fig. 4.7 (Region 1). These patterns exhibit the same rhombohedral structure. No alumina or titania phases are detected. With the replacement of ferric oxide by alumina, a shift of the diffraction peaks towards higher 2θ values is observed. The variation of the lattice parameter of these samples as a function of aluminium atomic content was obtained by Rietveld analysis and is shown in Fig. 4.9. The lattice parameters exhibit a linear decrease with increasing aluminium content. This is attributed to the relatively smaller ionic size of Al (0.054 nm) replacing the larger ionic size of Fe (0.065 nm) which results in a shrinkage of the lattice edges [157].

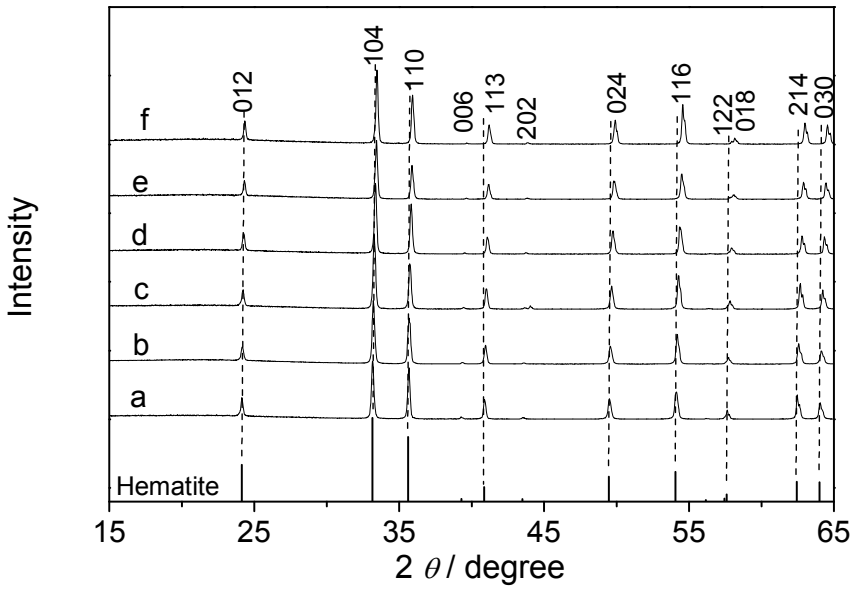

Fig. 4.8 XRD patterns of samples in Region 1 of Fig. 4.7 with composition (molar fraction) of Fe_2O_3 : TiO_2 : Al_2O_3 in starting mixtures of (a) 97.0 : 2.0 : 1.0, (b) 94.0 : 2.0 : 4.1, (c) 90.7 : 2.0 : 7.3, (d) 87.2 : 2.1 : 10.7, (e) 83.5 : 2.1 : 14.3, (f) 79.6 : 2.2 : 18.2.

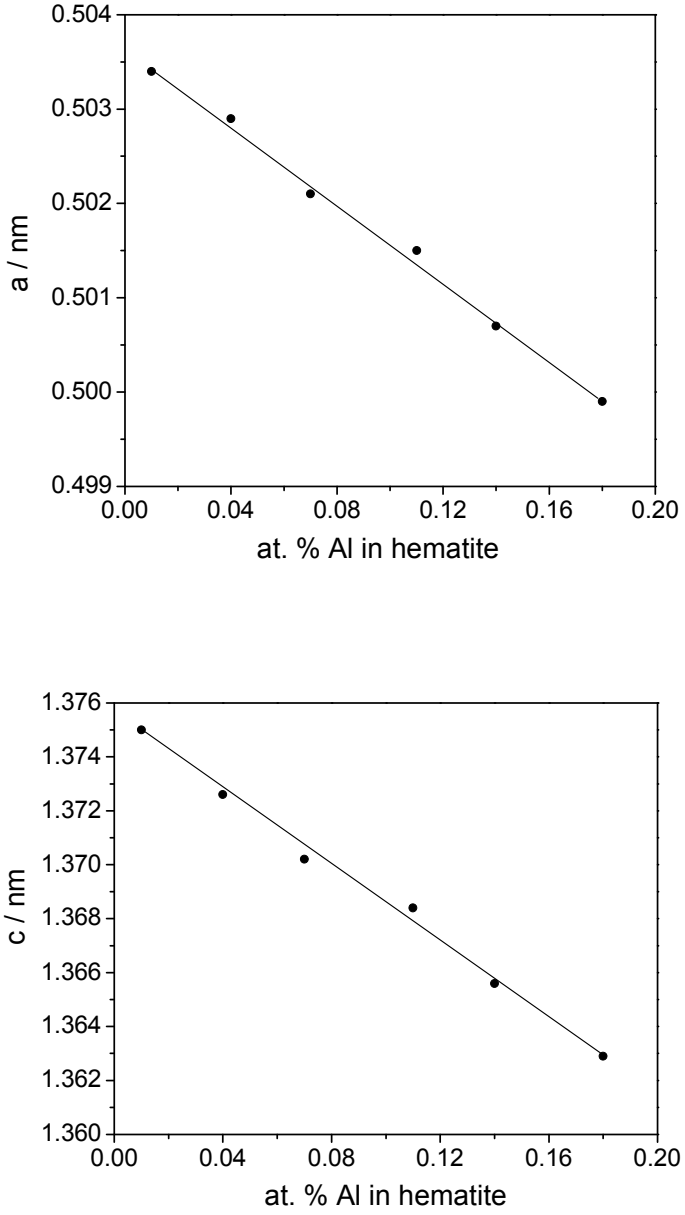

Fig. 4.9 The lattice constants *a* (top), *c* (bottom) as a function of Al atomic content in hematite solid solution in the samples in Fig. 4.8. The lattice parameters exhibit a linear decrease with increasing aluminium content. The shrinkage of the lattice edges is attributed to the relatively smaller ionic size of Al (0.054 nm) replacing the larger ionic size of Fe (0.065 nm) [157].

The XRD patterns of the samples, which are indicated along the Fe_2O_3-TiO_2 binary line from hematite solid solution to the bi-phasic region of (hematite + pseudobrookite) in Fig. 4.7

(Region 2), are presented in Fig. 4.10. When the three components form solid solutions as seen from pattern (a) to (c), the rhombohedral structure is the only phase. When the concentration of TiO_2 is above the solubility limit as seen from pattern (d) to (h), across the phase boundary, the intensity of the hematite phase decreases while that of the pseudobrookite phase increases with the concentration of TiO_2 increasing.

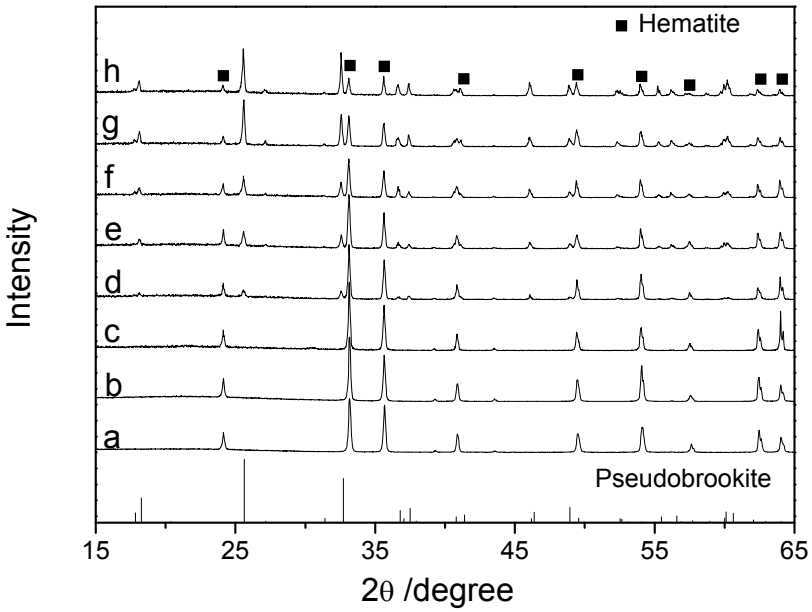

Fig. 4.10 XRD patterns of samples along the Fe_2O_3-TiO_2 edge from hematite solid solution to the bi-phasic region of (hematite + pseudobrookite), which are marked in Region 2 of Fig. 4.7. The composition (molar fraction) of Fe_2O_3 : TiO_2 : Al_2O_3 in starting mixtures are (a) 97.1 : 1.9 : 1.0, (b) 91.3 : 7.7 : 1.0, (c) 85.5 : 13.5 : 1.0, (d) 79.7 : 19.3 : 1.0, (e) 74.0 : 25.0 : 1.0, (f) 68.3 : 30.7 : 1.0, (g) 62.6 : 36.4 : 1.0, (h) 56.9 : 42.1 : 1.0.

Both the linear lattice parameter variation in hematite solid solution (Fig. 4.8 and Fig. 4.9) and the regular tendencies of the phase compositions variation (Fig. 10) across the phase boundaries in the ternary system Fe_2O_3-TiO_2-Al_2O_3 prove the reliability of the new parallel synthesis technique.

By controlling sintering conditions such as temperature and time, it is possible to obtain very different microstructures. Such control is very interesting in the design of materials for special

applications [158-160]. Three different particle size ranges are used in this system. Nanoscaled TiO_2 and Al_2O_3 and submicron scaled Fe_2O_3 are chosen as raw materials, based on two reasons, one is to show that the broader selection for raw materials could be applied in this new technique, the other is that the smaller particles could be inserted into the gap among bigger particles to get a more tightly packed structure [161]. The morphological difference in the high alumina, titania or ferric oxide content compositions of the prepared sintered library is illustrated in Fig. 4.11. Interestingly, a considerable influence arising from the bulk composition is observed. Composition at high Al_2O_3 content produces fine-grained assemblages and dense structures (Fig. 4.11 (c)). In contrast, Fe_2O_3-rich composition produces grain sizes averaging at 10-20 μm (Fig. 4.11 (a)). Even coarser grain sizes are observed in the high-TiO_2 bulk composition (Fig. 4.11 (b)). This differs with the investigation of Pownceby et al., [58] who reported near to or along the Al_2O_3-TiO_2 binary join, fine-grained assemblages, generally ≤2-3 μm in diameter, whereas Fe_2O_3-rich compositions grain size averaging 20-30 μm in diameter. Grain growth depends on several factors such as heat treatment, grain size distribution; grain morphology and the presence of second phases, etc. [162-164] The preliminary results obtained in this study suggest that a systematic study for the effect of heat treatment and sintering conditions on microstructure of the samples is required. Further investigation of this relationship is not included in this dissertation.

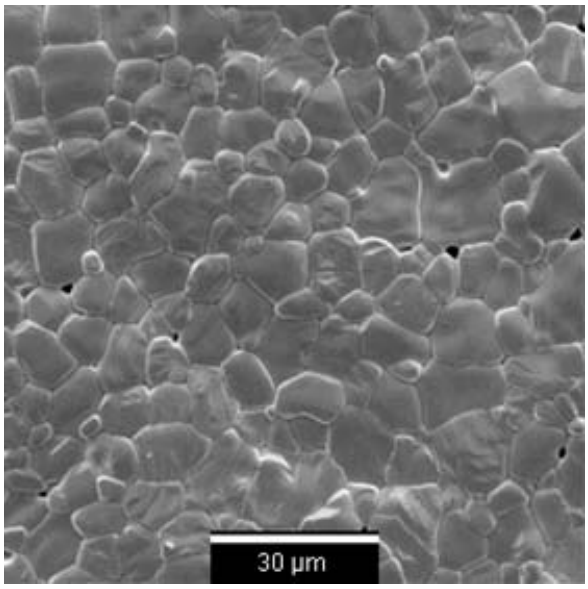

(a)

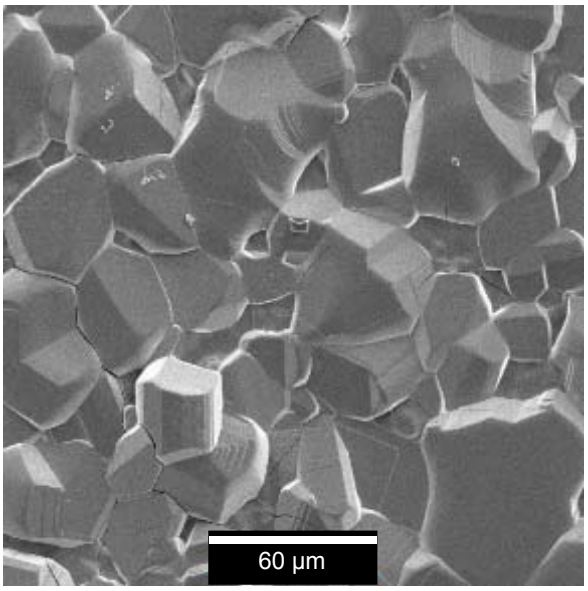

(b)

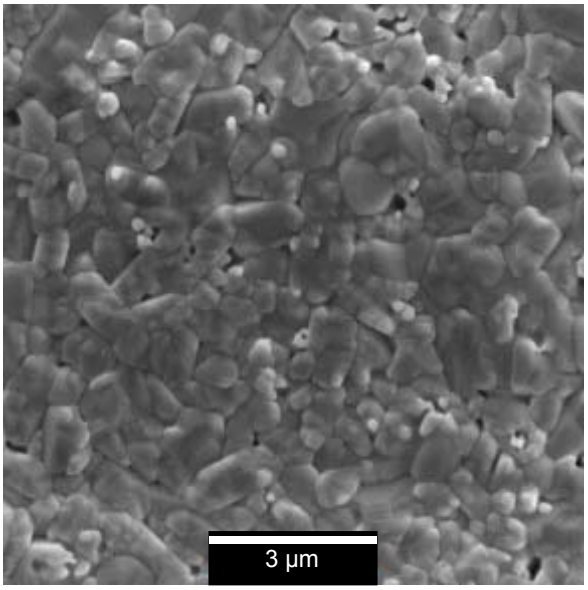

(c)

Fig. 4.11 SEM micrographs for sintered samples with the high alumina, titania or ferric oxide content compositions sintered in air at 1300°C. The starting compositions (molar fraction) of Fe_2O_3 : TiO_2 : Al_2O_3 are (a) 88.0 : 4.6 : 7.4, (b) 3.5 : 95.3 : 1.2, (c) 5.3 : 2.7 : 92.0.

Phase diagram mapping investigations by using the combinatorial method based on thin films [23-24], can be complicated by the possible interaction between the substrate and thin films and also by the difficulties of crystal structure identification due to strong textures which

often formed in the deposited films [165-166]. In comparison to thin film deposition technique, the products achieved by our technique suffer less from substrate influence and they are bulk-form ceramic materials. Therefore, the final libraries are applicable for the determination of bulk properties.

In the novel parallel synthesis technique, paraffin wax plays an important role to produce the combinatorial library. The organic vehicle based on paraffin wax produces the fluidity for the mixing of library members above the melting point of organic components and constrains the movement of the final mixtures in the cooled solid organic vehicle below the melting point. The sedimentation, which probably happens in nano-powder suspensions during aspirating-dispensing by the robot [35], seems not to be a problem because the particles are totally "fixed" in the solid organic vehicle. Demixing might occur during the thermal treatment of the mixtures. Fast thermal treatment for the purpose of quick removing the organic components after mixing is chosen in order to reduce the possibility of demixing. The splashing during the quick burning of organic components might also prevent the possible demixing.

The present work shows that injection moulding techniques can be used to produce highly-precise geometry to realize the three-dimensional composition spreading library. In a further step, the honeycomb cutting produces the library members and the mixing in the wax-based system is performed afterwards. In this flow, some factors may be modified, such as the choice of surfactant, the viscosity of the blends, the cutting speed, and the firing procedure etc. All those factors can influence the homogeneity of mixing and the maintenance of the mixing status during firing and finally influence the quality of the final mixtures. The detailed investigations concerning the optimization of above mentioned impacts have not been done in the present dissertation work.

In summary, a new parallel synthesis method by injection moulding technique to produce the compositionally spreading materials library followed by the honeycomb-dividing and mixing process has been developed. The ternary system Fe_2O_3-TiO_2-Al_2O_3 is chosen as an example to show the applicability of this new technique. The tendency of the compositional spreading in the whole library analyzed by ICP-AES is consistent with the expected calculated composition values. The similar phase relationship with previous reports, the regular tendencies and the linear lattice parameter variation in hematite solid solution prove the reliability of the new parallel synthesis technique. Paraffin wax-based organic media plays a

specific role in mixing due to their low melting point. Above the melting point, this medium provides free fluidity for mixing of the difference ceramic powders. Below the melting point, the medium is used to fix the mixed ceramic powders separated in space.

4.2 Phase relationship in CuO-TiO_2-CaO system

The discoveries of giant dielectric responses ($\varepsilon_r > 10^4$) in $CaCu_3Ti_4O_{12}$ and CuO, which are nearly both frequency and temperature independent over a large scale, make the ternary system CuO-TiO_2-CaO as potentially interesting system for dielectric property investigations. The composition and structure of phases within the CuO-TiO_2-CaO system should play an important role in the dielectric properties. Therefore, it seems to be quite meaningful to investigate the phases and their dielectric properties of the composites in the ternary system CuO-TiO_2-CaO systematically in order to find the possible new promising dielectric candidates and to reveal the composition-structure-dielectric property in this system. Up to now, no experimental phase relation investigation inside the ternary system CuO-TiO_2-CaO has been published. Since the reliability of the new parallel synthesis technique by injection moulding has been proven through the comparison of the phase relationship investigation in the ternary system Fe_2O_3-TiO_2-Al_2O_3 with the reports by the conventional method, this technique is further applied in the investigations of the phase relations and dielectric properties for the next ternary system, namely CuO-TiO_2-CaO.

The phase relationship in the ternary system CuO-TiO_2-CaO sintered at 950°C in air has been tentatively determined by XRD measurements. The results are shown in Fig. 4.12. The phase relationship in this system can be divided into five bi-phasic regions of $CaCu_3Ti_4O_{12}$+$CaTiO_3$, $CaTiO_3$+CuO, CuO+$CaCu_3Ti_4O_{12}$, $CaTiO_3$+Ca_2CuO_3, $CaCu_3Ti_4O_{12}$ +TiO_2 (seen in Fig. 4.12, lines ab, bd, da, bc, ae) and five tri-phasic regions of $CaCu_3Ti_4O_{12}$+$CaTiO_3$+CuO, $CaCu_3Ti_4O_{12}$+CuO+TiO_2, $CaCu_3Ti_4O_{12}$+$CaTiO_3$+TiO_2, $CaTiO_3$+CaO+Ca_2CuO_3, $CaTiO_3$+Ca_2CuO_3+CuO (seen in Fig. 4.12, regions I to V). The $CaCu_3Ti_4O_{12}$ compound is the only ternary oxide phase under these conditions in the investigated system.

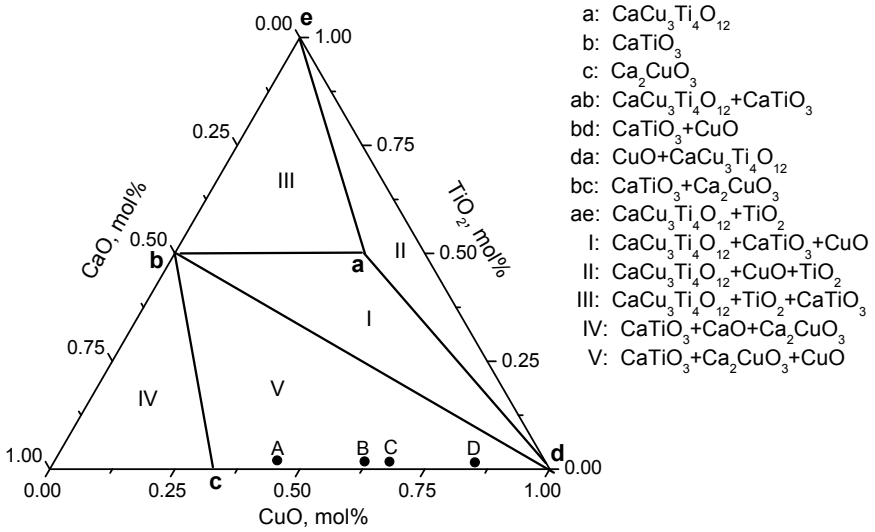

Fig. 4.12 Phase relationship in ternary system CuO-TiO_2-CaO at 950°C in air. The phase relationship analysis is based on compositions shown in Fig. 4.14. The XRD patterns of the samples A, B, C, D in phase region V are illustrated in Fig. 4.13.

Compared to the computed phase relations at 1000°C, [65] a disagreement existed about the number of possible compounds from $CaTiO_3$ to CaO. Though the CaO-rich compounds of $Ca_3Ti_2O_7$ and $Ca_4Ti_3O_{10}$ were evaluated to be present at $1 \geq P_{O2}/P_0 > 0.165$, no experimental evidence was given so far. The powder diffraction patterns of $CaTiO_3$, $Ca_3Ti_2O_7$ and $Ca_4Ti_3O_{10}$ are very similar [167-168]. A reflection near 18.2° (2θ) in the powder pattern of $Ca_3Ti_2O_7$ appears to be convincing evidence of the uniqueness of this composition [62]. Since most of the diffraction peaks of $CaTiO_3$ and $Ca_4Ti_3O_{10}$ overlap at higher 2θ angles, the diffraction patterns between $CaTiO_3$ and $Ca_4Ti_3O_{10}$ can be distinguished at the portion of the X-ray diffractogram below 30° (2θ) [169-170]. The most convincing evidence to identify $Ca_4Ti_3O_{10}$ is the reflection of x-rays from the diffraction from (006) ((near 19.6° (2θ)). Neither case of the patterns particular to $Ca_3Ti_2O_7$ and $Ca_4Ti_3O_{10}$ is observed in this study. It should be noted that the compound $Ca_3Ti_2O_7$ does not form readily at temperatures below 1500°C [171-172]. The compound $Ca_4Ti_3O_{10}$ was reported to be the equilibrium product of the composition $4CaO \cdot 3TiO_2$, at least at 1650°C [173]. This may explain why they are not determined in the present study. Another possibility is that even longer sintering duration might be needed for the formation of $Ca_3Ti_2O_7$ and $Ca_4Ti_3O_{10}$. The details have not been investigated further.

Preliminary results show that in region V, the additional phase $CaCu_2O_3$ is also observed besides the three phases of ($CaTiO_3$+Ca_2CuO_3+CuO). Fig. 4.13 shows the XRD patterns of some representative composites (A, B, C, D) in phase region V (marked in Fig. 4.12), which are located along the bi-phasic line of (CuO-Ca_2CuO_3). As seen from Fig. 4.13, with CuO content in the sample (from "A" to "D") increasing, both Ca_2CuO_3 and $CaCu_2O_3$ are decreasing. The predominant phase is changing from Ca_2CuO_3 to CuO when the CuO content increases ("A" to "D"). The $CaCu_2O_3$ phase clearly exists in the samples with high Ca_2CuO_3 content samples ("A", "B" and "C"). In addition, with more Ca_2CuO_3 content ("A"), higher amount of $CaCu_2O_3$ is observed. The phase equilibria at different oxygen pressure in the system CaO-CuO showed that Ca_2CuO_3 was the only intermediate phase [59]. The compound $CaCu_2O_3$ was reported to be stable above 950°C [174]. Roth et al reported $CaCu_2O_3$ was stable between 985° and 1018°C [61]. In our study, a possible partial reaction between Ca_2CuO_3 and CuO might happen during the long term sintering, and therefore produce a certain amount of $CaCu_2O_3$ [175]. More detailed work is required to clarify these points.

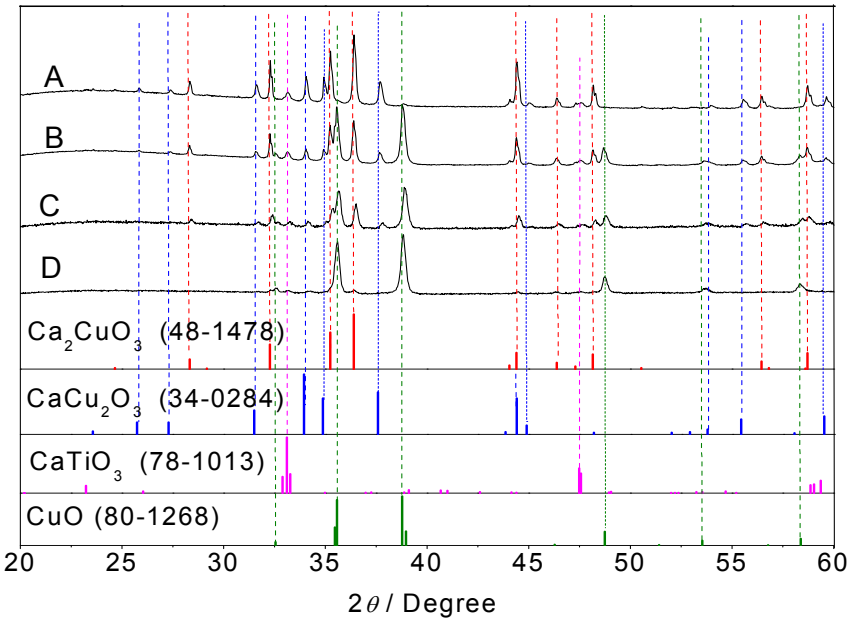

Fig. 4.13 The XRD patterns for the representative samples (A) to (D) in phase region V, which are marked in Fig. 4.12, with starting compositions of CuO : TiO_2 : CaO = 44.5 : 2.0 : 53.5; 62.0 : 1.8 : 36.2; 67.1 : 1.7 : 31.2; 84.3 : 1.5 : 14.2. Additional phase of $CaCu_2O_3$ (indicated by blue color) is clearly observed in the samples with higher Ca_2CuO_3 content.

4.3 Dielectric property in ternary system CuO-TiO_2-CaO

4.3.1 Dielectric property mapping

The room-temperature dielectric constant ε_r and dielectric loss tan δ at 10 kHz in the ternary system CuO-TiO_2-CaO sintered at 950°C are shown in Fig. 4.14. The phase boundaries determined in Section 4.2 are marked as dashed lines in Fig. 4.14. Most composites in the CuO-rich region and along binary CuO-CaO line exhibit quite promisingly high ε_r (>10^4) (Fig. 4.14 (a)). The ε_r of composites in tri-phasic regions of II and III, both of which contains TiO_2, give relatively low values. Compared to other phase regions, quite high values for tan δ in the composites in phase region V are observed (Fig. 4.14 (b)).

Sarkar et al. reported that properly annealed CuO possesses giant ε_r [97]. They proposed that using their route small portions of Cu^{3+} located at grain boundaries was responsible to the giant dielectric response. An electrically heterogeneous microstructure containing semiconducting grains and insulating grain boundaries was proposed [176]. This is the desired electrical microstructure to produce the internal barrier layer effect, which is thought to be the most probable mechanism for giant dielectric constants [137, 177]. In this study, the particular microstructure of larger grains (≈ 3 μm) of a predominant phase surrounded by smaller grains (≈ 0.3 μm) of secondary phases are observed in the composites in the CuO-rich region and along CaO-CuO binary line. This microstructure seems to be important to explain the observed dielectric behaviour, which will be discussed in Section 4.3.2. Such types of microstructures probably follow the internal barrier layer capacitance effect [118, 178] to enhance the dielectric properties of the composites.

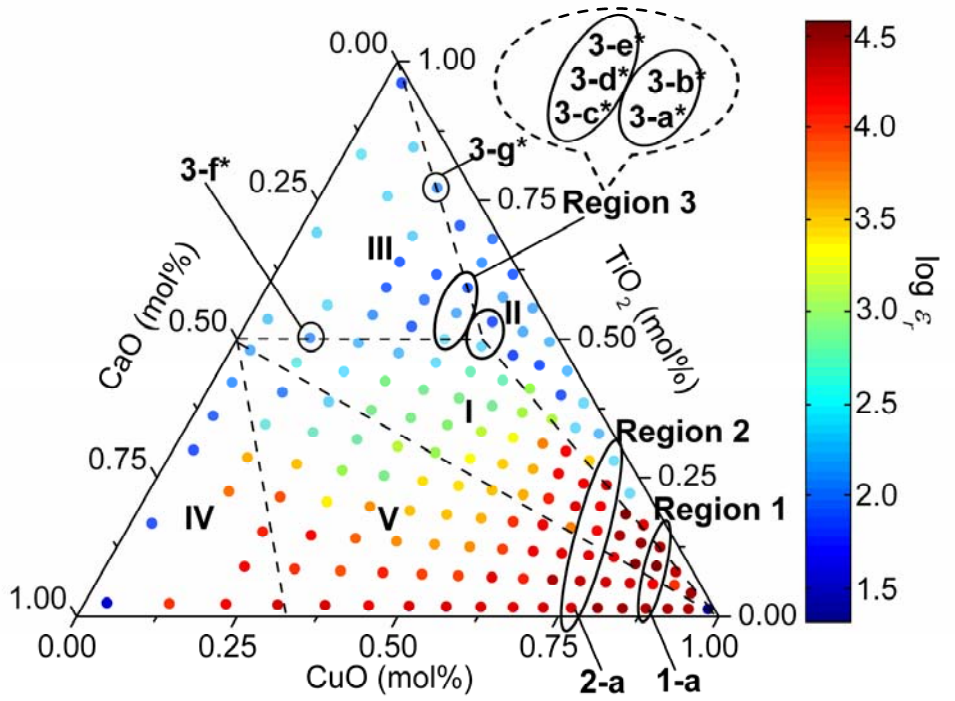

(a)

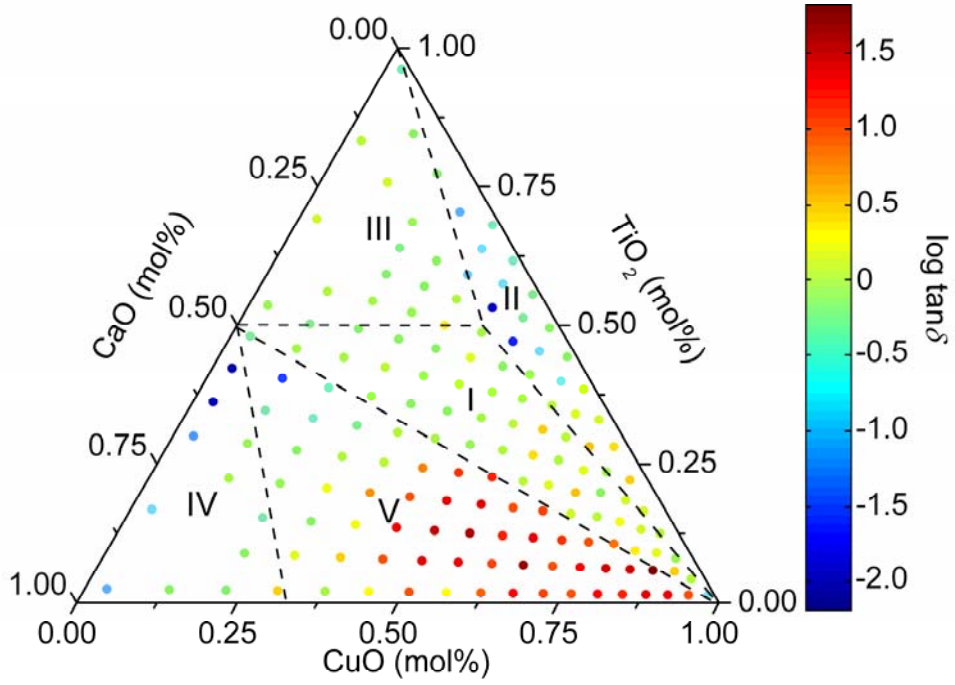

(b)

Fig. 4.14 Room-temperature of (a) ε_r and (b) tan δ of the samples sintered at 950°C in ternary system CuO-TiO_2-CaO at 10 kHz. Colored dots represent the investigated compositions (molar fraction) used to determine dielectric properties and the phase relations in Fig. 4.12. Dashed lines show the phase boundaries. The dielectric behaviour in the representative composites marked in Region 1 and Region 2 (Region 3) is discussed in Section 4.3.2 (Section 4.3.3).

Compared to the high dielectric constant of the composites in the CuO-rich region, the composites near $CaCu_3Ti_4O_{12}$ show much lower ε_r (~200) when they were sintered at 950°C (Fig. 4.14 (a)). However, the material with $CaCu_3Ti_4O_{12}$ phase was reported to show quite promising dielectric response ($\varepsilon_r > 10^4$) over a large frequency and temperature range [84]. Hence, different sintering conditions were performed in the composites in $CaCu_3Ti_4O_{12}$-rich region. When the composites near $CaCu_3Ti_4O_{12}$ region were sintered at 1050°C in air, quite high dielectric constants comparable to the reported values are observed. Great differences in microstructure are also observed compared to those sintered at 950°C. The detailed data will be discussed in Section 4.3.3.

4.3.2 Dielectric property in CuO-rich region

In order to show the correlation between dielectric property and phase distribution in the CuO-rich region in the ternary system CuO-TiO_2-CaO, composites in region 1 and region 2 (marked in Fig. 4.14 (a)) across the three different tri-phasic regions of V, I, II are chosen to demonstrate the frequency dependence of dielectric property in detail. Fig. 4.15 shows the frequency dependence of dielectric constant and dielectric loss of the representative samples (1-a) to (1-d) in region 1 and samples (2-a) to (2-g) in region 2 (Fig. 4.14 (a)). A clear difference of the dielectric behaviour across different phase regions is observed. This is likely to depend on various characteristics such as different multiphase combinations and/or microstructures.

In phase region V, a relative plateau of ε_r (>10^4) is observed, as seen in samples (1-a), (1-b) (Fig. 4.15 (a)) and samples (2-a), (2-b), (2-c) (Fig. 4.15 (b)) over the measured frequency range from 10^2 Hz to10^6 Hz. In comparison, in phase region I, as seen in samples (1-c), (1-d) (Fig. 4.15 (a)) and samples (2-d), (2-e), (2-f) (Fig. 4.15 (b)), the dielectric constant values slightly decrease with frequency increasing in low frequency range. In the higher frequency range, sharp decrease of dielectric constants with frequency increasing is observed.

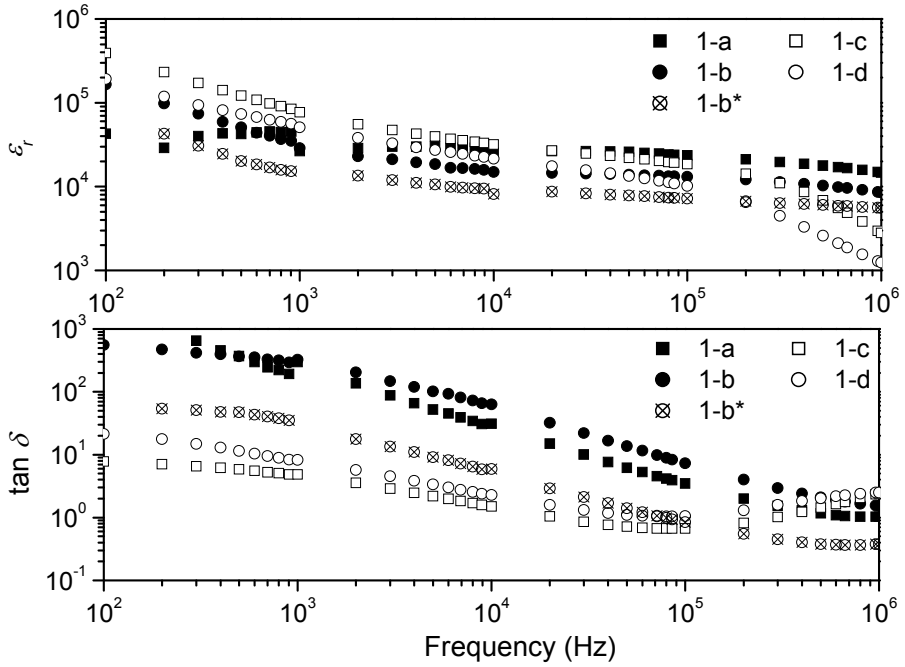

(a)

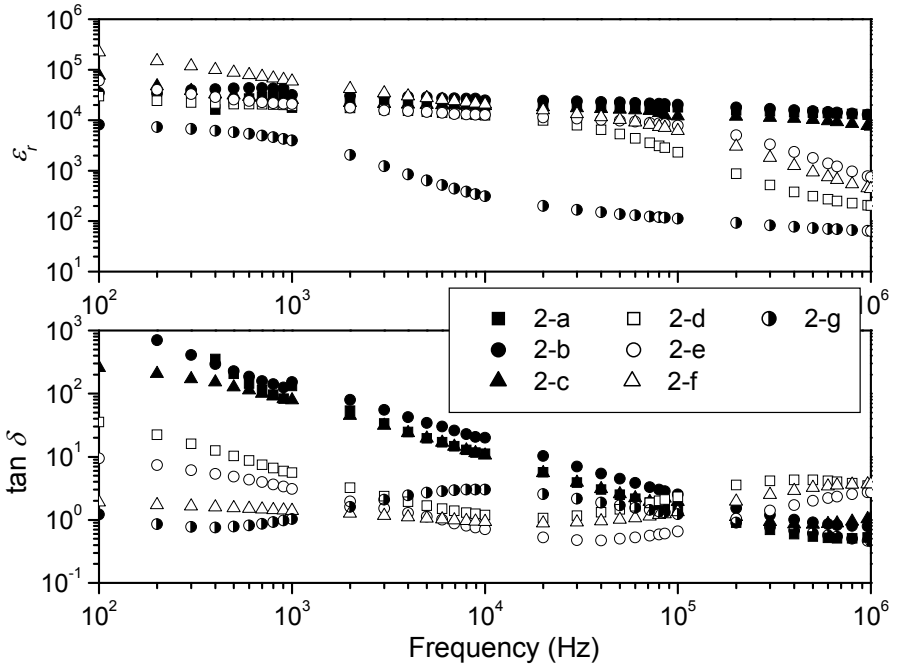

(b)

Fig. 4.15 The frequency dependence of ε_r (up) and tan δ (down) of (a): samples (1-a) to (1-d) (down to up) of Region 1 and (b): samples (2-a) to (2-g) (down to up) of Region 2 in Fig. 4.14 (a). Sample (1-b*) has the same starting composition as sample (1-b), but sintered at 1000°C, whereas others were sintered at 950°C.

In the high frequency range, the drastic drop of ε_r accompanied with a "loss peak" can be well described by a Debye-like relaxation [141]. The steep decrease in ε_r happens at the frequency where tan δ displays a relaxation peak. A change of physical nature of dielectric response can be revealed. It corresponds to the dielectric contribution changing from grain boundary at low frequency range to grain at high frequency range. The relaxation peak occurs at 50 kHz for samples (2-d) to (2-f) (Fig. 4.15 (b)), whereas it is found at around 100 kHz for samples (1-c) and (1-d) (Fig. 4.15 (a)). When the TiO_2 phase exists in the composite, which is the case in phase region II, the drastic drop of ε_r behind 1 kHz accompanied with a broad loss peak is observed in sample (2-g) (Fig. 4.15 (b)).

The plot of tan δ versus the frequency shows the possible coexistence of the two mechanisms. At lower frequency, the conduction mechanism might be the main contribution to the dielectric loss. At higher frequency, the relaxation phenomenon is the main source of the dielectric loss. The relaxation peak shifts to lower frequencies with decreasing of Cu content.

For the samples (1-a), (1-b) (Fig. 4.15 (a)) and (2-a), (2-b), (2-c) (Fig. 4.15 (b)), extremely high tan δ values are measured, especially at low frequency range. Such dielectric behaviour is also observed in other composites along CaO-CuO binary line. This implies a serious limitation to the application of such materials [179]. The dc conductivity is possibly the main contribution to the high dielectric losses in such composites in phase region V.

The dielectric loss of ceramic materials is also influenced by the extrinsic loss arising from porosity, secondary phases, grain size and defects, etc. induced by processing [180-181]. For example, when higher sintering temperature (1000°C instead of 950°C) is applied in the same composition as sample (1-b), a large decrease of tan δ and a slight decrease of ε_r are observed (sample (1-b*) in Fig. 4.15 (a)). This might be caused by the densification of the sample and by the decrease of porosity after sintering at higher temperature [182]. Fig. 4.16 shows the microstructure of these two samples. A bimodal grain size distribution is observed. The bigger grains are found to be composed of only copper oxide by EDX analysis. The smaller grains with secondary phases are situated on the bigger copper oxide grains. Compared to (1-b), sample (1-b*) shows the growing of both types of grains. The porosity of the sample (1-b*) treated at 1000°C is much lower than (1-b) at 950°C (Fig. 4.16). These preliminary results show that a decrease of the dielectric loss by sintering at higher temperature may be triggered.

Due to the limitation of the liquidus temperature, the sintering temperature is kept below 1000°C. Therefore, further optimization of the process in view of the decrease of tan δ may be probably studied by "soft chemistry" method, in which the temperature for sintering would be much lower compared to solid state reaction [183].

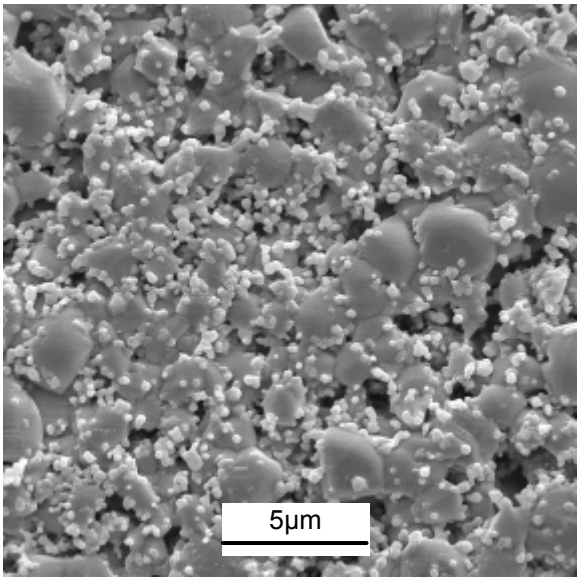

(a)

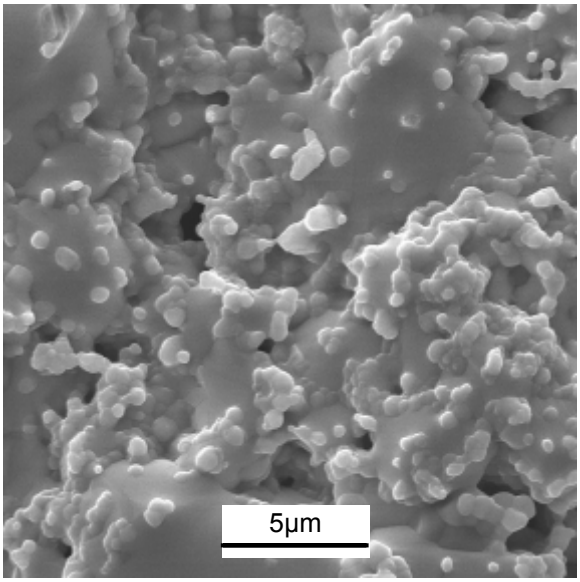

(b)

Fig. 4.16 SEM images of (a): sample (1-b) and (b): sample (1-b*) in Fig. 4.15 with the same starting compositions at sintering temperature of 950°C and 1000°C, respectively.

The typical bimodal grain size distribution observed in sample (1-b), is also found in some of the other samples in CuO-rich region and along the CaO-CuO binary line. Fig. 4.17 shows the microstructure of the composites (1-a), (1-c), (1-d) (left images of Fig. 4.17) and the composites (2-a), (2-c), (2-f) (right images of Fig. 4.17). The bigger grains of the predominant phase (CuO) are found in a fine-grained matrix of secondary phases in the composites in phase region V and phase region I. When $CaTiO_3$ phase exists as the secondary phase in the composites (phase region V and I), the bimodal grain size distribution is apparent. When no $CaTiO_3$ phase is included in the composite (phase region II), in the samples (2-f) (Fig. 4.17) and (2-g) (not shown), the bimodal particle size distribution is not obvious any more. Correspondingly, the composites with clear bimodal grain size distribution exhibit quite high dielectric constants, which are independent on frequency below the Debye-like relaxation peak. The relaxation peak shifts to lower frequency when the phase compositions changing from phase region V to I to II. Meanwhile, the bimodal grain size distribution becomes less apparent with compositions changing from region V to I to II. Therefore, it can be revealed that the dielectric behaviour observed in high-ε_r materials is greatly influenced by the particular microstructure, especially when bimodal grain size distribution occurs in the composites. The grain boundary effect has been reported to have important influence on the dielectric behaviour [184]. In this work, the grain boundary effect between the bigger grains with the predominant phase and the smaller grains with the secondary phases might also play an important role for the observed high dielectric constants.

The above investigations lead to the following questions: why do the composites in these regions, especially when bimodal grain size distribution occurs in the microstructure, tend to have much larger dielectric constants? Do all the large dielectric constants result from a common mechanism? The detailed analysis concerning the possible mechanism for the giant dielectric constant response will be discussed in the Section 4.4.

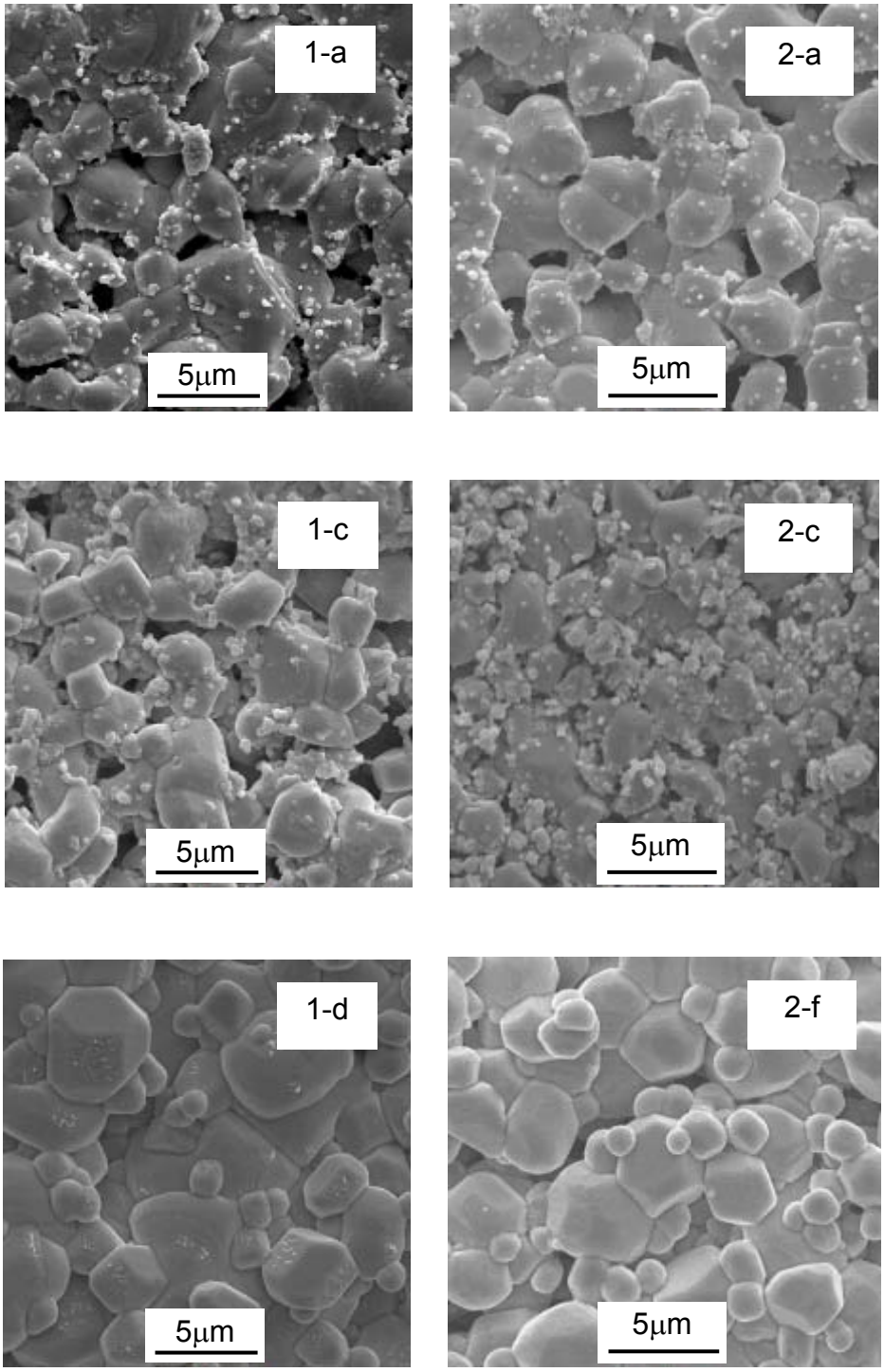

Fig. 4.17 SEM images of samples (1-a), (1-c), (1-d) (left-side images) and samples (2-a), (2-c), (2-f) (right-side images) in region 1 and region 2 of Fig. 4.14, respectively. Clear bimodal grain size distribution is shown in the composites.

4.3.3 Dielectric property in $CaCu_3Ti_4O_{12}$-rich region

Considerable interest to $CaCu_3Ti_4O_{12}$ has been stimulated since $CaCu_3Ti_4O_{12}$ was observed to show giant ε_r by Subramanian [84]. Furthermore, $CaCu_3Ti_4O_{12}$ has been reported to have quite different values of the dielectric constant because of different microstructures in the ceramic samples [185]. Fang et al. observed that ε_r of $CaCu_3Ti_4O_{12}$ becomes higher than 10^4 only when there are large grains (10-20 μm) in the sintered ceramic samples [185]. Adams et al. achieved $\varepsilon_r > 2.5\times10^5$ in large-grain (≈ 100μm) $CaCu_3Ti_4O_{12}$ ceramics, which is 2 orders of magnitude higher than fine-grained (≈ 5 μm) $CaCu_3Ti_4O_{12}$ ceramic [137]. They argued that large grains may be crucial for enhancement of the dielectric constant. Liu et al. found that $CaCu_3Ti_4O_{12}$ exhibits $\varepsilon_r \approx 10^4$ with small grain sizes (2-3 μm) [186]. They believe that the density of the sample is the key factor for the large dielectric constant in their samples prepared by a sol-gel process [186].

Due to a possible liquidus temperature in CuO-rich region, the samples near CuO cannot be treated higher than 1000°C; some of them partially melted even below 1000°C. Herein, 950°C is chosen as the sintering temperature for the dielectric property mapping in ternary system CuO-TiO_2-CaO. The composites in $CaCu_3Ti_4O_{12}$-rich region sintered at 950°C exhibit $\varepsilon_r \approx$ 200 at 10 kHz, seen in Fig. 4.14(a). When the composites in $CaCu_3Ti_4O_{12}$-rich region are sintered at 1050°C, quite different dielectric behaviour is observed. The following discussions are based on the comparison of the dielectric behaviour and microstructure of the representative composites marked in Region 3 in Figure 4.14 (a).

Fig. 4.18 presents the frequency dependence of the dielectric constant and loss tangent at room temperature for the $CaCu_3Ti_4O_{12}$-richest composites (3-a) and (3-a*), both of which have the same starting composition but sintered at 1050°C and 950°C, respectively. The location of (3-a*) in the ternary system is marked in Fig. 4.14 (a). Comparing to sample (3-a*), much higher ε_r and lower $\tan\delta$ are observed in sample (3-a). Judging from X-ray diffraction analysis, sample (3-a) contains the major phase of $CaCu_3Ti_4O_{12}$ with minor secondary phases of $CaTiO_3$ and Cu_2O.

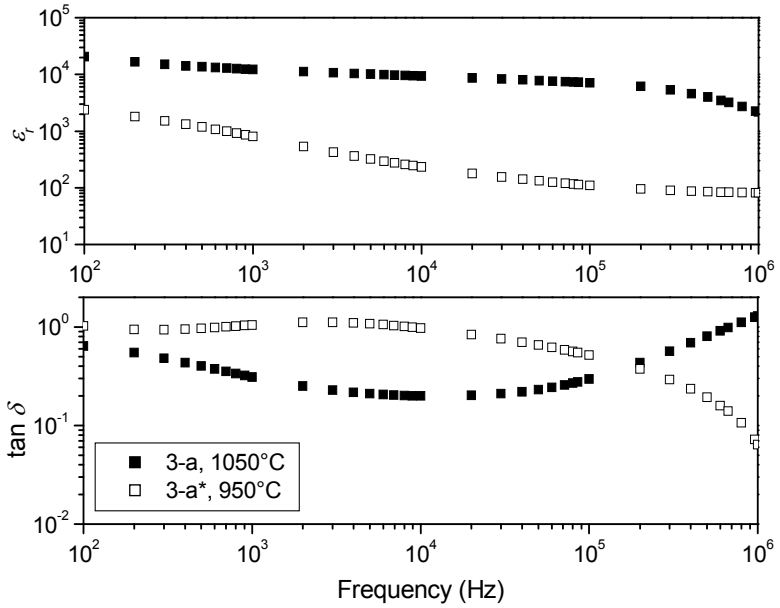

Fig. 4.18 The frequency dependence of ε_r (up) and tan δ (down) of samples (3-a) and (3-a*) in Region 3 of Fig. 4.14 (a) with the same starting composition but sintered at 1050°C and 950°C, respectively.

The microstructures of these two samples are investigated by SEM (Fig. 4.19). In sample (3-a*) (Fig. 4.19 (a)), the grains are homogeneous in shape and size, approximately ranging from 0.5 to 2 μm. In comparison, sample (3-a) sintered at 1050°C shows a quite different microstructure, as seen from Fig. 4.19 (b). Two types of grains are observed. There are the bigger grains with grain size approximately 10-30 μm and there are smaller grains with grain size ≈ 2 μm located at the triple point of the bigger grains or the grain boundaries. Additionally, a liquid phase is found on the grain boundaries. EDX analysis reveals different compositions in the big grains; small grains and liquid phase (see Fig. 4.20). $CaCu_3Ti_4O_{12}$, $CaTiO_3$ and copper oxide (either CuO or Cu_2O) have been thus localized, respectively. CuO will decompose into Cu_2O at temperature above 1000°C in air [138]. It may be assumed that copper oxide transforms into a liquid phase during the sintering treatment and leads to anomalous grain growth [187-188]. The existence of $CaTiO_3$ and a copper oxide wetting layer might be considered as the barrier layers of the $CaCu_3Ti_4O_{12}$ grains, promoting the dielectric property of $CaCu_3Ti_4O_{12}$ [138].

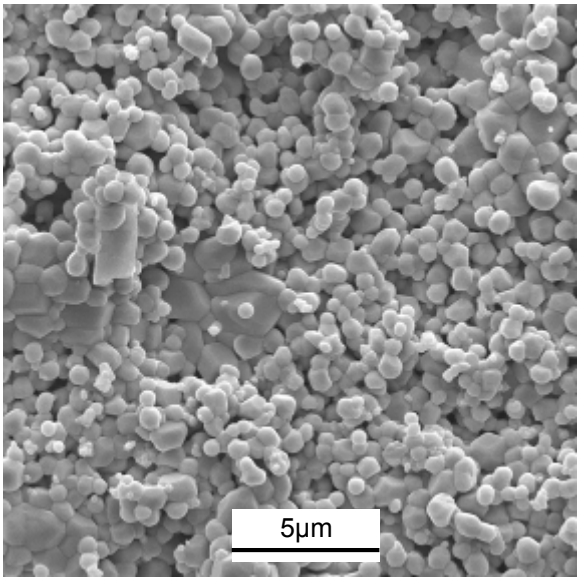

(a)

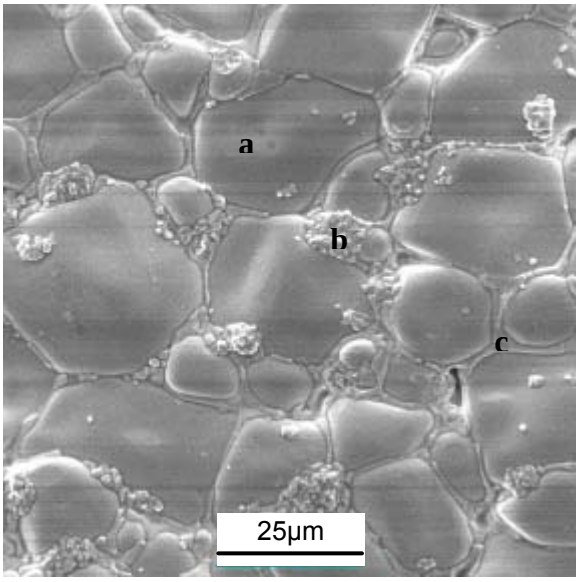

(b)

Fig. 4.19 SEM micrographs of (a): sample (3-a*) and (b): sample (3-a) in Fig. 4.18 sintered at 950°C and 1050°C, respectively. EDX composition analysis for a, b, c, marked in (b), is shown in Fig. 4.20. The grains are homogeneous in shape and size for sample (3-a*) sintered at 950°C. In comparison, clear grain boundary phases are observed in sample (3-a) sintered at 1050°C.

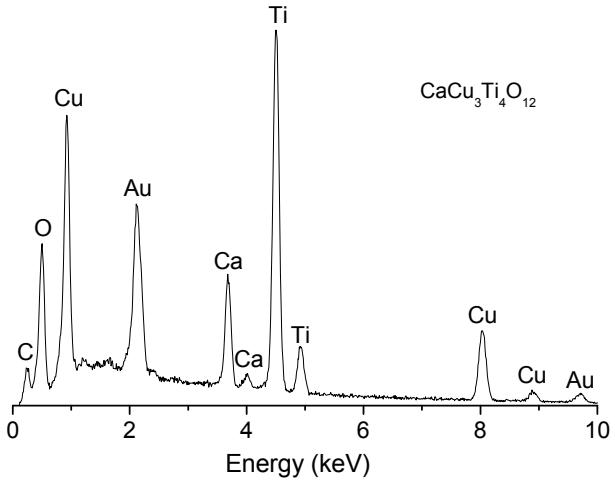

(a)

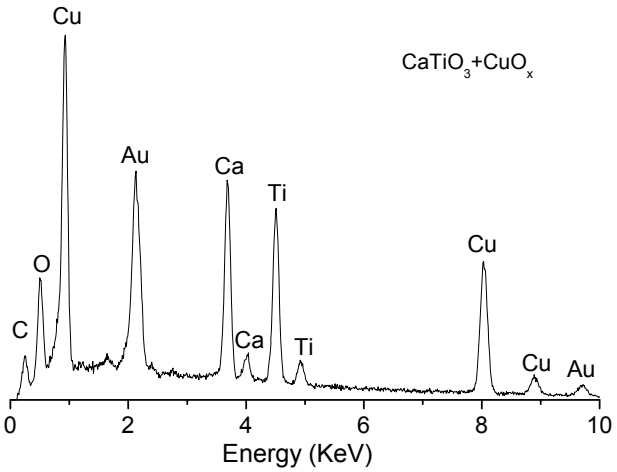

(b)

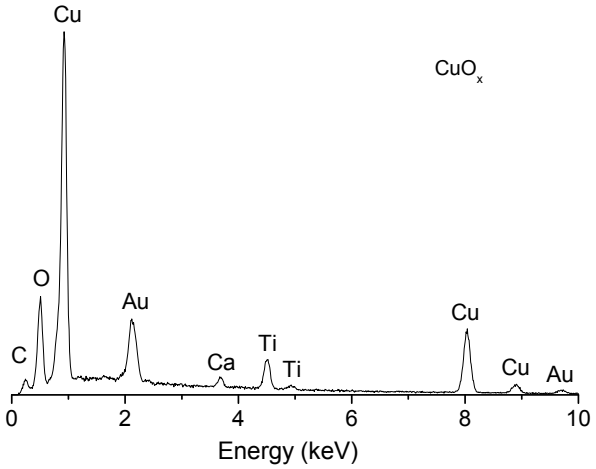

(c)

Fig. 4.20 The EDX composition analysis for (a) big grain, (b) small grains, and (c) liquid phase in sample (3-a) in Fig. 4.19. Different compositions for the big grains, small grains and liquid phase are revealed in sample (3-a).

From the above analysis, it can be seen that the particular microstructure with clear grain boundary effect is observed both in the composites in CuO-rich region (Section 4.3.2) sintered at 950°C and in sample (3-a) in $CaCu_3Ti_4O_{12}$-rich region sintered at 1050°C. The bigger grains with the predominant phase are found to be surrounded by the smaller grains or liquid phase with secondary phases. The particular microstructure which shows clear grain boundary effect might have important influence to the observed promising dielectric behaviour. The following discussions are based on the comparison of some other composites in $CaCu_3Ti_4O_{12}$-rich region in order to further justify the influence of grain boundary effect on the dielectric properties of the composites.

Fig. 4.21 shows the frequency dependence of sample (3-a) and (3-b) sintered at 1050°C. The location of these two samples is marked in Region 3 (Fig. 4.14 (a)). Lower dielectric constant values over the whole frequency range and higher dielectric loss values in the low frequency range are observed in sample (3-b) compared to (3-a). The dielectric constant of (3-b), even much lower than that of (3-a), but still keeps a quite high value above 1000 below 30 kHz. The XRD patterns of these two composites are shown in Fig. 4.22. Sample (3-a) contains the major phase of $CaCu_3Ti_4O_{12}$ with minor secondary phases of $CaTiO_3$ and Cu_2O. Sample (3-b) contains $CaCu_3Ti_4O_{12}$ and TiO_2 phase.

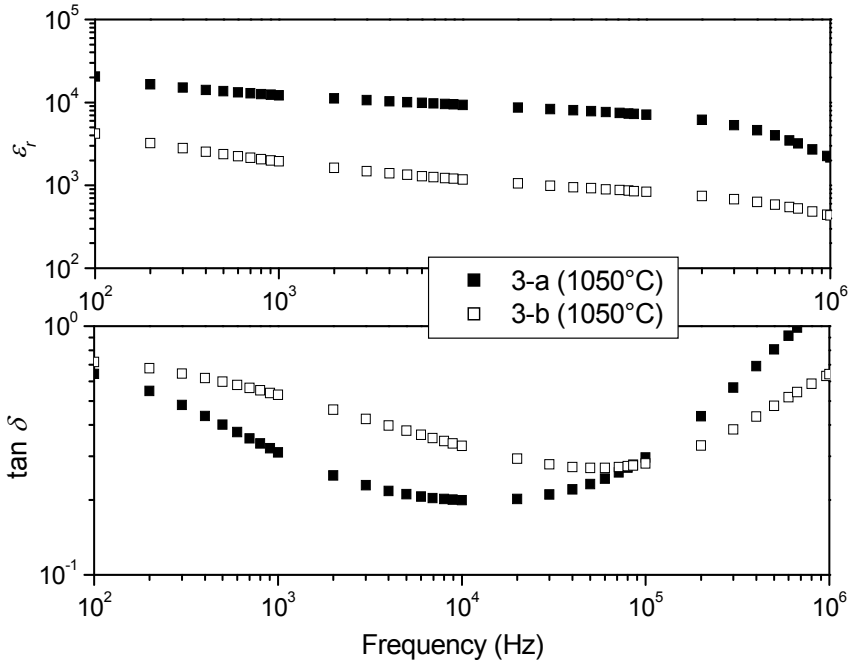

Fig. 4.21 The frequency dependence of ε_r (up) and tan δ (down) of samples (3-a) and (3-b) in Region 3 of Fig. 4.14 (a) sintered at 1050°C.

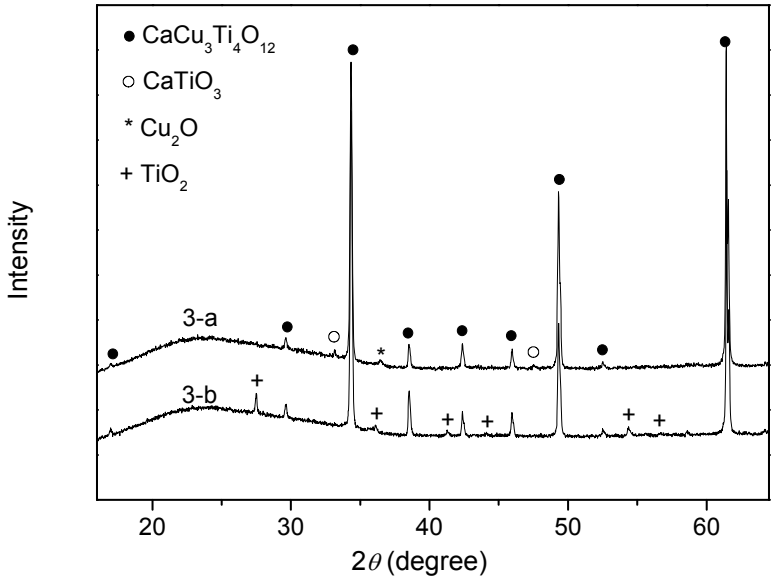

Fig. 4.22 XRD patterns of sample (3-a) and (3-b) in Region 3 of Fig. 4.14 (a) sintered at 1050°C. The phases included in (3-a) and (3-b) are ($CaCu_3Ti_4O_{12}$+$CaTiO_3$+CuO_2) and ($CaCu_3Ti_4O_{12}$+TiO_2), respectively.

The microstructure of sample (3-b) and (3-b*), which have same starting composition but sintered at 1050°C and 950°C, respectively, is shown in Fig. 4.23. Homogeneous grain size and shape in microstructure are observed in (3-b*), which is similar as observed in sample (3-a*), sintered at 950°C (Fig. 4.19 (a)). When the samples sintered at 1050°C, different microstructure is observed. The big grain growth also occurs in sample (3-b) when sintered at 1050°C. However, no clear grain boundary phases are observed in sample (3-b). As discussed previously, the microstructure in the sample (3-a) shows that both smaller grains with $CaTiO_3$ phase and a wetting layer composed of copper oxide are located surrounding the big $CaCu_3Ti_4O_{12}$ grains. Such grain boundary effect has important contribution to the observed high dielectric constant in sample (3-a) due to the possible barrier layers located at the grain boundaries. In comparison to (3-a), quite lower dielectric constant values (Fig. 4.21) are observed in sample (3-b) with no clear grain boundary phases. The dielectric constant of (3-b), even much lower than that of (3-a), but still keeps a quite high value above 1000 below 30 kHz. The enhancement of dielectric response in (3-b) compared to (3-b*) is mainly due to the densification due to higher sintering temperature. Hence, it can be seen that though the densification process can also enhance the dielectric response of the composites to some extent, no significant enhancement as occurred in (3-a) is observed in sample (3-b). This

further confirmed the important contribution of grain boundary phases to the giant dielectric response in sample (3-a).

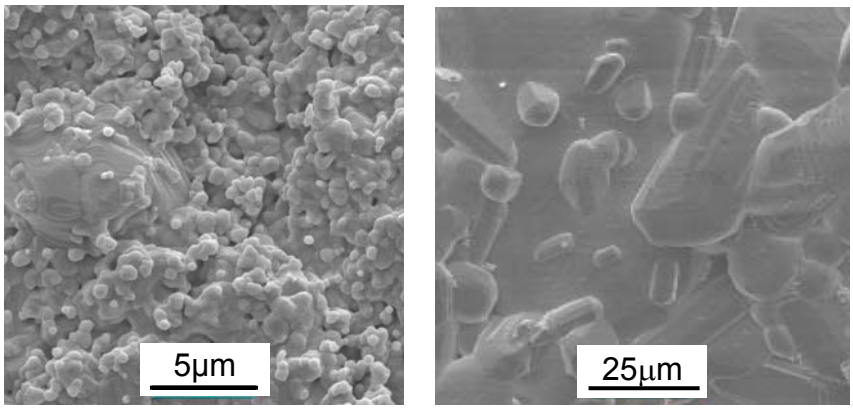

(a) (b)

Fig. 4.23 SEM micrographs of (a): sample (3-b*) and (b): sample (3-b) sintered at 950°C and 1050°C, respectively.

In order to compare the grain boundary effects in different compositions in $CaCu_3Ti_4O_{12}$-rich region, the frequency dependences of the three $CaCu_3Ti_4O_{12}$-rich composites (3-c), (3-d) and (3-e) in Region 3 (Fig. 4.14 (a)) have been investigated and are shown in Fig. 4.24. These composites exhibits very high ε_r (near 10^4 at the lower frequency range) with low dielectric loss when sintered at 1050°C, in comparison to those sintered at 950°C (ε_r ~200 at 10 kHz, seen in Fig. 4.14 (a)). The weak dependence of ε_r on frequency is observed in these composites sintered at 1050°C. The corresponding X-ray diffraction patterns for these samples sintered at 1050°C are shown in Fig. 4.25. Samples (3-c) and (3-e) are bi-phasic composites of ($CaCu_3Ti_4O_{12}$ + $CaTiO_3$) and ($CaCu_3Ti_4O_{12}$ + TiO_2), respectively. Sample (3-d) is a tri-phasic composite of ($CaCu_3Ti_4O_{12}$ + $CaTiO_3$ + TiO_2). The microstructure of these three samples is shown in Fig. 4.26. All three composites show clear grain boundary effect. Smaller grains located at the grain boundary of the bigger grains. This reveals the significance of grain boundary effect to the observed giant dielectric constants in such composites. Sample (3-d) shows particularly more evenly distributed smaller grains and bigger grains (Fig. 4.26). The nearly frequency independence of dielectric constants is observed in (3-d) (Fig. 4.24). Microstructure evolution and different phase combination in such composites are important for enhancing the dielectric properties. Although the clear grain boundary effect can be

concluded in this investigation, the influence of phase compositions and microstructure on the dielectric properties such as dielectric loss behaviour in such region is still a mystery, and needs more systematic investigations.

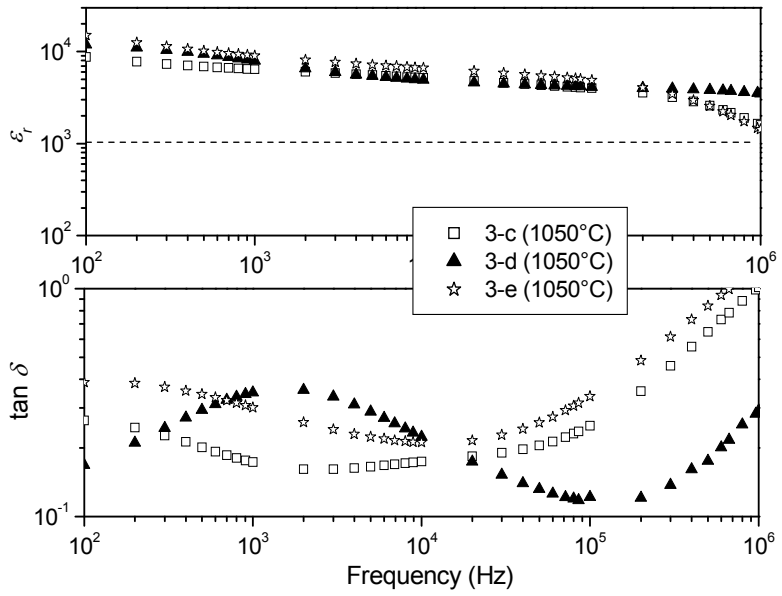

Fig. 4.24 The frequency dependence of ε_r (up) and tan δ (down) of samples (3-c), (3-d) and (3-e) in Region 3 of Fig. 4.14 (a) sintered at 1050°C.

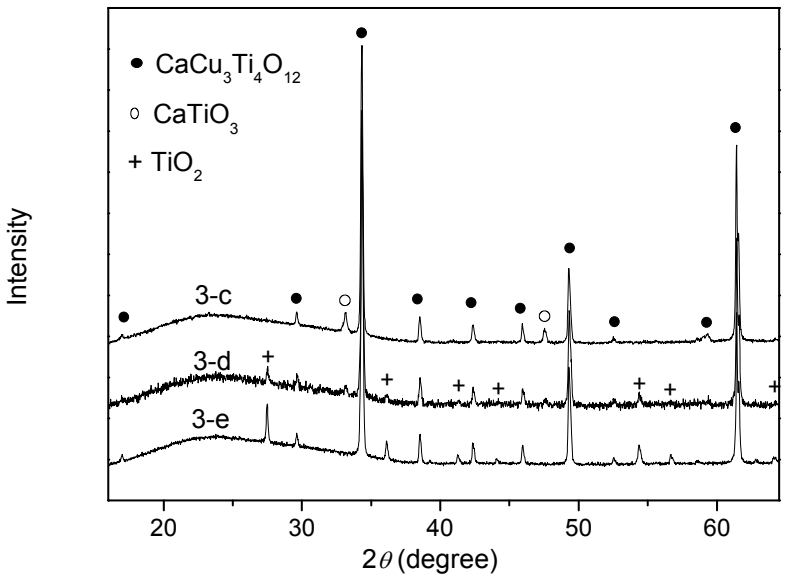

Fig. 4.25 X-ray diffraction patterns of sample (3-c), (3-d) and (3-e) in Fig. 4.24. The phases included in (3-c), (3-d) and (3-e) are ($CaCu_3Ti_4O_{12}$+$CaTiO_3$), ($CaCu_3Ti_4O_{12}$+$CaTiO_3$+TiO_2) and ($CaCu_3Ti_4O_{12}$+TiO_2), respectively.

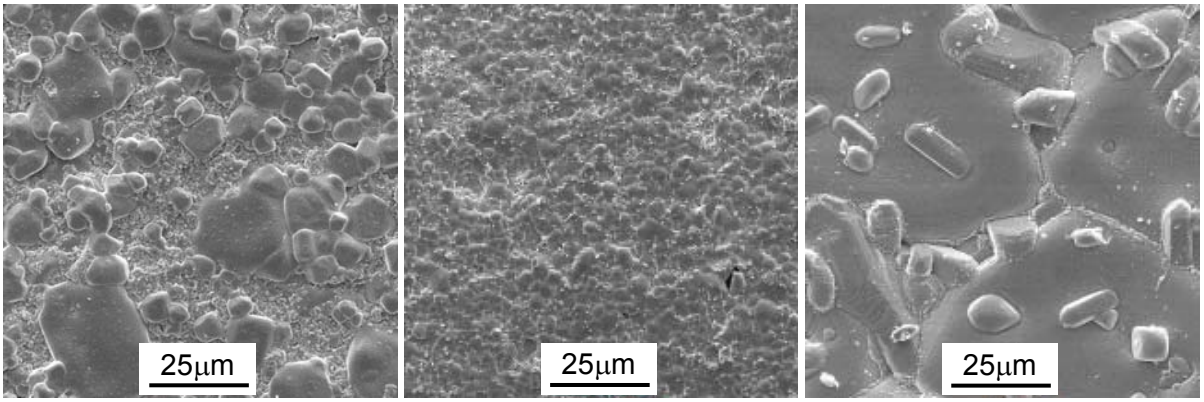

(a) (b) (c)

Fig. 4.26 SEM micrographs of (a): (3-c), (b): (3-d) and (c): (3-e) in Fig. 4.24. All three composites sintered at 1050°C show the grain boundary effect, which might significantly influence the dielectric behaviour of the composites.

Fig. 4.27 presents the dielectric constant and dielectric loss dependence on frequency at room temperature for bi-phasic ($CaCu_3Ti_4O_{12}$-$CaTiO_3$) composites of (3-c) and (3-f) (Fig. 4.14 (a)) with sintering temperature of 1050°C. A weak dependence of ε_r on frequency is observed in these samples. Much higher dielectric constants are observed in the $CaCu_3Ti_4O_{12}$-richer sample of (3-c). The composite (3-f) exhibits both lower dielectric constant and lower dielectric loss compared to (3-c).

Fig. 4.28 shows the microstructure of (3-f). The SEM image of (3-c) is shown in Fig. 4.26(a). Typical bimodal grain size distribution is observed in both samples. EDX analysis reveals different compositions in the bigger grains and smaller grains, which are found to be $CaCu_3Ti_4O_{12}$ and $CaTiO_3$, respectively. Comparing these two samples, it can be clearly seen that the smaller grains are dominant in sample (3-f) (Fig. 4.28) because $CaTiO_3$ is the major phase in sample (3-f). Contrary to (3-f), the bigger grains are predominant due to the higher content of $CaCu_3Ti_4O_{12}$ in (3-c). Kobayashi et al. [139] investigated the dielectric properties of two phase composites of $CaCu_3Ti_4O_{12}$ and $CaTiO_3$ and found $CaTiO_3$ could effectively decrease the dielectric loss of the composite. A high ε_r ($\approx$ 1800) with a low tan δ ($\leq$0.02) below 100 kHz was obtained at a $CaCu_3Ti_4O_{12}$: $CaTiO_3$ ratio of 2 : 1. A barrier layer of $CaTiO_3$ on the surface of the $CaCu_3Ti_4O_{12}$ grains was proposed to be the possible contribution

to the high dielectric performance [139]. Similar barrier layer effect from $CaTiO_3$ might take place in sample (3-c). In case of (3-f), the sample is mainly composed of the smaller grains with the predominant phase of $CaTiO_3$ and few bigger grains with $CaCu_3Ti_4O_{12}$ phase. Therefore, the smaller dielectric response in (3-f) is supposed to be contributed mainly from the smaller grains ($CaTiO_3$), where the extrinsic contribution from the grain boundary of $CaCu_3Ti_4O_{12}$ is less.

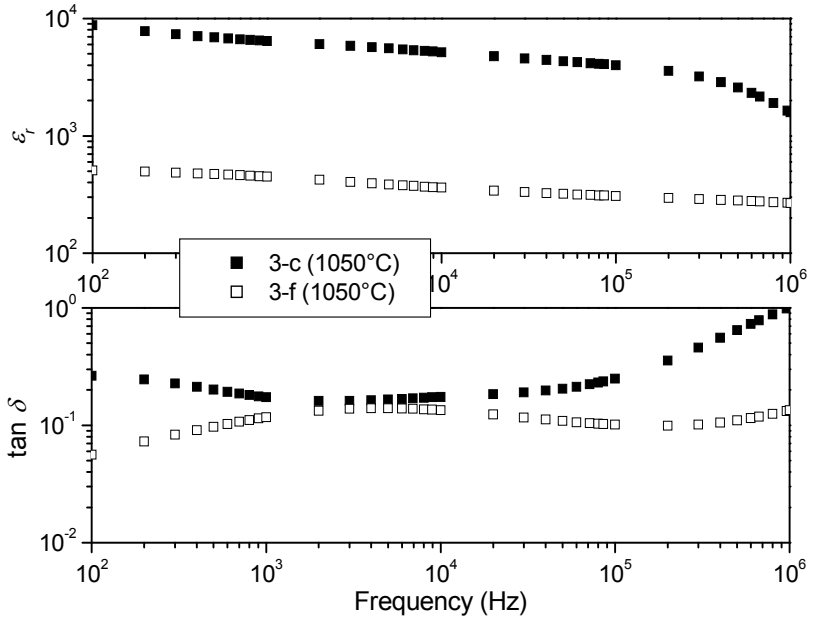

Fig. 4.27 The frequency dependence of ε_r (up) and tan δ (down) of samples (3-c) and (3-f) sintered at 1050°C, which are marked in Fig. 4.14 (a).

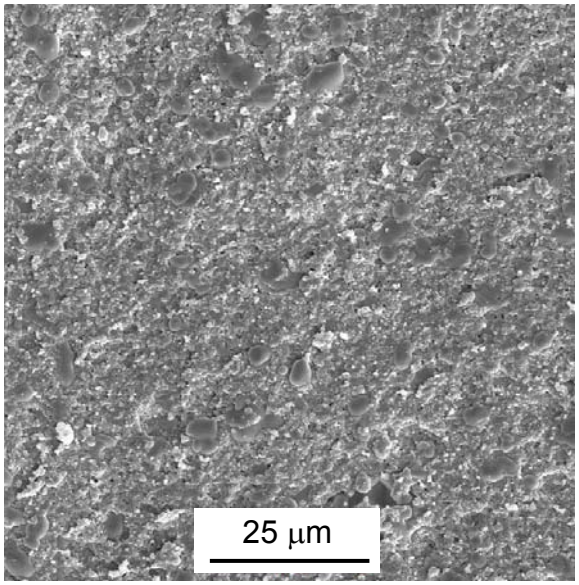

Fig. 4.28 SEM micrographs of sample (3-f) sintered at 1050°C.

Another comparison between two bi-phasic ($CaCu_3Ti_4O_{12}$-TiO_2) composites has been tentatively investigated, which also give the hint to the important role of the grain boundary effect to the dielectric response. Fig. 4.29 presents the dielectric constant and the dielectric loss dependence on frequency at room temperature for sample (3-e) and (3-g) sintered at 1050°C. A weak dependence of ε_r on frequency is observed in both samples. Higher dielectric constants are observed in the $CaCu_3Ti_4O_{12}$-richer composite. With the content of TiO_2 increasing, the dielectric constant value of the composite is decreasing, the dielectric loss decreasing as well. The microstructure of these two composites is shown in Fig. 4.26 (c) and Fig. 4.30, respectively. For (3-e), smaller particles located at the grain boundaries are observed and found to be a Cu-rich phase, although no additional copper oxide phase was examined in XRD pattern in this composite. Quite homogeneous grains in size and shape are observed in the composite (3-g). No clear boundary phase has been detected in (3-g). Lin et al. [189] investigated TiO_2-rich $CaCu_3Ti_4O_{12}$ systems and found that an increase in TiO_2 content decreases the dielectric constant of polycrystalline materials. In our study, similar results are obtained. It is further proposed that grain boundary phases of the composites have an influence on the dielectric behaviour of the composites.

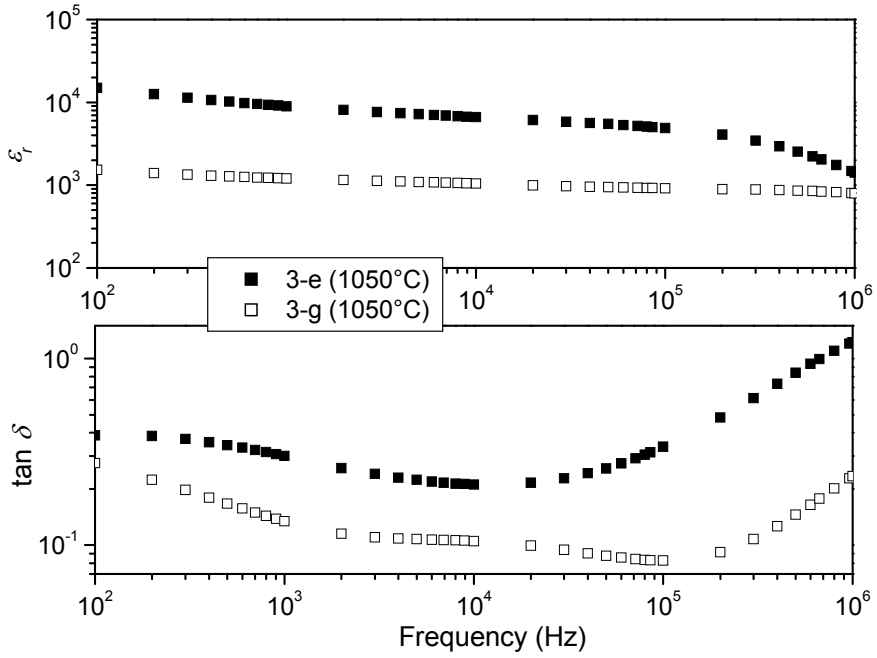

Fig. 4.29 The frequency dependence of ε_r (top) and tan δ (bottom) of composites (3-e), (3-g), sintered at 1050°C.

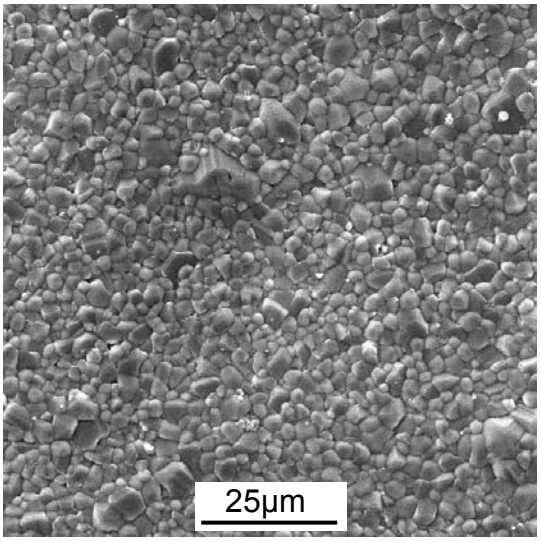

Fig. 4.30 SEM image of sample (3-g) sintered at 1050°C.

The results demonstrate the importance of ceramic microstructure in controlling the electric properties of composites and support the internal barrier layer effect at the grain boundaries. In summary, in the composites in $CaCu_3Ti_4O_{12}$-rich region, much higher dielectric constant can be obtained when sintered at 1050°C, in comparison to the composites sintered at 950°C. The densification process can enhance the dielectric response of the composites to some extent, but it is not the main reason for the observed significant enhancement of the dielectric response in the composites with clear grain boundary effect. Grain boundary effects are supposed to have important contributions to the observed high dielectric constant response.

4.4 Possible mechanism for the giant dielectric constant

4.4.1 Internal barrier layer capacitance (IBLC) mechanism

Back to the earlier mentioned questions, namely, why do the composites in CuO-rich regions sintered at 950°C and the composites in $CaCu_3Ti_4O_{12}$-rich region sintered at 1050°C tend to have much larger dielectric constants? Do all the large dielectric constants result from a common mechanism? In Section 2.4.3, the possible mechanism has been reviewed taking $CaCu_3Ti_4O_{12}$ as an example. Although the location of the barrier layer is still open to scientific debate and needs to be further confirmed, internal barrier layer effect was considered as the most favourable mechanism for $CaCu_3Ti_4O_{12}$ and the other materials such as Li or Ti doped NiO, CuO, which show similar dielectric behaviour [119]. Interfacial polarization occurs in electrically inhomogeneous systems. When an electric current passes through interfaces between two different dielectric media, because of their different conductivities, surface charges pile up at the interfaces, and give rise to a Debye-like relaxation process [141-142] under an external alternating voltage. A detected Debye-like relaxation response is not necessarily the result of dipole relaxation in the system; sometimes it originates from the heterogeneity of the system [143]. For example, grain boundaries and/or the electrodes applied to the sample can produce the effect [121]. This effect has been widely used to account for dielectric relaxations in many heterogeneous materials [103].

In previous investigations, clear grain boundary effects were observed in the composites in both CuO-rich region and $CaCu_3Ti_4O_{12}$-rich region, which exhibit giant dielectric constants. The bigger grains are found to be the major phase of the composite, and the smaller grains of secondary phases are located at the grain boundaries. Three microstructural models can be accordingly established and has been schematically illustrated in Fig. 4.31. In case of the composites in CuO-rich region, the smaller grains which surrounded the bigger grains may consist of one secondary phase (Fig. 4.31 (a)) or two secondary phases (Fig. 4.31 (b)). The third case is a model (Fig. 4.31 (c) & (d)) according to the microstructure which was observed in the composite (3-a) sintered at 1050°C in $CaCu_3Ti_4O_{12}$-rich region. There are two secondary phases in different forms located at the $CaCu_3Ti_4O_{12}$ grain boundaries. These are a liquidus phase of copper oxide and smaller grains of $CaTiO_3$ phase. In addition, according to the Fang et al.'s model [136], the barrier layers are located at domain boundaries inside the grain and grain boundaries (Fig. 4.31 (e)).

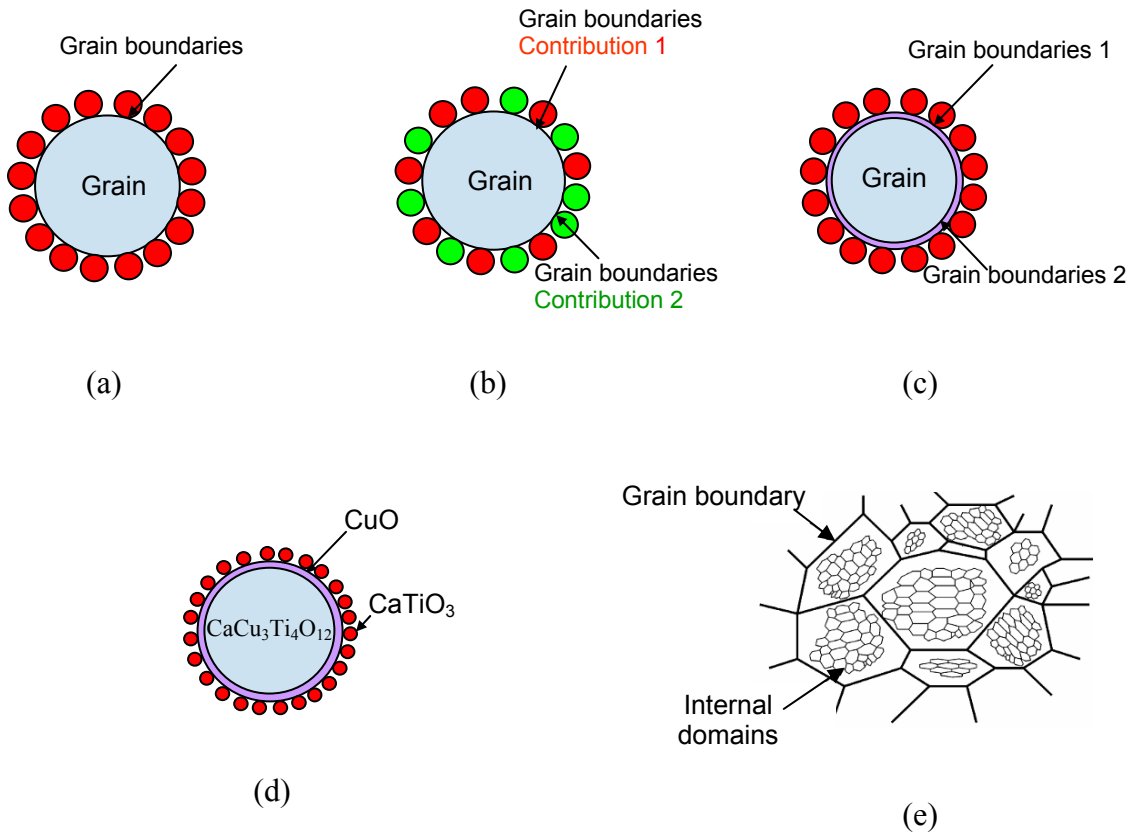

Fig. 4.31 Microstructure models of multiphased composites showing the grain boundary effect. The bigger grains with predominant phase are surrounded by (a) smaller grains with one secondary phase; (b) with two secondary phases; (c) smaller grains and liquid phase; (d) an example of model (c); (e) domain boundaries exist inside the grains [136].

The various morphologies associated with these possibilities for the location of the barrier layers can be related to the enormous enhancement of the dielectric constant and a Debye-like frequency response [190]. There are characteristic details of the dielectric response that may help to distinguish between them or exclude some of the possibilities, such as temperature dependence of dielectric responses [191] and/or impedance spectroscopy [137], I-V curve [140, 192], etc. Once the internal morphology responsible for the remarkable dielectric properties is established, a path to control over that morphology, allowing for fine tuning of the dielectric properties, might then become evident [113].

In the present work, the temperature dependence of the dielectric response has been investigated preliminarily on the representative composite (1-c) (Fig. 4.14 (a)) with

predominant phase CuO accompanied with secondary phases of $CaTiO_3$ and $CaCu_3Ti_4O_{12}$. This part is discussed in the next section.

4.4.2 Temperature dependence of dielectric response

Based on the dielectric property investigation from the ternary system CuO-TiO_2-CaO, the most promising candidates with high dielectric constants are observed in two regions. One is the CuO-rich region sintered at 950°C; the other is the $CaCu_3Ti_4O_{12}$-rich region sintered at 1050°C. The particular microstructure of bigger grains with predominant phase surrounded by smaller grains with secondary phases is observed. This type of microstructure is the desired electric microstructure to produce the internal barrier layer, which is thought to be the most probable mechanism for giant dielectric constants. Herein, in order to reveal the possible mechanism for the giant dielectric response, the detailed temperature dependence of dielectric response was carried out in the composite with the molar fraction of Cu/Ti/Ca of ~ 85/10/5, which is designated as sample (1-c) (Fig. 4.14 (a)). This composite shows giant dielectric constant above 10^4, with less frequency dependence below 10^5 Hz.

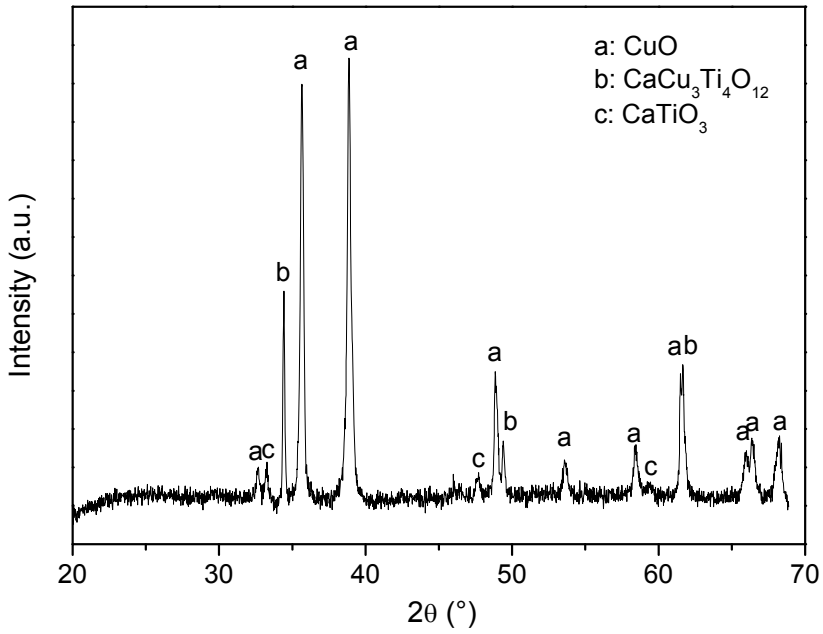

Fig. 4.32 XRD pattern of the sample (1-c) with the molar fraction of Cu/Ti/Ca of ~85/10/5, sintered at 950°C in air.

The microstructure of the sample (1-c) is shown in Fig. 4.17. The sample exhibits a bimodal grain size distribution, with small grains of about 300-600 nm and large grains of size comprised between 2 and 5 μm. The XRD pattern of the sample (1-c) is shown in Fig. 4.32. Three phases exist as $CaCu_3Ti_4O_{12}$, $CaTiO_3$ and CuO, in which CuO is the main phase.

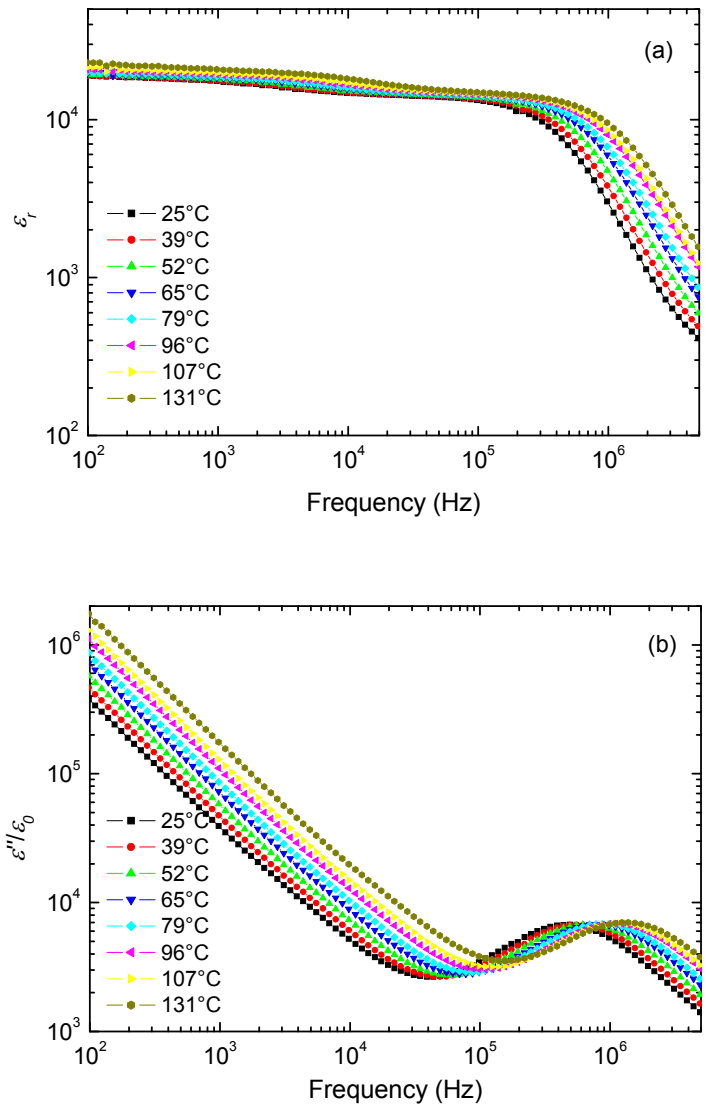

Fig. 4.33 The frequency dependence of the (a) ε_r and (b) $\varepsilon''/\varepsilon_0$ at temperatures between 25 and 130°C for sample (1-c) sinted at 950°C in air.

Fig. 4.33 shows the frequency dependence of the ε_r ($\varepsilon'/\varepsilon_0$) and $\varepsilon''/\varepsilon_0$ of the sintered sample at various temperature between 25 and 130°C. A Debye-like relaxation with a steep decrease in ε_r at the frequency where $\varepsilon''/\varepsilon_0$ displays a relaxation peak is observed. Fig. 3(a) shows that

sample (1-c) has very high dielectric constant $\varepsilon_r > 10^4$ and weakly frequency and temperature dependence below 100 kHz. The relaxation peak shifts to higher frequencies as temperature increases, shown in Fig. 4.33 (b), which reveals a thermally activated relaxation process [193].

The dielectric relaxation time, τ, (($\tau = 1/(2\pi f)$, where f is the response frequency at which the dielectric loss has a maximum)) can be determined by the Arrhenius law [194] of

$$\tau = \tau_0 \exp(\frac{Ea}{k_B T}) \quad \textbf{(4.1)}$$

$$\ln \tau = \ln \tau_0 + \frac{E_a}{k_B T} \quad \textbf{(4.2)}$$

where τ_0 is the pre-exponential factor, E_a is the activation energy for the relaxation, k_B is the Boltzmann constant and T is the absolute temperature. In Fig. 4.34, the relaxation time has been plotted as a function of inverse temperature. The experimental data fit well with the Arrhenius relation, within the temperature range of 25-130°C. The activation energy of an electrical response, at different temperature can be derived from the fitting curve (solid line) according to (Eq. 4.1 & Eq. 4.2) and is found to be 0.103 eV.

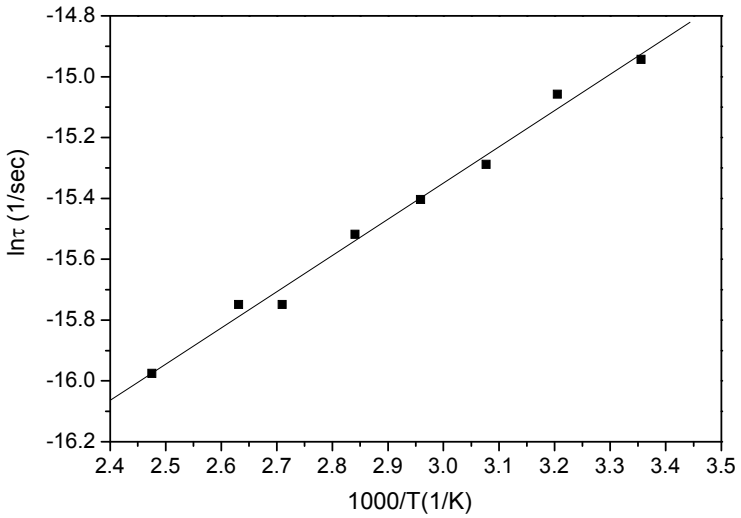

Fig. 4.34 Arrhenius plot of dielectric relaxation time τ for the sintered sample (1-c).

The secondary phases located at grain boundaries might provide a significant contribution to the observed high dielectric response of the sample (1-c). The charge carriers pile up at the

interfaces where different conductive materials exist, which exhibit high dielectric constant. The electrically heterogeneous microstruture consisting of semiconducting grains with insulating grain boundaries might associate to the high dielectric constant observed in (1-c) due to internal barrier layer effect [137]. As the permittivity of the sample (1-c) increases slightly with an increase of temperature over the whole frequency range, the thermally activated mechanism also plays its role partly in the high dielectric response of (1-c).

In the low frequency region, dielectric loss is quite high and increases with temperature, which is possibly due to the increase of the dc conductivity [195]. The expression describing the losses is:

$$\tan\delta = \frac{\varepsilon''}{\varepsilon'} = \frac{(\varepsilon_r'' + \sigma/\omega)}{\varepsilon'} \qquad \textbf{(4.3)}$$

where ε_r" corresponds to the part of the losses associated to the relaxation phenomena and σ/ω corresponds to the part due to a pure conduction mechanism, with σ the conductivity, ω the angular frequency [138]. Therefore, the plot of $\varepsilon''/\varepsilon_0$ versus the frequency for various temperatures gives a hint to the possible coexistence of these two mechanisms.

4.4.3 Temperature dependence of impedance spectra

In polycrystalline solids, complex impedance spectra usually contain features that can be directly related to the microstructure [196]. The resistance, *R* and *C* values of electrically active grain and grain boundary regions in many electroceramics can be estimated by impedance spectroscopy (IS) [197]. Data can often be modelled on an ideal equivalent circuit consisting of two parallel *RC* elements connected in series, one *RC* element for the bulk (grain) and the other for the grain boundary. For such a circuit, each *RC* element gives rise to (ideally) a semicircular arc in impedance complex plane plots and a plateau in spectroscopic plots of the real component of the permittivity (or capacitance). The position of the arcs in the frequency spectrum depends on their relaxation times, τ, where $\tau = RC$; at the arc maxima, the relationship $\omega_{max}RC=1$ holds, where $\omega=2\pi f$ and f is the applied frequency (in Hz). In general, τ for grain boundary regions is much larger than for the bulk and the grain boundary response is relaxed out at lower frequencies than bulk effects. Often, *RC* elements have ω_{max} values that lie outside the available frequency range, especially if they represent either insulating

regions with high R or semiconducting regions with low R. In such cases, only parts of arcs may be observed [91].

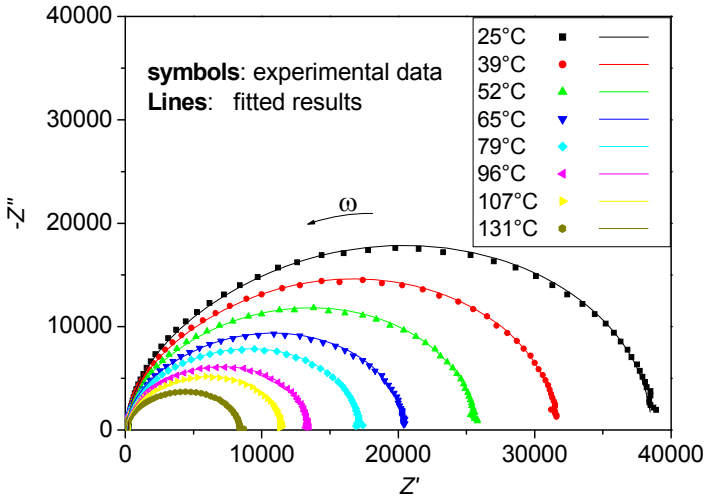

Fig. 4.35 Impedance complex plane plot, Z^* at different temperatures for the sintered sample (1-c). The fitting results consist of segments of three (RC) elements connected in series (Fig. 4.36).

Fig. 4.35 shows the impedance spectra of the sintered sample (1-c) at various temperatures. Apparently, only one arc is found in the complex plot. Due to the big difference of the resistivities between grain and grain boundary, the higher resistivity of the grain boundary is dominating the overall conductivity and thus leading to the appearance of only one semicircle in the complex impedance plots. Detailed curve fitting results are also shown in Fig. 4.35. The best fitting results consist of segments of three (RC) elements connected in series, as shown in Fig. 4.36. Resistivity, specific capacitance and dielectric permittivity values at various temperatures due to three (RC) elements are reported in Table 4.2. The R_1C_1 element gives quite low resistivity and small capacitance, in comparison to the other two elements of R_2C_2 and R_3C_3. The fitting results suggest the two possible barrier layers exists corresponding to elements R_2C_2 and R_3C_3, respectively, which give rise to giant dielectric constants.

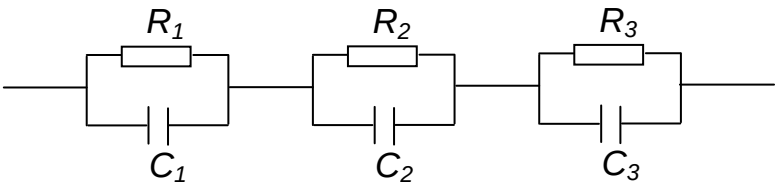

Fig. 4.36 Equivalent circuit used to represent the electrical properties in sample (1-c).

Table 4.2 Specific resistivity, capacitance and permittivity values for (R_1C_1), (R_2C_2) and (R_3C_3) at various temperatures determined by impedance spectroscopy in sample (1-c).

T /°C	R_1C_1			R_2C_2			R_3C_3		
	R /Ω	C /pF	ε_r	R /Ω	C /pF	ε_r	R /Ω	C /pF	ε_r
25	208	33.9	307	5611	4080	37000	32730	2510	22800
39	175	36.9	335	4784	4050	36800	26590	2530	23000
52	147	40.9	371	4109	3940	35700	21360	2610	23700
65	121	46.8	424	3438	3820	34700	16830	2710	24500
79	108	49.7	451	2851	3860	35000	14180	2720	24700
96	88	59.9	543	2189	3860	35100	11100	2760	25000
107	82	58.7	533	2000	3690	33500	9323	2900	26300
131	69	65.1	591	1572	3470	31500	6746	3130	28400

The resistivity data, R, obtained for R_1C_1, R_2C_2 and R_3C_3 can be plotted against reciprocal temperature in Arrhenius format (Fig. 4.37) according to (Eq. 4.4 & Eq. 4.5). The experimental data fit well with the Arrhenius relation, within the temperature range of 25-130°C. The activation energies $E_{a,1}$, $E_{a,2}$ and $E_{a,3}$, corresponding to (R_1C_1), (R_2C_2) and (R_3C_3) are 0.110, 0.128 and 0.154 eV, respectively. $E_{a,1}$ is very close to the activation energy obtained from the Debye-like relaxation time (Fig. 4.34).

$$R = R_0 \exp(\frac{E_a}{k_B T}) \quad \textbf{(4.4)}$$

$$\ln R = \ln R_0 + \frac{E_a}{k_B T} \quad \textbf{(4.5)}$$

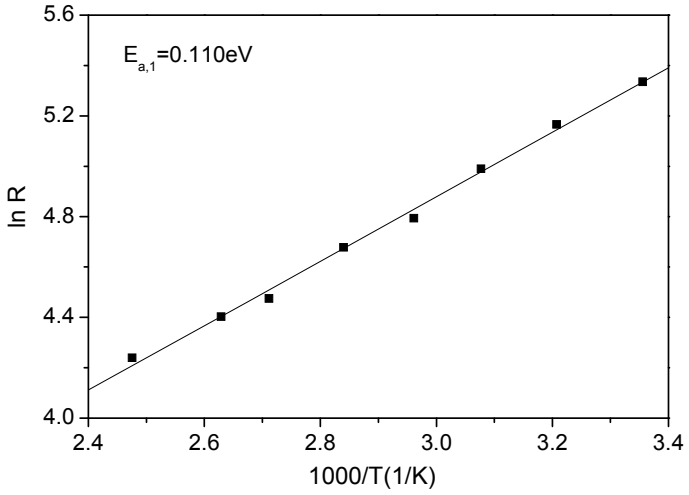

(a)

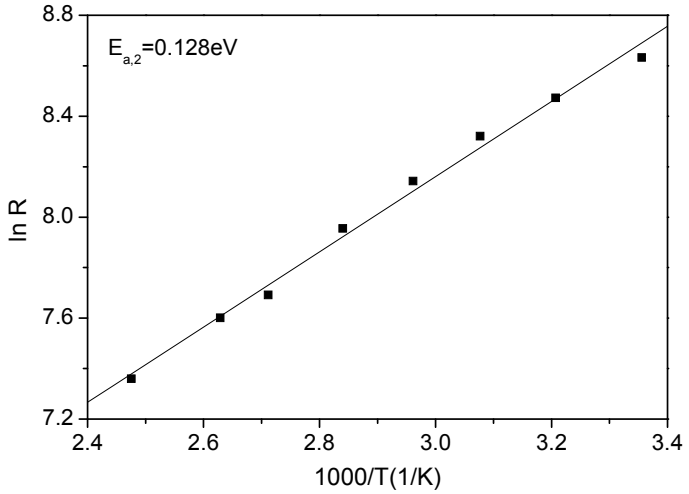

(b)

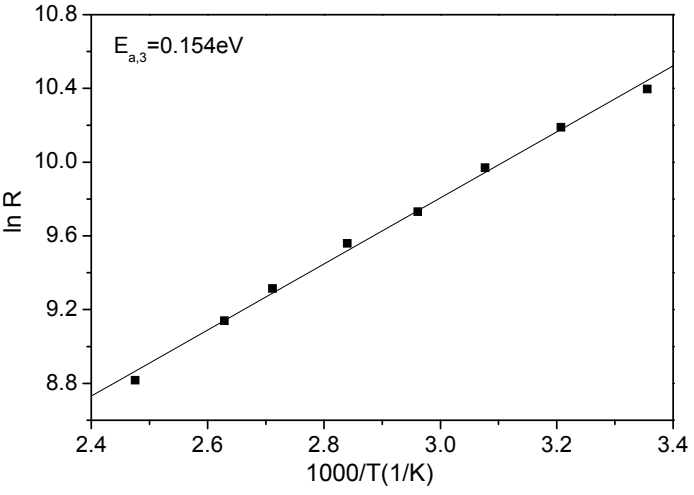

(c)

Fig. 4.37 Arrhenius plot of resistance R_1, R_2, R_3 obtained from impedance spectra in sample (1-c).

From the equivalent circuit of Maxwell-Wagner relaxation, it can be deduced that the activation energy of the bulk is approximately equal to that of the Debye-like relaxation [186]. Therefore, the three elements (R_1C_1), (R_2C_2) and (R_3C_3) can thus be attributed to bulk (grain), barrier layer one, barrier layer two, respectively. From the impedance spectra data, it can be concluded that the barrier layers can effectively enhance the dielectric response of the material. However, the location of the barrier layers is still uncertain. According to the schematic microstructure model (Fig. 4.31 (b), it is supposed that the barrier layers can be possibly locate at grain boundaries. Two secondary phases might act as the two estimated barrier layers correspondingly. Based on the model by Fang et al. (Fig. 4.31 (e)), the two barrier layers can be also attributed to the domain boundary and grain boundary, respectively. To determine the location of the barrier layers, more investigations have to be carried out.

If the enormous dielectric constants of such materials do in fact originate from the suggested extrinsic mechanism, the width of the barrier layers, and hence the value of the dielectric response, might be controllable [90]. Several types of experiments might be useful in testing the location of the barrier layers. Impedance spectroscopy at lower temperatures (below 0°C) can be applied to get separate semicircles, representing different elements, considering the fitting results are not convincing due to the possibility to estimate the impedance spectroscopy results based on other circuits. Temperature dependence of other samples with different secondary phases can be tested to exclude the barrier layers from different secondary phases. C-V measurements, TEM, etc., can also give strong indications about existence of the barrier layers. These proposals deserve to be further investigated.

4.5 Dielectric property of representative composites by sol-gel method

4.5.1 $CaCu_3Ti_4O_{12}$

$CaCu_3Ti_4O_{12}$ is usually made by standard solid-state reactions from stoichiometric ratios of $CaCO_3$, CuO, and TiO_2 at high temperatures. Higher temperature is required in the powder preparation process. Moreover, it suffers from the disadvantages of inhomogeneity. In contrast, synthesis from a solution affords the reaction with a homogeneous mixing of the metal ions at the atomic scale, shorter reaction time and at lower temperature [198].

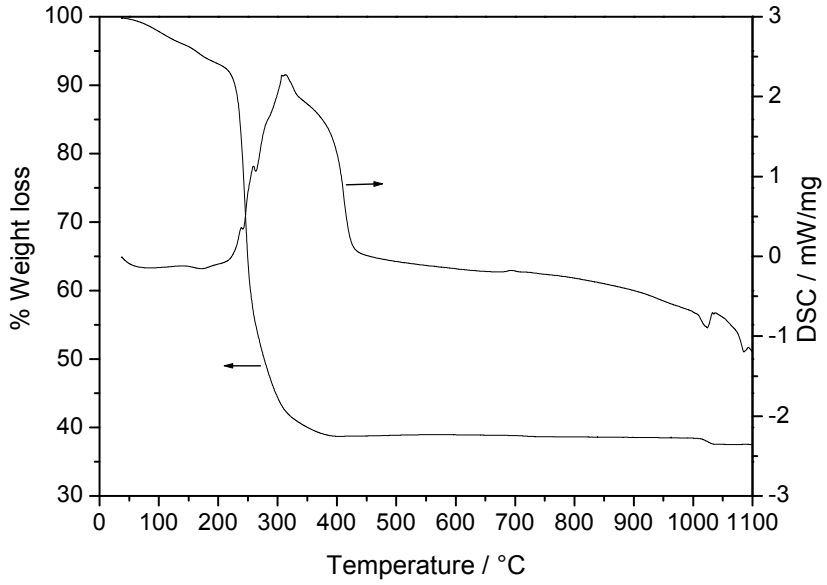

Fig. 4.38 The TG-DSC curves of the thermal decomposition of $CaCu_3Ti_4O_{12}$ precursor at a heating rate of 10°Cmin^{-1} in syn. air.

The TG-DSC curve of decomposition of the precursor solutions for $CaCu_3Ti_4O_{12}$ is shown in Fig. 4.38. The TG curve shows a major weight loss from 200 to ~ 400°C. The weight loss is related to the combustion of organic matrix. On the DSC curve, a main exothermic effect is observed between 200 and 400°C with maxima at 313°C, also indicating that the thermal events are associated with the burnout of organic species involved in the precursor powders. Fig. 4.39 shows the XRD patterns of $CaCu_3Ti_4O_{12}$ in different thermal processing. In the first

step, the sol-gel solution was treated at 500°C for 30min. There are two relatively strong peaks at 35.6 and 38.9° and some minor broad peaks. The two strong peaks correspond to copper oxide (Fig. 4.39 (a)). After treated at 700°C for 2h (Fig. 4.39 (b)), $CaCu_3Ti_4O_{12}$ phase appears. CuO is the secondary phase. After sintering at 1050°C or 1090°C, $CaCu_3Ti_4O_{12}$ is the major phase accompanied by trace of $CaTiO_3$. The copper oxide content might be under the limitation of the measurement due to partial vaporization, which might also explain the weight loss observed in thermogravimetric curve at ca. 1025°C. It is suggested by Guilleemet-Fritsch et al. [138] that the pure $CaCu_3Ti_4O_{12}$ phase is obtained only when the ratio of calcium, copper and titanium are very close to the stoichiometric one. In the present work, the exact pure phase of $CaCu_3Ti_4O_{12}$ has not been obtained. However, the secondary phases might have positive effect on the dielectric behaviour to the material, as discussed in the previous sections.

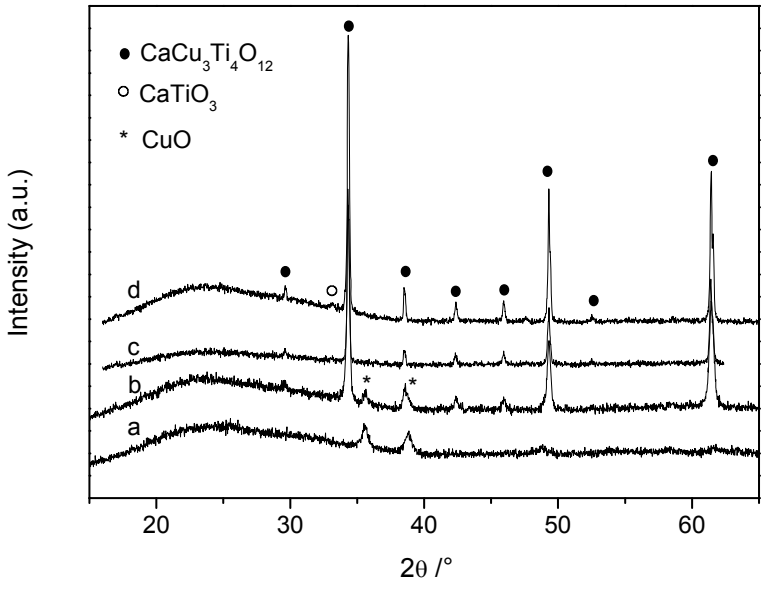

Fig. 4.39 XRD patterns of sample $CaCu_3Ti_4O_{12}$ with thermal treatments of (a) 500°C for 0.5h, (b) 750°C for 2h, (c) 1050°C for 70h and (d) 1090°C for 70h.

The frequency dependence of dielectric response of sample $CaCu_3Ti_4O_{12}$ is shown in Fig. 4.41. Quite high dielectric constant above 2×10^4 with minor frequency dependence is observed. Bigger grains are observed in the sample sintered at 1090°C. Accordingly the higher dielectric constants in this sample are observed. These results prove the qualitative reproducibility of the high-ε_r material by sol-gel process.

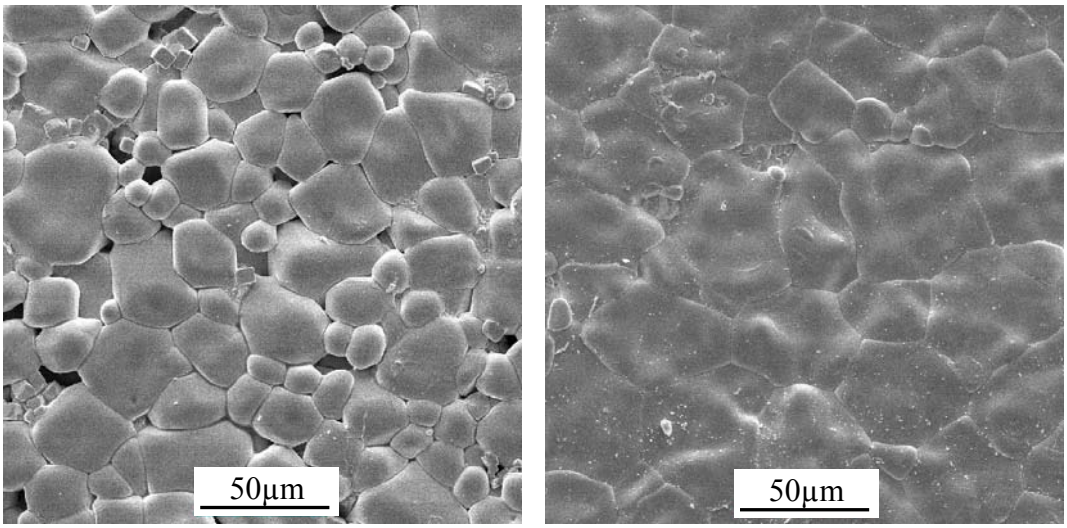

Fig. 4.40 SEM images of sample $CaCu_3Ti_4O_{12}$ sintered at (a) 1050°C and (b) 1090°C.

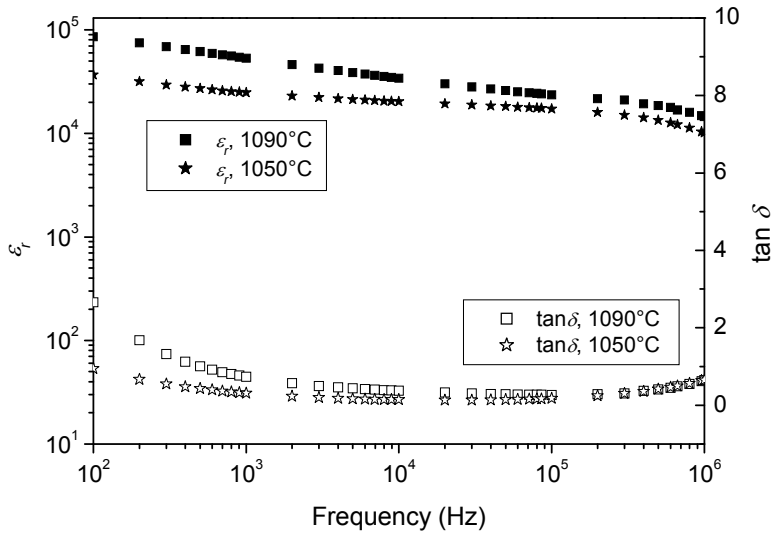

Fig. 4.41 The frequency dependence of ε_r and tan δ of $CaCu_3Ti_4O_{12}$ sintered at 1050°C and 1090°C, respectively.

4.5.2 CuO-rich composite

The composites in two regions inside the ternary system CuO-TiO_2-CaO are found to show giant dielectric constants. They are the composites in CuO-rich region sintered at 950°C and in $CaCu_3Ti_4O_{12}$-rich region sintered at 1050°C. In this section, the dielectric behaviour of the composite (Cu/Ti/Ca of ~ 85/10/5), which was prepared by sol-gel process, has been studied. This sample is denoted as CuO-a. The frequency dependence of dielectric constants and dielectric loss is shown in Fig. 4.42. Quite high dielectric constant values are found in the low frequency range. Typical Debye-like relaxation in the high frequency range is also observed in the sample. Here, it can be concluded that the high dielectric constant composites, which are discovered from the dielectric mapping by parallel synthesis in the ternary system CuO-TiO_2-CaO, keep the high values when the samples are produced by sol-gel process.

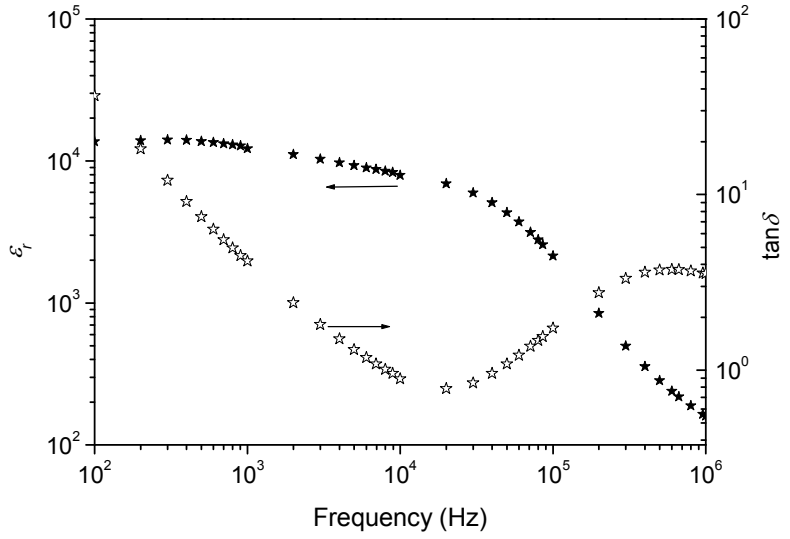

Fig. 4.42 The frequency dependence of ε_r and tan δ of CuO-a sintered at 1050°C and 1090°C, respectively.

5. Summary and Conclusions

A novel parallel synthesis method by injection moulding technique to produce the compositional spreading materials library followed by the honeycomb-dividing and mixing process has been developed in this work.

The ternary system Fe_2O_3-TiO_2-Al_2O_3 is chosen as an example to show the applicability of this new technique. The microstructure difference between original powder and the feedstock show well-arranged and dense structure after mixing with the corresponding binder system. For the nanoscaled powder as Al_2O_3 and TiO_2, although dense structure is obtained, clear agglomerates below 250 nm are found. In comparison, well-dispersed and organized structure for Fe_2O_3 powder with submicron particle size is obtained. The successful injection moulding process confirms good rheological properties of the feedstock. Ex-situ mixing process for the three components has been performed. The homogeneity of mixing is testified by EDX analysis. The tendency of the compositional spreading analyzed by ICP-AES is consistent with the expected calculated composition values. The similar phase relationship with previous reports, the regular tendencies with the variation of the compositions and the linear lattice parameter variation in hematite solid solution prove the reliability of the new parallel synthesis technique.

In this study, paraffin wax-based organic media plays a specific role to produce the library. The mixing of library members is realized by a paint mixer above the melting point of the organic vehicle based on paraffin wax, in which free fluidity for mixing of the different ceramic powders is provided. The final mixing status is easily kept in the cooled solid organic vehicle below the melting point after mixing. The wax medium is used to fix the mixed ceramic powders separated in space. The sedimentation, which probably happens in nano-powder suspensions during aspirating-dispensing by the robot, seems not to be a problem because the particles are totally “fixed” in the solid organic vehicle. One problem existing in the present method is that demixing might occur during the thermal treatment. Hence, the fast thermal treatment for the purpose of quick removing the organic components after mixing is

chosen in order to reduce the possibility of demixing. Meanwhile, the splashing during the quick burning of organic components also prevents the possible demixing.

The parallel synthesis method is further applied to produce variation of the compositions in the ternary system CuO-TiO_2-CaO. Subsolidus phase relationship and dielectric properties in the ternary system CuO-TiO_2-CaO have been studied. Five bi-phasic regions ($CaCu_3Ti_4O_{12}$-$CaTiO_3$, $CaTiO_3$-CuO, CuO-$CaCu_3Ti_4O_{12}$, $CaTiO_3$-Ca_2CuO_3, $CaCu_3Ti_4O_{12}$-TiO_2) and five tri-phasic regions ($CaCu_3Ti_4O_{12}$-$CaTiO_3$-CuO, $CaCu_3Ti_4O_{12}$-CuO-TiO_2, $CaCu_3Ti_4O_{12}$-TiO_2-$CaTiO_3$, $CaTiO_3$-CaO-Ca_2CuO_3, $CaTiO_3$-Ca_2CuO_3-CuO) and only one ternary oxide compound $CaCu_3Ti_4O_{12}$ are found in this system. In tri-phasic region ($CaTiO_3$-Ca_2CuO_3-CuO), additional phase $CaCu_2O_3$ is also observed probably due to partial reaction between Ca_2CuO_3 and CuO.

After dielectric mapping within the ternary system CuO-TiO_2-CaO, giant dielectric constants are found in two regions: one is the CuO-rich region and along the CaO-CuO binary line, in which the composites possess ε_r (>10^4) and can be fabricated in a single step at a low sintering temperature of 950°C; the other is the $CaCu_3Ti_4O_{12}$-rich region sintered at 1050°C. A quite high tan δ is observed in composites in the phase region of ($CaTiO_3$-Ca_2CuO_3-CuO). The low resistivity and Debye relaxation might be two main contributions to the high dielectric loss.

The grain size distributions in most of the giant ε_r composites are found to be bimodal. Smaller grains with secondary phases are located on the surface or the boundaries of the bigger grains, which are composed of the predominant phase. The smaller grains might act as barrier layers and thus enhance the dielectric response of the materials. The $CaCu_3Ti_4O_{12}$-richest sample sintered at 1050°C exhibits a clear grain boundary effect made of liquidus copper oxide phase and smaller grains of $CaTiO_3$ phase. This sample possesses giant dielectric constants (>10^4). In comparison, the sample with same starting composition but sintered at 950°C shows homogeneous microstructure and rather low dielectric constant values (~200) is observed. Similarly, giant dielectric behaviour is also observed in the other composites with the distinct grain boundary microstructure in the $CaCu_3Ti_4O_{12}$-rich region sintered at 1050°C. The $CaTiO_3$ phase can effectively reduce the dielectric loss of the composite but it also decreases the dielectric constants. The results demonstrate the importance of ceramic microstructure, especially the grain boundary effect in controlling the dielectric properties of the material.

Internal barrier layer capacitance (IBLC) model is supposed to be the more probable mechanism to explain such giant dielectric response observed in the high-ε_r materials. The existence of the barrier layers has been confirmed by the frequency and temperature dependences of the dielectric response in the representative high dielectric constant ($>10^4$) composite with molar fraction of Cu/Ti/Ca of ~85/10/5. The barrier layers are probably located at the interfaces between grain and grain boundary. From the temperature dependence of impedance spectra, the equivalent circuit based on three (*RC*) elements connected in series has been estimated. The three (*RC*) elements are bulk, first barrier layer and second barrier layer. The specific resistivity, capacitance and permittivity values show the great contribution of the giant dielectric constant from the barrier layers. The location of the barrier layers is still open to debate. Strong hints suggest that the internal barrier layer effect, possibly located at the grain boundaries, is the main contribution to the observed high dielectric constants.

The reproducibility of the high-ε_r materials prepared by the parallel synthesis method has also been confirmed by sol-gel process. Two representative materials with major $CaCu_3Ti_4O_{12}$ phase and major CuO phase , which were produced by sol-gel process, respectively, exhibit the high dielectric constant values ($>10^4$) at low frequency range. These results qualitatively confirm the reproducibility of the materials by other means. The dielectric response can be significantly altered and modified due to the different microstructure. Therefore, the further modification and optimization of the dielectric response of the material by building up different microstructures remains a challenge in the future study.

6. Outlook

1. The advantage of the present novel parallel synthesis strategy is that the same method can be used for a multitude of ternary component systems. More compositionally varying libraries in smaller increments may be synthesized in a single experiment during honeycomb cutting by use of a honeycomb with smaller cell size. Furthermore, this approach can easily be extended to more complex combinations. A quaternary system for example can be realized by adding one additional layer in shape of prism on top of the ternary system as the fourth component. The schematic set-up is shown in Fig. 6.1. The concentration of the fourth component can be adjusted by the height of the fourth layer, as seen from Fig. 6.1. This method, in contrast to other combinatorial methods, such as thin-film synthesis techniques, etc, offers a new and efficient technique to reveal the complex relation of composition-structure-property of unknown materials systems.

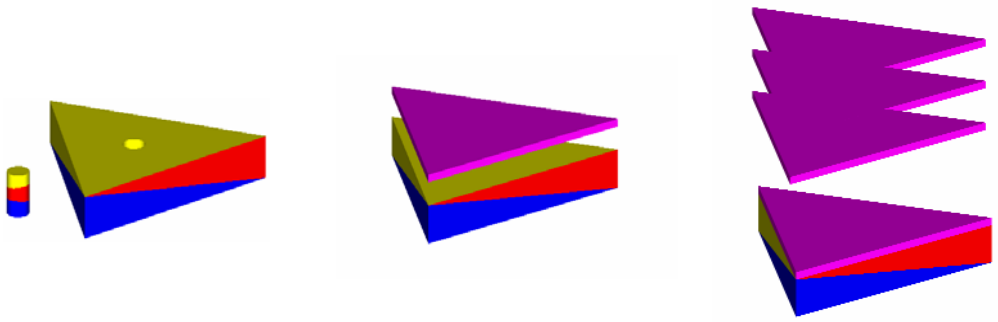

Fig. 6.1 Schematic set-up for parallel synthesis of quaternary system. A quaternary system can be realized by adding one additional layer in shape of prism on top of the ternary system as the fourth component. The concentration of the fourth component can be adjusted by the height of the fourth layer.

In principle the appropriate high-throughput screening tools are important as well to be applied for the evaluation of combinatorial libraries of materials. In the present work, this part is not included.

2. In the development of this novel parallel synthesis method, it is confirmed that injection moulding technique can be used to produce highly precise geometry to realize the three dimensional composition spreading library. In a further step, the honeycomb cutting produces the library members and the ex-situ mixing in the wax-based system can be carried out. In this flow, some factors may be modified, such as the powder size, the choice of the surfactant, the viscosity of the blends, the cutting speed by honeycomb and the firing procedure, etc. All those factors can influence the homogeneity of mixing, the maintenance of the mixing status during firing and finally influence the quality of the final mixtures. These impacts need to be further studied.

3. In the study of composition-structure-property relations in the ternay system CuO-TiO_2-CaO, it is currently premature to associate the special microstructures and phase distributions with the promising dielectric properties of the composites. More investigations such as the temperature dependence of dielectric properties in the representative giant-ε_r composites with different phase and microstructure deserve to be further explored in order to understand the mechanism behind the dielectric behaviour.

4. The inherent problem and the intrinsic limit in parallel synthesis of compositionally varying samples are: different compositions could have very different optimum process conditions [6]. As it is observed in the present study for dielectric property investigation in ternary system CuO-TiO_2-CaO, the best candidates are found in CuO-rich region with sintering temperature of 950°C. The comparable promising dielectric constants values with much smaller dielectric loss values can be achieved in $CaCu_3Ti_4O_{12}$-rich region sintered at 1050°C, which did not show particular good dielectric behaviour when sintered at 950°C. Comparing these two regions, although giant dielectric constants can be obtained in single-step by sintering at 950°C in CuO-rich region, the high dielectric losses in such materials are in no doubt becoming big disadvantages for the application. Whereas in $CaCu_3Ti_4O_{12}$-rich region, much higher sintering temperature are needed to achieve desired microstructure and accordingly

good dielectric response. It is desirable to achieve good quality of the dielectric materials with less energy input to produce such materials.

7. Appendix

7.1 List of abbreviations

Table 7.1 List of abbreviations

XRD	X-ray Diffraction
TG	Thermogravimetry
DSC	Differential scanning calorimetry
ICP-AES	Inductively coupled plasma atomic emission spectroscopy
SEM	Scanning Electron Microscopy
EDX	Energy dispersive X-ray spectroscopy
IS	Impedance spectroscopy

7.2 List of used chemicals

Table 7.2 Chemicals used in the preparation of combinatorial libraries in injection moulding and sol-gel process.

Chemicals	Product name	Supplier
TiO_2	P25	Degussa
Al_2O_3	Aluminiumoxid C	Degussa
Fe_2O_3	1300M	Nordic pigments
$CaCO_3$	SOCAL® 312	Solvay Chemicals
CuO	99+%, 30-50nm	Nanostructured & Amorphous Materials Inc
Stearic acid		Fluka
Stearicamid		Fluka
Decane		Fluka
Paraffin wax	Terhell@ Typ 5405	Schümann
Luwax V	T_m: 46-52°C, Density: 0.935g/cm^3	BASF
$Ti(OiPr)_4$		Sigma-Aldrich
$(CH_3COO)_2Cu \cdot H_2O$		Sigma-Aldrich
$(CH_3COO)_2Ca \cdot xH_2O$		Merck

7.3 List of instruments and equipments

Kneader: Stephan, Hameln, Germany

Injection moulding machine: Allrounder 220M, Arburg

Aluminium honeycomb board (cell size 6.4mm): Euro-composites Co.

Red-devil Painter mixer: Chameleon M & T Machines Ltd.

Stainless steel pressing tool: Paul-Otto-Weber GmbH

400 kN Pressing Machine: Paul-Otto-Weber GmbH

Cold isostatic press: Paul-Otto-Weber GmbH

Optical microscope: Olympus Optical Co. Ltd.

Inductively coupled plasma atomic emission spectroscopy (ICP-AES): Horiba Jobin Yvon GmbH

X-ray diffractometer: D500, Siemens

X-ray diffractometer: X'Pert MRD; Philips

Scanning electron microscope (SEM): JSM 6400F, JEOL

SEM equipped with energy-dispersive X-ray spectroscopy (EDX): ThermoNoran

LCR Meter: Agilent 4284A precision LCR meter

DC resistivity: Model 2425 100W SoureMeter (KEITHLEY)

TG-DSC: Netzsch STA 449 C

7.4 Composition calculation

In a three-layer unit of the ternary system, each composition in this library depends on its geometrical position in the honeycomb and the content of metal oxide in each layer. The total thickness at any cell along the honeycomb net is equal to the sum of the individual thicknesses, which vary proportionally from cell to cell. The composition in molar fraction in each cell of the honeycomb is calculated from the solid loading in the corresponding feedstock, the molecular weight of the components, and the individual thickness ratio of the central point in the respective cell within the honeycomb net. To illustrate the calculation of individual thickness at any point along the three layers, the mathematical and geometric analysis is necessary.

Fig. 7.1 shows geometric analysis to get the mathematic calculation for the individual thickness ratio of any point of three-component system within the honeycomb net. Fig. 7.1 (a) is the vertical view of three layers in x-y coordinate. A vertical plane cutting along MN, which is parallel to BC, is done to get the cross section in order to show the relations of the individual thicknesses from three layers. The individual thicknesses of a random point "P" inside the triangle ABC from layer A, layer B and layer C are supposed to be h_A, h_B, h_C, respectively (Fig. 7.1 (b) and (c)).

Once the geometric setting of the three layers is done, the ratio of h_A: h_B: h_C of a random point P inside this triangle ABC can be easily calculated according to the geometrical relations:

Suppose the side length of triangle ABC is d, then

$$h_A = h \cdot \left(d - (x + y \cdot ctg60^0) \Big/ d \right) \tag{7.1}$$

$$h_B = hy \Big/ d \sin 60° \tag{7.2}$$

$$h_C = h(x \sin 60° + y \cos 60° - y) \Big/ d \sin 60° \tag{7.3}$$

where h_A, h_B, h_C is the thickness of the corresponding up-layer, middle-layer, down-layer, respectively, in a random point inside triangle ABC. d is the side length of triangle ABC. (x, y) is the coordinate values in x-y plane (Fig. 7.1 (a)).

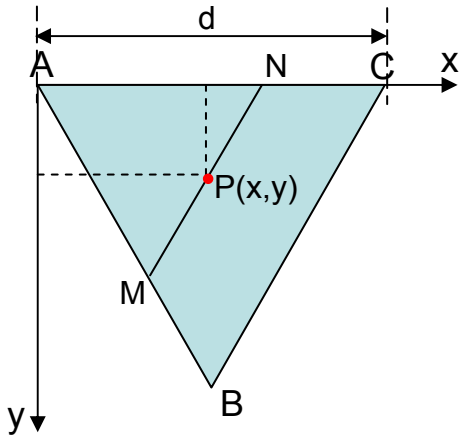

(a)

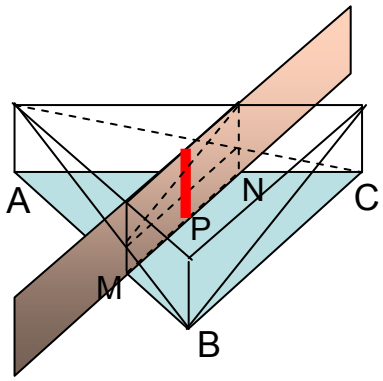

(b)

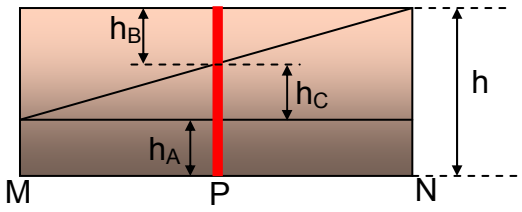

(c)

Fig. 7.1 (a) Vertical view of combinatorial three layers in x-y coordinate; (b) A vertical plane cutting parallel to BC is designated as "MN"; (c) the cross section of the vertical plane cutting of (b). The individual thicknesses of a random point "P" inside the triangular prism ABC from layer A, layer B and layer C are h_A, h_B, h_C, respectively.

After honeycomb cutting, in each cell of the honeycomb, the height ratio from three layers is calculated by the position of the central point of each hexagonal honeycomb cell according to the above equations. Finally, each composition in this library can be calculated according to the thickness ratio of three layers and the content of metal oxide in each layer.

7.5 Parallel synthesis for ternary system CuO-TiO_2-CaO

7.5.1 Photographs of injected and cutted three layers

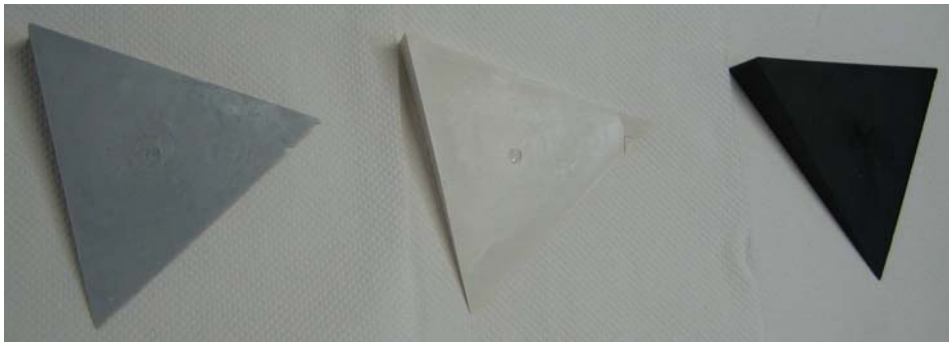

(a)

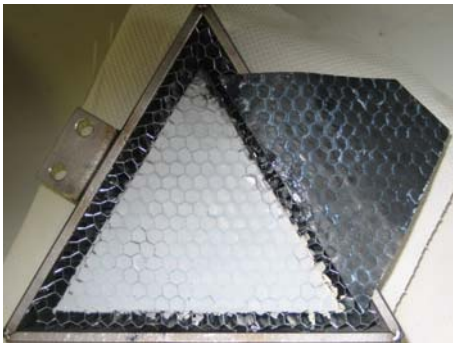

(b)

Fig. 7.2 Photographs of (a) injected three layers, left: $CaCO_3$ layer; middle: TiO_2 layer; right: CuO layer, (b) the product after honeycomb cutting.

7.5.2 Mixing of three components in ternary system CuO-TiO_2-CaO

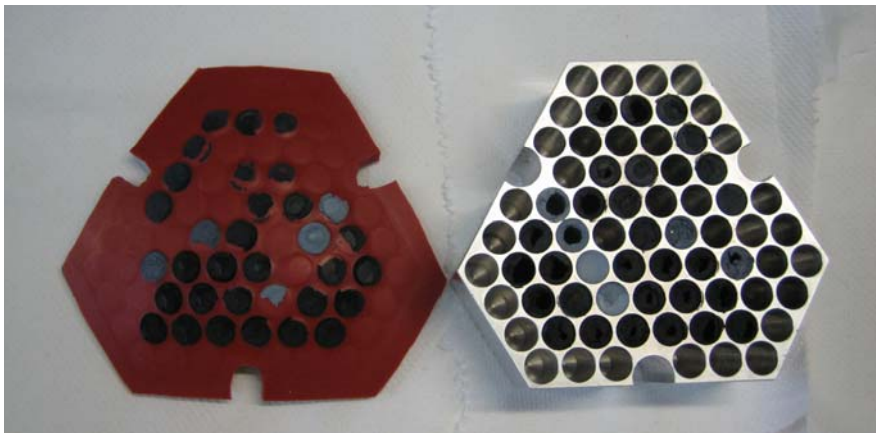

Fig. 7.3 Ex-situ mixed products of the layered pieces in self-made aluminium rack for the ternary system CuO-TiO_2-CaO. Left is the silicone rubber cover for the rack.

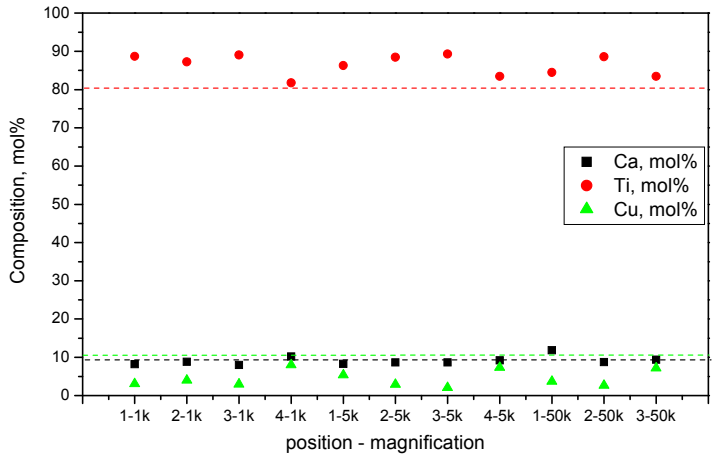

Fig. 7.4 EDX analysis of different positions in magnifications of ×5000, ×50000, ×40000 for the mixture with composition of Cu : Ti : Ca = 10.4: 80.2 : 9.4. Dashed colored lines indicate the calculated composition. Number of x-axis was defined by “position - magnification”.

References

[1] W.F. Maier, K. Stöwe, S. Sieg, Combinatorial and high-throughput materials science, *Angew. Chem. Int. Ed.*, 46, 2007, 6016-6067.

[2] W.F. Maier, The combinatorial approach, *Materialstoday*, 7, 2004, 55-56.

[3] I. Takeuchi, J. Lauterbach, M. J. Fasolka, Combinatorial materials synthesis, *Materialstoday*, 8, 2005, 18-26.

[4] J. C. Zhao, Combinatorial approaches as effective tools in the study of phase diagrams and composition-structure-property relationships, *Prog. Mater. Sci.*, 51, 2006, 557-631.

[5] E.J. Amis, X.-D. Xiang, J.-C. Zhao, Combinatorial materials science: what's new since Edison, *MRS Bull.*, 27, 2002, 295-300.

[6] H. Koinuma, I. Takeuchi, Combinatorial solid-state chemistry of inorganic materials, *Nat. Mater.*, 3, 2004, 429-438.

[7] X.-D. Xiang, X. Sun, G. Briceno, et al. A combinatorial approach to materials discovery. *Science*, 268, 1995, 1738-1740.

[8] R.B. Van Dover, L.F. Schneemeyer, R.M. Fleming, Discovery of a useful thin-film dielectric using a composition-spread approach. *Nature*, 392, 1998, 162-164.

[9] J. C. Zhao, A combinatorial approach for structural materials. *Adv. Eng. Mater.*, 3, 2001, 143-147.

[10] J.R.G. Evans, M.J. Edirisinghe, P.V. Coveney, J. Eames, Combinatorial searches of inorganic materials using the ink-jet printer: science, philosophy and technology. *J. Eur. Ceram. Soc.*, 21, 2001, 2291-2299.

[11] I. Yanase, T. Ohtaki, M. Watanabe, Combinatorial study on nano-particle mixture prepared by robot system, *Appl. Surf. Sci.*, 189, 2002, 292-299.

[12] J. Scheidtmann, D. Klär, J.W. Saalfrank, T. Schmidt, W.F. Maier, Quantitative composition activity relationships (QSAR) of Co-Ni-Mn-mixed oxide and M_1-M_2-mixed oxide catalysts, *QSAR Comb. Sci.*, 24, 2005, 203-210.

[13] Z.Q. Guan, Th. Pfullmann, M. Oehring, R. Bormann, Phase formation during ball milling and subsequent thermal decomposition of Ti-Al-Si powder blends, *J. Alloy. Compd.*, 252, 1997, 245-251.

[14] J.A. Puszkiel, P.A. Larochette, F.C. Gennari, Thermodynamic and kinetic studies of Mg-Fe-H after mechanical milling followed by sintering, *J. Alloy. Compd.*, 463, 2008, 134-142.

[15] M.J. Edirisinghe, J.R.G. Evans, Properties of ceramic injection moulding formulations, *J. Mater. Sci.*, 22, 1987, 269-277.

[16] S. Ren, W. Kochanek, H. Bolz, M. Wittmar, I. Grobelsek, M. Veith, Combinatorial preparation of solid-state materials by injection moulding, *J. Eur. Ceram. Soc.*, 28, 2008, 3005-3010.

[17] A. Boettcher, G. Haase, R. Thun, *Z. Metallk.*, 46, 1955, 386.

[18] K. Kennedy, T. Stefansky, G. Davy, V. F. Zackay, E. R. Parker, Rapid method for determining ternary-alloy phase diagrams, *J. Appl. Phys.*, 36, 1965, 3808-3810.

[19] J. J. Hanak, The "Multiple-Sample Concept" in materials research: synthesis, compositional analysis and testing of entire multicomponent systems, *J. Mater. Sci.*, 5, 1970, 964-971.

[20] X.-D. Xiang, A combinatorial approach to materials discovery, *Science*, 268, 1995, 1738-1740.

[21] X.-D. Xiang, Combinatorial materials synthesis and screening: an integrated materials chip approach to discovery and optimization of functional materials, *Annu. Rev. Mater. Sci.*, 29, 1999, 149-171.

[22] I. Ohkubo, H.M. Christen, P. Khalifah, S. Sathyamurthy, H.Y. Zhai, C.M. Rouleau, D.G. Mandrus, D.H. Lowndes, Continuous composition-spread thin films of transition metal oxides by pulsed-laser deposition, *Appl. Surf. Sci.*, 223, 2004, 35-38.

[23] X.-D. Xiang, Mapping of physical properties-composition phase diagrams of complex material systems using continuous composition material chips. *Appl. Surf. Sci.*, 189, 2002, 188-195.

[24] Y.K. Yoo, Q. Xue, Y.S. Chu, S. Xu, U. Hangen, H.-C. Lee, et al., Identification of amorphous phases in the Fe-Ni-Co ternary alloy system using continuous phase diagram material chips. *Intermetallics*, 14, 2006, 241-247.

[25] G.K. Hubler, C.M. Cotell, C.A. Carosella, S. Schiestel, Metastable materials formation by ion beam assisted deposition: application to metal clusters in ceramic matrices, *Mater. Sci. Eng. A*, 253, 1998, 212-220.

[26] C.X. Wang, G.W. Yang, Thermodynamics of metastable phase nucleation at the nanoscale, *Mater. Sci, Eng. R*, 49, 2005, 157-202.

[27] Q. Jiang, H.M. Lu, Size dependent interface energy and its applications, *Surf. Sci. Rep.*, 63, 2008, 427-464.

[28] K.L. Choy, Chemical vapour deposition of coatings, Prog. Mater. Sci., 48, 2003, 57-170.

[29] J.-C. Zhao, Reliability of the diffusion-multiple approach for phase diagram mapping, *J. Mater. Sci.*, 39, 2004, 3913-3925.

[30] X.N. Jing, J.H. Zhao, L.H. He, 2D aggregate evolution in sintering due to multiple diffusion approaches, *Mater. Chem. Phys.*, 80, 2003, 595-598.

[31] J.-C. Zhao, M.R. Jackson, L.A. Peluso, Determination of the Nb-Cr-Si phase diagram using diffusion multiples, *Acta Materialia*, 51, 2003, 6395-6405.

[32] J.-C. Zhao, A combinatorial approach for efficient mapping of phase diagrams and properties, *J. Mater. Res.*, 16, 2001, 1565-1578.

[33] E.W. McFarland, W.H. Weinberg, Combinatorial approaches to materials discovery, *Trends in Biotech.*, 17, 1999, 107-115.

[34] K.K.B. Hon, L. Li, I.M. Hetchings, Direct writing technology – advances and developments, *CIRP Annals – Manufacturing Technology*, 57, 2008, 601-620.

[35] L. Chen, J. Bao, C. Gao, Combinatorial synthesis of insoluble oxide library from ultrafine/nano particle suspension using a drop-on-demand inkjet delivery system. *J. Comb. Chem.*, 6, 2004, 699-702.

[36] K. Fujimoto, S. Ito, S. Suehara, S. Inoue, M. Watanabe, Effective algorithm for material exploration in ceramics with combinatorial technology. *J. Eur. Ceram. Soc.*, 26, 2006, 731-734.

[37] X. Zhao, J.R.G. Evans, M.J. Edirisinghe, J.H. Song, Formulation of a ceramic ink for a wide-array drop-on-demand ink-jet printer, *Ceram. Int.*, 29, 2003, 887-892.

[38] J. Wang, M.M. Mohebi, J.R.G. Evans, Two methods to generate multiple compositions in combinatorial ink-jet printing of ceramics. *Macromol. Rapic Commun.*, 26, 2005, 304-309.

[39] J. Wang, J.R.G. Evans, Segregation in multicomponent ceramic colloids during drying of droplets. *Phys. Rev. E*, 73, 2006, 021501.

[40] J.A. Lewis, J.E. Smay, J. Stuecker, J. Cesarano III, Direct ink writing of three-dimensional ceramic structures, *J. Am. Ceram. Soc.*, 89, 2006, 3599-3609.

[41] Y. Zhang, L. Chen, S. Yang, J.R.G. Evans, Control of particle segregation during drying of ceramic suspension droplets, *J. Eur. Ceram. Soc.*, 27, 2007, 2229-2235.

[42] S. Yang, J.R.G. Evans, Metering and dispensing of powder; the quest for new solid freeforming techniques, *Powder Technol.*, 178, 2007, 56-72.

[43] J. Wang, J.R.G. Evans, Drying behaviour of droplets of mixed powder suspensions, *J. Eur. Ceram. Soc.*, 26, 2006, 3123-3131.

[44] J. Klein, T. Zech, J.M. Newsam, S.A. Schunk, Application of a novel split & Pool-principle for the fully combinatorial synthesis of functional inorganic materials, *Appl. Catal. A,* 254, 2003, 121-131.

[45] K.S. Lam, M. Lebl, V. Krchnak, The „one-bead-one-compound“ combinatorial library method, *Chem. Rev.*, 97, 1997, 411-448.

[46] T. Konishi, T. Hondo, T. Araki, K. Nishio, T. Tsuchiya, T. Matsumoto, S. Suehara, S. Todoroki, S. Inoue, Investigation of glass formation and color properties in the P_2O_5-TeO_2-ZnO system, *J. Non-Cryst. Solids*, 324, 2003, 58-66.

[47] R.M. German, K.F. Hens, S.T. Lin, Key issues in powder injection moulding, *Bull. Am. Ceram. Soc.*, 70, 1991, 1294-1302.

[48] H. Ye, X.Y. Liu, H. Hong, Fabrication of metal matrix composites by metal injection moulding – a review, *J. Mater. Process. Tech.*, 200, 2008, 12-24.

[49] M.J. Edirisinghe, J.R.G. Evans, Systematic development of the ceramic injection moulding process, *Mater. Sci. Eng. A*, 109, 1989, 17-26.

[50] P. Suri, S.V. Atre, R.M. German, J.P. de Souza, Effect of mixing on the rheology and particle characteristics of tungsten-based powder injection moulding feedstock, *Mater. Sci. Eng. A*, 356, 2003, 337-344.

[51] J.J. Reddy, N. Ravi, M. Vijayakumar, A simple model for viscosity of powder injection moulding mixes with binder content above powder critical binder volume concentration, *J. Eur. Ceram. Soc.*, 20, 2000, 2183-2190.

[52] Z.Y. Liu, N.H. Loh, S.B. Tor, K.A. Khor, Y. Murakoshi, R. Maeda, Binder system for micropowder injection moulding, *Mater. Lett.*, 48, 2001, 31-38.

[53] J. Karch, R. Birringer, H. Gleiter, Ceramics ductile at low temperature, *Nature*, 330, 1987, 556-558.

[54] M.R. Gallas, B. Hockey, A. Pechenik, G.J. Piermarini, Fabrication of transparent γ-Al_2O_3 from nanosize particles, *J. Am. Ceram. Soc.*, 77, 1994, 2107-2112.

[55] B.A. Rozenberg, R. Tenne, Polymer-assisted fabrication of nanoparticles and nanocomposites, *Prog. Polym. Sci.*, 33, 2008, 40-112.

[56] J. Kraus, Spritzgießen nanoskaliger keramischer Pulver am Beispiel des Degussa Aluminiumoxid C, Ph. D Thesis, INM – Leibniz Institute for New Materials, INM and Universität des Saarlandes, Saarbrücken, Germany, 1999.

[57] A.A. Fotiev, L.L. Surat, A.I. Tretyakov, Phase relationships in the Al_2O_3-Fe_2O_3-TiO_2-V_2O_5, Cr_2O_3-Fe_2O_3-TiO_2-V_2O_5, and Al_2O_3-Cr_2O_3-TiO_2-V_2O_5 systems, *Russ. J. Inorg. Chem.*, 25, 1981, 739-743.

[58] M. I. Pownceby, , Constanti-Carey, K. K. and Fisher-White, M. J., Subsolidus phase relationships in the system Fe_2O_3-Al_2O_3-TiO_2 between 1000° and 1300°C. *J. Am. Ceram. Soc.*, 86, 2003, 975-980.

[59] A. M. M. Gadalla and J. White, Equilibrium relationships in the system CuO-Cu_2O-CaO, *Trans. Br. Ceram. Soc.*, 65, 1966, 181-190.

[60] C. –F. Tsang, J. K. Meen, D. Elthon, Phase equilibria of the calcium oxide – copper oxide system in oxygen at 1 atm, *J. Am. Ceram. Soc.*, 78, 1995, 1863-1868.

[61] R. S. Roth, N. M. Hwang, C. J. Rawn, B. P. Burton, J. J. Ritter, Phase equilibria in the systems CaO-CuO and CaO-Bi_2O_3, *J. Am. Ceram. Soc.*, 74, 1991, 2148-2151.

[62] R. C. Devries, R. Roy, E. F. Osborn, Phase equilibrium in the system CaO-TiO_2, *J. Phys. Chem*., 58, 1954, 1069-1073.

[63] A. Jongejan, A. L. Wilkins, A re-examination of the system CaO-TiO_2 at liquidus temperatures, *J. Less-Common Metals.*, 20, 1970, 273-279.

[64] F.-H. Lu, F.-X. Fang, Y.-S. Chen, Eutectic reaction between copper oxide and titanium dioxide, *J. Eur. Ceram. Soc.*, 21, 2001, 1093-1099.

[65] K.T. Jacob, C. Shekhar, X. Li, G.M. Kale, Gibbs energy of formation of $CaCu_3Ti_4O_{12}$ and phase relations in the ternary system CaO-CuO/Cu_2O-TiO_2, *Acta Mater.*, 56, 2000, 4798-4803.

[66] H. Chen, T.N. Cong, W. Yang, C. Tan, Y. Li, Y. Ding, Progress in electrical energy storage system: a critical review, *Prog. Nat. Sci.*, 19, 2009, 291-312.

[67] K. Asami, Characterization of heterogeneous systems by dielectric spectroscopy, *Prog. Polym. Sci.*, 27, 2002, 1617-1659.

[68] R. Waser, U. Böttger, S. Tiedke, Polar oxides: properties, characterization and imaging, Wiley-VCH Verlag GmbH & Co. KGaA, Weinheim, 2005, ISBN: 3-527-40532-1, 11-38.

[69] K. Maex, M.R. Baklanov, D. Shamiryan, F. Lacopi, S.H. Brongersma, Z.S. Yanovitskaya, Low dielectric constant materials for microelectrics, *J. Appl. Phys.*, 93, 2003, 8793-8841.

[70] P. Kötz, M. Carlen, Principles and applications of electrochemical capacitors, *Electrochimica Acta*, 45, 2000, 2483-2498.

[71] H. Weiss, Physics and technology of data storage, *Solid-State Electronics*, 19, 1976, 347-356.

[72] M.G. Kanatzidis, K.R. Poeppelmeier, et al., Report from the third workshop on future directions of solid-state chemistry: the status of solid-state chemistry and its impact in the physical sciences, *Prog. Solid State Chem.*, 36, 2007, 1-133.

[73] Q. Ling, D. Liaw, C. Zhu, D. Chan, E. Kang, K. Neoh, Polymer electronic memories: materials, devices and mechanisms, *Prog. Poly. Sci.*, 33, 2008, 917-978.

[74] D.K. Hale, The physical properties of composite materials, *J. Mater. Sci*., 11, 1976, 2105-2141.

[75] Z. Surowiak, M.F. Kupriyanov, D. Czekaj, Properties of nanoscrystalline ferroelectric PZT ceramics, *J. Eur. Ceram. Soc.*, 21, 2001, 1377-1381.

[76] L.B. Kong, T.S. Zhang, J. Ma, F. Boey, Progress in synthesis of ferroelectric ceramic materials via high-energy mechanochemical technique, *Prog. Mater. Sci.*, 53, 2008, 207-322.

[77] L. Mitoseriu, L. Stoleriu, M. Viviani, D. Piazza, M.T. Buscaglia, R. Calderone, V. Buscaglia, A. Stancu, P. Nanni, C. Galassi, Influence of stoichiometry on the dielectric and ferroelectric properties of the tunable (Ba,Sr)TiO_3 ceramics investigated by first order reversal curves method, *J. Eur. Ceram. Soc.*, 26, 2006, 2915-2921.

[78] J. Smolander, M. Ahtee, Electrostatics of the ferroelectric phases of $BaTiO_3$, *J. Phys. Chem. Solids*, 44, 1983, 1-12.

[79] S.M. Gupta, A.R. Kulkarni, Synthesis and dielectric properties of lead magnesium niobate a review, Mater. *Chem. Phys.*, 39, 1994, 98-109.

[80] X. Chen, H. Fan, Y. Fu, L. Liu, J. Chen, Low-temperature fabrication and crystallization behaviour of $Pb(Mg_{1/3}Nb_{2/3}O_3)$ crystallites by a hydrothermal process, *J. Alloy. Compd.*, 469, 2009, 322-326.

[81] J. Wu, C. Nan, Y, Lin, Y. Deng, Giant dielectric permittivity observed in Li and Ti doped NiO, *Phys. Rev. Lett.*, 89, 2002, 217601.

[82] G.D. Wilk, R. M. Wallace, J. M. Anthony, High-k gate dielectrics: current status and materials properties considerations, *J. Appl. Phys.*, 89, 2001, 5243-5275.

[83] N. Setter, R. Waser, Electroceramic materials, *Acta Mater.*, 48, 2000, 151-178.

[84] M. A. Subramanian, D. Li, N. Duan, B. A. Reisner, A. W. Sleight, High dielectric constant in $ACu_3Ti_4O_{12}$ and $ACu_3Ti_3FeO_{12}$ phases, *J. Solid. State. Chem.*, 151, 2000, 323-325.

[85] P. Lunkenheimer, V. Bobnar, A.V. Pronin, A.I. Ritus, A.A. Volkov, A. Loidl, Origin of apparent colossal dielectric constants, *Phy. Rev. B*, 66, 2002, 052105.

[86] I.P. Raevski, S.A. Prosandeev, A.S. Bogatin, M.A. Malitskaya, L. Jastrabik, High dielectric permittivity in $AFe_{1/2}B_{1/2}O_3$ nonferroelectric perovskite ceramics (A=Ba, Sr, Ca; B=Nb, Ta, Sb), *J. Appl. Phys.*, 93, 2003, 4130-4136.

[87] M.A. Ramirez, P.R. Bueno, J.A. Varela, E. Longo, Non-ohmic and dielectric properties of a $Ca_2Cu_2Ti_4O_{12}$ polycrystalline system, *Appl. Phys. Lett.*, 89, 2006, 212102.

[88] S.-Y. Chung, Lattice distortion and polarization switching in calcium copper titanate, *Appl. Phys. Lett.*, 87, 2005, 052901.

[89] B. Bochu, M. N. Deschizeaux, J. C. Joubert, A. Collomb, J. Chenavas, M. Marezio, Synthèse et caractérisation d'une série de titanates perovskites isotypes de $CaCu_3Mn_4O_{12}$, *J. Solid State. Chem.*, 29, 1979, 291-298.

[90] L. He, J.B. Neaton, M.H. Cohen, D. Vanderbilt, First-principles study of the structure and lattice dielectric response of $CaCu_3Ti_4O_{12}$, *Phys. Rev. B*, 65, 2002, 214112.

[91] D.C. Sinclair, T.B. Adams, F.D. Morrison, A.R. West, $CaCu_3Ti_4O_{12}$: One-step internal barrier layer capacitor, *Appl. Phys. Lett.*, 80, 2002, 2153-2155.

[92] D.C. Sinclair, A.R. West, Impedance and modulus spectroscopy of semiconducting $BaTiO_3$ showing positive temperature coefficient of resistance, *J. Appl. Phys.*, 66, 1989, 3850-3856.

[93] G.A. Samara, The relaxational properties of comopositionally disordered ABO_3 perovskites, *J. Phys.: Condens. Matter*, 15, 2003, R367-R411.

[94] B.S. Prakash, K.B.R. Varma, Influence of sintering conditions and doping on the dielectric relaxation originating from the surface layer effects in $CaCu_3Ti_4O_{12}$ ceramics, *J. Phys. Chem. Solid*, 68, 2007, 490-502.

[95] M.-H. Whangbo, M.A. Subramanian, Structural model of planar defects in $CaCu_3Ti_4O_{12}$ exhibiting a giant dielectric constant, *Chem. Mater.*, 18, 2006, 3257-3260.

[96] V. Brize, G. Gruener, J. Wolfman, K. Fatyeyeva, M. Tabellout, M. Gervais, F. Gervais, Grain size effects on the dielectric constant of $CaCu_3Ti_4O_{12}$ ceramics, *Mater. Sci. Eng. B*, 2006, 129, 135-138.

[97] S. Sarkar, P. K. Jana, B. K. Chaudhuri, Copper (II) oxide as a giant dielectric material, *Appl. Phys. Lett.*, 89, 2006, 212905.

[98] S. Pongha, P. Thongbai, T. Yamwong, S. Maensiri, Giant dielectric response and polarization relaxation mechanism in (Li, V)-doped NiO ceramics, *Scripta Materialia*, 60, 2009, 870-873.

[99] W.Y. Wang, D.F. Zhang, X.L. Chen, Nonlinear electrical characteristics and dielectric properties of (Ca, Ta)-doped TiO_2 ceramics, *J. Mater. Sci.*, 38, 2003, 2049-2054.

[100] W.Y. Wang, D.F. Zhang, T. Xu, Y.P. Xu, T. Zhou, B.Q. Hu, C.Y. Wang, L.S. Wu, X.L. Chen, Nonlinear electrical characteristics and dielectric properties of Ca, Ta-doped TiO_2 varistors, *Appl. Phys. A*, 76, 2003, 71-75.

[101] W.Y. Wang, D.F. Zhang, T. Xu, X.F. Li, T. Zhou, X.L. Chen, Effect of temperature on nonlinear electrical behaviour and dielectric properties of (Ca, Ta)-doped TiO_2 ceramics, *Mater. Res. Bull.*, 37, 2002, 1197-1206.

[102] C. Li, J. Wang, X. Wang, H. Chen, W. Su, Nonlinear electrical properties of Ta-doped titania capacitor-varistor ceramics, *Mater. Chem. Phys.*, 74, 2002, 187-191.

[103] J. Liu, C. Duan, W. Yin, W.N. Mei, R.W. Smith, J.R. Hardy, Large dielectric constant and Maxwell-Wagner relaxation in $Bi_{2/3}Cu_3Ti_4O_{12}$, *Phys. Rev. B*, 70, 2004, 144106.

[104] B. Barbier, C. Combettes, S. Guillemet-Fritsch, T. Chartier, F. Rossignol, A. Rumeau, T. Lebey, E. Dutarde, $CaCu_3Ti_4O_{12}$ ceramics from co-precipitation method: Dielectric properties of pellets and thick films, *J. Eur. Ceram. Soc.*, 29, 2009, 731-735.

[105] C.C. Homes, T. Vogt, S.M. Shapiro, S. Wakimoto, A.P. Ramirez, Optical response of high-dielectric-constant perovskite-related oxide, *Science*, 293, 2001, 673-676.

[106] M.-J. Pan, B.A. Bender, A bimodal grain size model for predicting the dielectric constant of calcium copper titanate ceramics, *J. Am. Ceram. Soc.*, 88, 2005, 2611-2614.

[107] L. Wu, Y. Zhu, S. Park, S. Shapiro, G. Shirane, Defect structure of the high-dielectric-constant perovskite $CaCu_3Ti_4O_{12}$, *Phys. Rev. B*, 71, 2005, 014118.

[108] G.H. Haertling, Ferroelectric ceramics: history and technology, *J. Am. Ceram. Soc.*, 82, 1999, 797-818.

[109] J. Li, A.W. Sleight, M.A. Subramanian, Evidence for internal resistive barriers in a crystal of the giant dielectric constant material: $CaCu_3Ti_4O_{12}$, *Solid State Commun.*, 135, 2005, 260-262.

[110] A.P. Ramirez, M.A. Subramanian, M. Gardel, G. Blumberg, D. Li, T. Vogt, S.M. Shapiro, Giant dielectric constant response in a copper-titanate, *Solid State Commun.*, 115, 2000, 217-220.

[111] N. Kolev, R.P. Bontchev, A.J. Jacobson, V.N. Popov, V.G. Hadjiev, A.P. Litvinchuk, M.N. Iliev, Raman spectroscopy of $CaCu_3Ti_4O_{12}$, *Phys. Rev. B*, 66, 2002, 132102.

[112] C.C. Homes, T. Vogt, S.M. Shapiro, S. Wakimoto, M.A. Subramanian, A.P. Ramirez, Charge transfer in the high dielectric constant materials $CaCu_3Ti_4O_{12}$ and $CdCu_3Ti_4O_{12}$, *Phys. Rev. B*, 67, 2003, 092106.

[113] M.H. Cohen, J.B. Neaton, L. He, D. Vanderbilt, Extrinsic models for the dielectric response of $CaCu_3Ti_4O_{12}$, *J. Appl. Phys.*, 94, 2003, 3299-3305.

[114] A. Tselev, C.M. Brooks, S.M. Anlage, H. Zheng, L. Salamanca-Riba, R. Ramesh, M.A. Subramanian, Evidence for power-law frequency dependence of intrinsic dielectric response in the $CaCu_3Ti_4O_{12}$, *Phys. Rev. B*, 70, 2004, 144101.

[115] B.S. Prakash, K.B.R. Varma, Effect of sintering conditions on the dielectric properties of $CaCu_3Ti_4O_{12}$ and $La_{2/3}Cu_3Ti_4O_{12}$ ceramics: a comparative study, *Physica B*, 382, 2006, 312-319.

[116] C.C. Calvert, W.M. Rainforth, D.C. Sinclair, A.R. West, EELS characterisation of bulk $CaCu_3Ti_4O_{12}$ ceramics, *Micron*, 37, 2006, 412-419.

[117] G. Chiodelli, V. Massarotti, D. Capsoni, M. Bini, C.B. Azzoni, M.C. Mozzati, P. Lupotto, Electric and dielectric properties of pure and doped $CaCu_3Ti_4O_{12}$ perovskite materials, *Solid State Commun.*, 132, 2004, 241-246.

[118] P. Leret, J.F. Fernandez, J. de Frutos, D. Fernandez-Hevia, Nonlinear I-V electrical behaviour of doped $CaCu_3Ti_4O_{12}$ ceramics, *J. Eur. Ceram. Soc.*, 27, 2007, 3901-3905.

[119] T.-T. Fang, L.-T. Mei, H.-F. Ho, Effects of Cu stoichiometry on the microstructures, barrier-layer structures, electrical conduction, dielectric responses, and stability of $CaCu_3Ti_4O_{12}$, *Acta. Mater.*, 54, 2006, 2867-2875.

[120] M.A. Subramanian, A.W. Sleight, $ACu_3Ti_4O_{12}$ and $ACu_3Ru_4O_{12}$ perovskites: high dielectric consants and valence degeneracy, *Solid State Sci.*, 4, 2002, 347-351.

[121] J. Liu, C. Duan, W.N. Mei, R.W. Smith, J.R. Hardy, Dielectric properties and Maxwell-Wagner relaxation of compounds $ACu_3Ti_4O_{12}$ (A=Ca, $Bi_{2/3}$, $Y_{2/3}$, $La_{2/3}$), *J. Appl. Phys.*, 98, 2005, 093703.

[122] L. Liu, H. Fan, P. Fang, L. Jin, Electrical heterogeneity in $CaCu_3Ti_4O_{12}$ ceramics fabricated by sol-gel method, *Solid State Commun.*, 142, 2007, 573-576.

[123] I.M. Hodge, M.D. Ingram, A.R. West, Impedance and modulus spectroscopy of polycrystalline solid electrolytes, *J. Electroanal. Chem.*, 74, 1976, 125-143.

[124] T.B. Adams, D.C. Sinclair, A.R. West, Characterization of grain boundary impedances in fine- and coarse-grained $CaCu_3Ti_4O_{12}$ ceramics, *Phys. Rev. B*, 73, 2006, 094124.

[125] D. Capsoni, M. Bini, V. Massarotti, G. Chiodelli, M.C. Mozzatic, C.B. Azzoni, Role of doping and CuO segregation in improving the giant permittivity of $CaCu_3Ti_4O_{12}$, *J. Solid State Chem.*, 177, 2004, 4494-4500.

[126] A.R. West, T.B. Adams, F.D. Morrison, D.C. Sinclair, Novel high capacitance materials: $BaTiO_3$: La and $CaCu_3Ti_4O_{12}$, *J. Eur. Ceram. Soc.*, 24, 2004, 1439-1448.

[127] L.M. Levinson (Ed.), Electronic ceramics: properties, devices and applications, Marcel Dekker, New York, 1988.

[128] W. Wersing, Microwave ceramics for resonators and filters, *Curr. Opin. Solid St. Mater. Sci.*, 1, 1996, 715-731.

[129] D.R. Clarke, Varistor ceramics, *J. Am. Ceram. Soc.*, 82, 1999, 485-502.

[130] R. Freer, C. Leach, Local properties of grain boundaries in semiconducting ceramics, *Solid State Ionics*, 173, 2004, 41-51.

[131] F. Greuter, G. Blatter, Electrical properties of grain boundaries in polycrystalline compound semiconductors, *Semicond. Sci. Technol.*, 5, 1990, 111-137.

[132] D.R. Clarke, Grain boundaries in polycrystalline ceramics, *Ann. Rev. Mater. Sci.*, 17, 1987, 57-74.

[133] B.S. Prakash, K.B.R. Varma, Effect of the addition of B_2O_3 and BaO-B_2O_3-SiO_2 glasses on the microstructure and dielectric properties of grain dielectric constant material $CaCu_3Ti_4O_{12}$, *J. Solid State Chem.*, 180, 2007, 1918-1927.

[134] L. Ni, X.M. Chen, X.Q. Liu, R.Z. Hou, Microstructure-dependent giant dielectric response in $CaCu_3Ti_4O_{12}$ ceramics, *Solid State Commun.*, 139, 2006, 45-50.

[135] T.-T. Fang, L.-T. Mei, Evidence of Cu deficiency: a key point for the understanding of the mystery of the giant dielectric constant in $CaCu_3Ti_4O_{12}$, *J. Am. Ceram. Soc.*, 90, 2007, 638-640.

[136] T.-T. Fang, C.P. Liu, Evidence of the internal domains for inducing the anomalously high dielectric constant of $CaCu_3Ti_4O_{12}$, *Chem. Mater.*, 17, 2005, 5167-5171.

[137] T.B. Adams, D.C. Sinclair, A.R. West, Giant barrier layer capacitance effects in $CaCu_3Ti_4O_{12}$ ceramics, *Adv. Mater.*, 14, 2002, 1321-1323.

[138] S. Guillemet-Fritsch, T. Lebey, M. Boulos, B. Durand, Dielectric properties of $CaCu_3Ti_4O_{12}$ based multiphased ceramics, *J. Eur. Ceram. Soc.*, 26, 2006, 1245-1257.

[139] W. Kobayashi, I. Terasaki, $CaCu_3Ti_4O_{12}/CaTiO_3$ composite dielectrics: Ba/Pb-free dielectric ceramics with high dielectric constants, *Appl. Phys. Lett.*, 87, 2005, 032902.

[140] S.Y. Chung, I.L.D. Kim, S.J.L. Kang, Strong nonlinear current-voltage behaviour in perovskite-derivative calcium copper titanate, *Nat. Mater.*, 3, 2004, 774-778.

[141] K.S. Cole, R.H. Cole, Dispersion and absorption in dielectrics, I. alternating current characteristics, *J. Chem. Phys.*, 9, 1941, 341-351.

[142] K.S. Cole, R.H. Cole, Dispersion and absorption in dielectrics, II. direct current characteristics, *J. Chem. Phys.*, 10, 1942, 98-105.

[143] S. Pekhson, Models of relaxation in glass, *J. Non-Cryst. Solids*, 95-96, 1987, 131-147.

[144] P. Lunkenheimer, R. Fichtl, S.G. Ebbinghaus, A. Loidl, Nonintrinsic origin of the colossal dielectric constants in $CaCu_3Ti_4O_{12}$, *Phys. Rev. B*, 70, 2004, 172102.

[145] M.J. Edirisinghe, J.R.G. Evans, Review: fabrication of engineering ceramics by injection moulding, II. Techniques, *Int. J. High Tech. Ceram.*, 2, 1986, 249-278.

[146] R.K. Thakur, C.Vial, K.D.P. Nigam, E.B. Nauman, G. Djelveh, Static mixers in the process industries – a review, *Chem. Eng. Res. Design*, 81, 2003, 787-826.

[147] M.T. Zaky, Effect of solvent debinding variables on the shape maintenance of green molded bodies, *J. Mater. Sci.*, 39, 2004, 3397-3402.

[148] S. Ahn, S.J. Park, S. Lee, S.V. Atre, R.M. German, Effect of powders and binders on material properties and molding parameters in iron and stainless steel powder injection moulding process, *Poweder Technology*, 193, 2009, 162-169.

[149] Z. Xie, J. Luo, X. Wang, J. Li, Y. Huang, The effect of organic vehicle on the injection moulding of ultra-fine zirconia powders, *Materials & Design*, 26, 2005, 79-82.

[150] T.Y. Chan, S.T. Lin, Effects of Stearic acid on the injection moulding of alumina, *J. Am. Ceram. Soc.*, 78, 1995, 2746-2752.

[151] S.P. Rwei, I. Manas-Zloczower, D.L. Feke, Observation of carbon black agglomerate dispersion in simple shear flows, *Polym. Eng. Sci.*, 30, 1990, 701-706.

[152] B.C. Mutsuddy, R.G. Ford, Ceramic injection moulding, Chapman & Hall, UK, 1995, p. 39.

[153] J. Baldyga, L. Makowski, W. Orciuch, C. Sauter, H.P. Schuchmann, Deagglomeration processes in high-shear devices, *Chem. Eng. Res. Design*, 86, 2008, 1369-1381.

[154] E. Kato, K. Daimon, J. Takahashi, Decomposition temperature of β-Al_2TiO_5. *J. Am. Ceram. Soc.*, 63, 1980, 355-356.

[155] B. Freudenberg, A. Mocellin, Aluminium titanate formation by solid-state reaction of fine Al_2O_3 and TiO_2 powders, *J. Am. Ceram. Soc.*, 70, 1987, 33-38.

[156] T.S. Liu, D.S. Perera, Long-term thermal stability and mechanical properties of aluminium titanate at 1000-1200°C, *J. Mater. Sci.*, 33, 1998, 995-1001.

[157] N.N. Greenwood, A. Earnshaw, Chemistry of the elements, Butterworth-Heinemann, Oxford, 1997, pp. 222, 1074.

[158] M. Subbanna, P.C. Kapur, Pradip, Computer-aided control of evolution of microstructure during sintering, *Mater. Chem. Phys.*, 67, 2001, 17-24.

[159] S.I. Stupp, P.V. Braun, Molecular manipulation of microstructures: biomaterials, ceramics, and semiconductors, *Science*, 277, 1997, 1242-1248.

[160] W.J. Clegg, Design of ceramic laminates for structural applications, *Mater. Sci. Tech.*, 14, 1998, 483-495.

[161] J.K. Jain, R.K. Kamilla, Quantitative study of large composite-fermion systems, *Phys. Rev. B*, 55, 1997, R4895-R4898.

[162] J. Tartaj, G.L. Messing, Anisotropic grain growth in α-Fe_2O_3-doped alumina, *J. Eur. Ceram. Soc.*, 17, 1997, 719-725.

[163] M. Hillert, On the theory of normal and abnormal grain growth, *Acta Metal.*, 13, 1965, 227-238.

[164] M. Avrami, Granulation, phase change, and microstructure kinetics of phase change. III, *J. Chem. Phys.*, 9, 1941, 177-184.

[165] N. Fujimura, T. Nishihara, S. Goto, J. Xu, T. Ito, Control of preferred orientation for ZnOx films: control of self-texture, *J. Cryst. Growth*, 130, 1993, 269-279.

[166] D.P. Tracy, D.B. Knorr, K.P. Rodbell, Texture in multilayer metallization structures, *J. Appl. Phys.*, 76, 1994, 2671-2680.

[167] I.-S. Kim, M. Itoh, T. Nakamura, Electrical conductivity and metal-nonmetal transition in the perovskite-related layered system $Ca_{n+1}TinO_{3n+1-\delta}$ (n = 2, 3, and ∞), *J. Solid State Chem.*, 101, 1992, 77-86.

[168] G. Pfaff, Synthesis of calcium titanate powders by the sol-gel process, *Chem. Mater.*, 6, 1994, 58-62.

[169] M. Ceh, D. Kolar, Solubility of CaO in $CaTiO_3$, *J. Mater. Sci.*, 29, 2994, 6295-6300.

[170] K.T. Jacob, K.P. Abraham, Thermodynamic properties of calcium titanates: $CaTiO_3$, $Ca_4Ti_3O_{10}$ and $Ca_3Ti_2O_7$, *J. Chem. Thermodyn.*, 41, 2009, 816-820.

[171] L. W. Coughanour, R. S. Roth, V. A. DeProsse, Phase equilibrium relations in the systems Lime-Titania and Zirconia-Titania, *J. Research NBS.*, 52, 1954, 37-42.

[172] R.M. Vezikova, V.M. Gropyanov, Phase composition of sintered lime refractories with TiO_2 additions, *Refractories*, 34, 1993, 87-90.

[173] R. S. Roth, Revision of the phase equilibrium diagram of the binary system calcia-titania, showing the compound $Ca_4Ti_3O_{10}$, *J. Research NBS.*, 61, 1958, 437-440.

[174] K.H. Breuer, W. Eysel, Powder Diffraction File, Card No. 34-284. International Centre for Diffraction Data, Newtowne Square, PA, 1993.

[175] A.M. Yankin, Y.V. Golikov, R.G. Zakharov, O.A. Vikhreva, I.N. Dubrovina, V.F. Balakirev, Phase equilibria in the Ca-Cu-O system under variable temperatures and oxygen pressures, *Ceram. Int.*, 22, 1996, 83-85.

[176] S. Sarkar, P.K. Jana, B.K. Chaudhuri, Colossal internal barrier layer capacitance effect in polycrystalline copper (II) oxide, *Appl. Phys. Lett.*, 92, 2008, 022905.

[177] J.A. Kittl, K. Opsomer, M. Popovici, N. Menou, B. Kaczer, X.P. Wang, C. Adelmann, M.A. Pawlak, et al., High-k dielectrics for future generation memory devices, *Microelectron. Eng.*, 86, 2009, 1789-1795.

[178] A. Amith, P. Mark, Schottky barriers on ordered and disordered surfaces of GaAs (110), *J. Vac. Sci. Technol.*, 15, 1978, 1344-1352.

[179] D.R. Uhlmann, G. Teowee, J.M. Boulton, Dielectric relaxation in ferroelectrics, *J. Non-Cryst. Solids*, 131-133, 1991, 1194-1201.

[180] X. Kuang, M.M.B.Allix, J.B. Claridge, H.J. Niu, M.J. Rosseinsky, R.M. Ibberson, D.M. Iddles, Crystal structure microwave dielectric properties and AC conductivity of B-cation deficient hexagonal perovskites $La_5M_xTi_{4-x}O_{15}$ (x=0.5, 1; M=Zn, Mg, Ga, Al), *J. Mater. Chem.*, 16, 2006, 1038-1045.

[181] R. Waser, R. Hagenbeck, Grain boundaries in dielectric and mixed conducting ceramics, *Acta Mater.*, 48, 2000, 797-825.

[182] S. Guo, Densification of ZrB_2-based composites and their mechanical and physical properties: a review, *J. Eur. Ceram. Soc.*, 29, 2009, 995-1011.

[183] D. Segal, Soft chemistry routs to zirconia ceramics, *Key Eng. Mater.*, 153-154, 1998, 241-250.

[184] A.J. Bell, Ferroelectrics: The role of ceramic science and engineering, *J. Eur. Ceram. Soc.*, 28, 2008, 1307-1317.

[185] T.T. Fang, H.K. Shiau, Mechanism for developing the boundary barrier layers of $CaCu_3Ti_4O_{12}$, *J. Am. Ceram. Soc.*, 87, 2004, 2072-2079.

[186] J. Liu, Y. Sui, C. Duan, W, Mei, R. Smith, J.R. Hardy, $CaCu_3Ti_4O_{12}$: low-temperature synthesis by pyrolysis of an organic solution, *Chem. Mater.*, 18, 2006, 3878-3882.

[187] C.-F. Yang, Improvement of the sintering and dielectric characteristics of surface barrier layer capacitors by CuO addition, *Jpn. J. Appl. Phys.*, 35, 1996, 1806-1813.

[188] C.-F. Yang, L. Wu, T.-S. Wu, Effect of CuO on the sintering and dielectric characteristics of $(Ba_{1-x}Sr_x)(Ti_{0.9}Zr_{0.1})O_3$ ceramics, *J. Mater. Sci.*, 27, 1992, 6573-6578.

[189] Y.-H. Lin, J. Cai, M. Li, C. Nan, J. He, High dielectric and nonlinear electrical behaviours in TiO_2-rich $CaCu_3Ti_4O_{12}$ ceramics, *Appl. Phys. Lett.*, 88, 2006, 172902.

[190] B.S. Prakash, K.B.R. Varma, Effect of sintering conditions on the microstructural, dielectric, ferroelectric and varistor properties of $CaCu_3Ti_4O_{12}$ and $La_{2/3}Cu_3Ti_4O_{12}$ ceramics belonging to the high and low dielectric constant members of $ACu_3M_4O_{12}$ (A= alkali, alkaline-earth metal, rare-earth metal or vacancy, M= transition metal) family of oxides, *Physica B*, 403, 2008, 2246-2254.

[191] W. Li, R.W. Schwartz, ac conductivity relaxation processes in $CaCu_3Ti_4O_{12}$ ceramics: Grain boundary and domain boundary effects, *Appl. Phys. Lett.*, 89, 2006, 242906.

[192] S.-M. Wang, S.-J.L. Kang, Grain boundary segregation and high nonlinear I-V characteristics in Fe-added strontium titanate, *J. Am. Ceram. Soc.*, 91, 2008, 2617-2622.

[193] A.K. Singh, S.K. Barik, R.N.P. Choudhary, P.K. Mahapatra, Ac conductivity and relaxation mechanism in $Ba_{0.9}Sr_{0.1}TiO_3$, *J. Alloy. Comp.*, 479, 2009, 39-42.

[194] Q. Tang, M. Shen, L. Fang, Anomalous dielectric properties in $(BaSr)TiO_3$ films fabricated by pulsed-laser deposition in N_2 atmosphere, *Solid State Commun.*, 135, 2005, 707-710.

[195] P. Thongbai, T. Yamwong, S. Maensiri, Correlation between giant dielectric response and electrical conductivity of CuO ceramic, *Solid State Commun.*, 147, 2008, 385-387.

[196] A.J. Bard, L.R. Faulkner, Electrochemical methods – fundamental and applications, John Wiley & Sons, New York, 1980.

[197] T.B. Adams, D.C. Sinclair, A.R. West, Influence of processing conditions on the electrical properties of $CaCu_3Ti_4O_{12}$ ceramics, *J. Am. Ceram. Soc.*, 89, 2006, 3129-3135.

[198] C. Masingboon, P. Thongbai, S. Maensiri, T. Yamwong, S. Seraphin, Synthesis and giant dielectric behaviour of $CaCu_3Ti_4O_{12}$ ceramics prepared by polymerized complex method, *Mater. Chem. Phys.*, 109, 2008, 262-270.

List of publications

1. **S. Ren**, W. Kochanek, H. Bolz, M. Wittmar, I. Grobelsek, M. Veith*, Combinatorial preparation of solid-state materials by injection moulding, *J. Eur. Ceram. Soc.*, 28, 2008, 3005-3010.
2. M. Veith*, **S. Ren**, M. Wittmar, H. Bolz, Giant dielectric constant response of the composites in ternary system CuO-TiO_2-CaO, *J. Solid State Chem.*, 182, 2009, 2930-2936.
3. **S. Ren**, M. Wittmar, M. Aslan, I. Grobelsek, M. Quilitz, M. Veith*, Dielectric properties of composites in the CuO-TiO_2-CaO system, *11^{th} International Conference and Exhibition of the European Ceramic Society (11^{th} ECerS Conference)*, Krakow, Poland, June 21-25, 2009. (Oral presentation + Manuscript)